Spin-Preserving Metasurface-Based Focusing Mirror for Enhancing Light-Matter Interactions

by

Fehime Sema Kuru

A thesis
presented to the University of Waterloo
in fulfillment of the
thesis requirement for the degree of
Master of Science
in
Physics

Waterloo, Ontario, Canada, 2021

Author's Declaration

I hereby declare that I am the sole author of this thesis. This is a true copy of the thesis, including any required final revisions, as accepted by my examiners.

I understand that my thesis may be made electronically available to the public.

Abstract

We propose a dielectric metasurface mirror that focuses one spin state while diverging the other state and preserves the spin state upon reflection, unlike conventional mirrors. First, we discuss the working principle of the mirror and introduce an earlier version of the design to discuss important potential drawbacks to a metasurface design. Then, we simulate a mirror design that can preserve the spin state up to 99.6%. Overall, the simulations give 81% reflectivity for the desired spin state, half of which is due to material loss. A Fabry Pérot optical cavity formed by a pair of such mirrors would have a finesse of 15 and Q value of 1964. We find the focusing of the mirror to have good quality, with a Strehl ratio of 0.88. We simulate a cavity numerically to find the mode profile after 120 roundtrips. We estimate a mode volume of $725\mu m^3$ for a cavity with length $56\mu m$ and mirror size $15\mu m$. Our metasurface design has potential to be used in quantum optics to enhance light-matter interactions and optical nonlinearities. The reflectivity of the mirror can be further enhanced by overcoming material loss, which would allow a high finesse cavity for single spin state to be built. Last, we construct and characterize with broadband polarization tomography a fiber integrated quarter-waveplate formed by misaligning and splicing a short section of polarization maintaining fiber with precise length.

Acknowledgements

First, I would like to thank my supervisor, Michal Bajcsy, for his guidance and support. He always encouraged me to work on my weaknesses and helped me grow as a scientist and provided me with many opportunities to gain experience during my masters. I was working alongside with a postdoc in our group, Behrooz Semnani, who helped me with my project patiently and provided so many great insights. Another postdoc in our group, Rubayet Al-Maruf, have perfromed the characterization of the dielectric materials, but also provided useful insight for my simulations and lab work. I would like to thank them for their help. I thank my lab partners Yujia and Michael, who have worked on tomography measurements with me, and I thank Yujia for developing the code for the measurements. I would like to thank the other members of the group for their kindness and support. I thank Taso Alkiviades for his help with the glass processing station. I thank all my amazing friends for helping me take my mind off things at stressful times and making Waterloo a more fun place to be at.

Dedication

This thesis is dedicated to my family who have always supported me with my life decisions. I would not be here without their support.

Table of Contents

List of Figures

List of Tables

Chapter 1

Introduction

1.1 Quantum Optics

Light is made up of units of energy called photons, according to particle interpretation of light. In free space, photons do not interact with each other. However, nonlinear optical medium can act as a mediator for photon-photon interactions since optical properties of nonlinear medium depend on the presence of photons. At the same time, the optical nonlinearities are usually very low when only a few photons are present. Creating strong interactions at the single photon level has been a major goal of quantum optics research. Different approaches have been developed, such as taking advantage of the strong nonlinearities in graphene [43, 1], using waveguides to confine light and trap atoms in close proximity [57], implementing a cavity to a waveguide to further enhance interaction strength [24, 18], designing photonic structures such as nano-antennas [46], or designing cavities with high quality factors and low mode volumes [51]. The ratio of spontaneous emission of atoms coupled to a resonant cavity to atoms in free space can be described by the Purcell factor: $F_P = \frac{3}{4\pi^2}\left(\frac{\lambda_0}{n}\right)^2 \frac{Q}{V}$ [40]. Q describes the temporal confinement of light, and is a measure of how well light is confined in the cavity, and V describes the mode volume, which is a measure of spatial confinement. High Q factors and low mode volumes increase spontaneous emission significantly in a cavity, which leads to stronger interactions.

Another more recent technique for enhancing interactions is using the spin-orbit coupling of light. Circularly polarized (CP) light, whose net electric field vector rotates perpendicular to direction of propagation, carries spin angular momentum by an amount $\pm\hbar$ per photon. Photons with spin can interact with atomic transitions by transferring its spin to/from atomic transitions between energy levels. It is stated by Gonzalez-Ballestero *et al.*

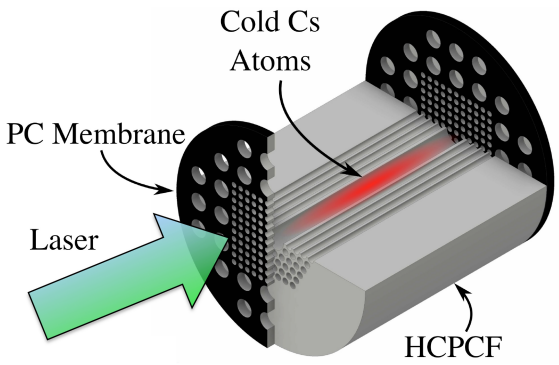

Figure 1.1: Fabry Perot cavity integrated with HCPCF. Image obtained from [17].

[20] that interaction with spin can lead to 50% more enhanced entanglement for the case without spin. Light-matter interactions with spin can enhance the interaction strength significantly [32]. Furthermore, there exists optical transitions coupled to different values of spin [32], which have different transition strengths [41] or decay rates [54]. This provides flexibility to use different spin state for various purposes. Another advantage of spin is the efficient directionality of light emitted from atoms. Nanophotonic waveguides were constructed that separate two spin states [38, 45, 7], so that emitters can be coupled to the respective directions on the waveguide. Research on chiral light-matter interaction in cavities have been recently developing [54], and this thesis intends to contribute by building a cavity that supports a single state of spin (circular polarization), such that light-matter interactions will be significantly enhanced.

In Fig. 1.1, a Fabry Pérot cavity, integrated with a hollow-core photonic crystal fiber (HCPCF) is given from the study by Flannery *et al.* [18]. Transverse confinement of light is implemented by the HCPCF, and the hollow core allows atoms to be injected inside the fiber [6] to interact with the confined light. Mounting mirrors on both sides will result with the cavity, where light is confined in the longitudinal direction. Our mirror design aims to achieve the same operation. First, it should operate as a mirror and preserve the CP state of incident light, so that cavity supports a single CP state. Second, it should confine light in the transverse direction, which can be implemented if the mirrors are focusing mirrors. For this purpose, we have chosen to build our mirror using dielectric metasurfaces.

1.2 Why Metasurfaces?

Metasurfaces are two-dimensional layers of sub-wavelength sizes, consisting of arrays of phase elements with sub-wavelength separations which add unique phase to the wavefront. Their small size and freedom to manipulate light open up a wide range of potential applications. Conventional optical elements can be made more compactly, and combinations of bulky optical elements can be implemented by a single structure.

Earlier metasurfaces consisted of plasmonic antennas [56], where the geometry of antennas affect the phase imparted on the field scattered. Quarter wave-plates [55], vortex plates [19] were created by this design. The performance of these devices in the optical region were limited due to high plasmonic loss at optical frequencies, insufficient coupling efficiency for single-layered structures and other sources of loss during phase modulation [26]. Dielectric metasurfaces overcome these limitations and offer a much efficient interface for designing metasurfaces in the optical frequencies. Dielectric metasurfaces are implemented as metalenses [58, 29, 16] including lenses with tunable focus [5], and reflectors [34, 3].

Metasurfaces are particularly useful for exploiting the chiral properties of light, where chirality refers to a structure whose mirror image is not superimposable on itself by any rotation or transformation, and circular polarization is a chiral property. Any application with circular polarization would require complex optical setup, consisting of waveplates, polarizers and more. Metasurfaces allow combining the effects of multiple objects into one, such as a metalens that is designed to separate two CP states by having two separate focal points [23], CP state selective transmittors [53] and waveguides. CP state preserving mirrors were also implemented using chiral photonic crystal mirrors [42] and chiral metamirrors [28].

Manipulating the phase and CP states of light have been an interest for a long time, and geometric phase is a common method to implement chiroptical properties [13, 33]. By this method, wavefront of light can be completely reshaped where the phase imparted on a section of wavefront is controlled solely by the rotation angle of the phase element on the optical structure, while the CP state is switched [37, 9]. Our proposed structure has two major properties: Focusing and preserving the CP state, both of which can be implemented by geometric phase method.

Separation or detection of CP state is particularly useful in biochemistry, as circular dichroism is observed in nature [21, 44], and detection of polarization of light has been applied by chiral metamaterials [8, 31] for sensing applications. Our metasurface mirror has potential applications outside of quantum optics, but this is outside of the scope of

this thesis.

1.3 Outline of the Thesis

The thesis starts with explaining some background in metasurfaces and optics. Main ideas like geometric phase and theory of dielectric waveguides are explained. Chapter 2 ends with an introduction of Fabry Pérot cavity. In Chapter 3, we introduce the steps to building a metasurface mirror design, and discuss some performance issues with an earlier version of our design. Discussion of these issues are necessary to understand some changes that were made to the design, and to make sure similar issues are omitted for other dielectric metasurface mirror designs. In Chapter 4, we update the unit cell design and analyse its performance. We construct the full mirror and show that it successfully acts as a focusing mirror. Then, operation of a potential cavity built by this mirror is analytically discussed. In Chapter 5, we design a fiber integrated quarter-waveplate, where two polarization maintaining optical fibers are spliced together. Then, we characterize the fiber using broadband polarization tomography.

Chapter 2

Metasurfaces and Optics

In this chapter, we will introduce the theory necessary to understand how our metasurface mirror can implement geometric phase and circular polarization (CP) state preservation and some key points to consider when designing a metasurface mirror. First, we will discuss diffraction gratings, which are periodic structures similar to metasurfaces, and show how we can avoid our structure to act like a diffraction grating to prevent any unwanted diffraction. Then, we will introduce the CP states of light and its electric field and Jones matrix representation, which will be useful when discussing the geometric (Berry) phase in the next section, where we will show that rotating an optical element can induce geometric phase, and we will argue how having a half-waveplate (HWP) element contributes to both conservation of CP state and the implementation of geometric phase. Then, we will discuss how rectangular waveguides can be designed to operate as a HWP, which will be used in the metasurface design. Last, we will introduce the Fabry Pérot cavity and its properties.

2.1 Diffraction Gratings

Diffraction gratings are optical elements with periodic structures that split the incident light into several components. A polychromatic light will get separated into its constituent wavelengths as each component reflects by slightly different angles. Here, we focus on monochromatic light. When a monochromatic light is incident on a diffraction grating, it will also get separated upon reflection, according to the diffraction orders m, where $m \in \mathbb{Z}$. Diffraction of monochromatic light by a diffraction grating working in the reflection mode is sketched in Fig. 2.1. The 0th order of diffraction is equivalent to reflection from a flat surface where the angle of reflection is the same as angle of incidence. The angle of

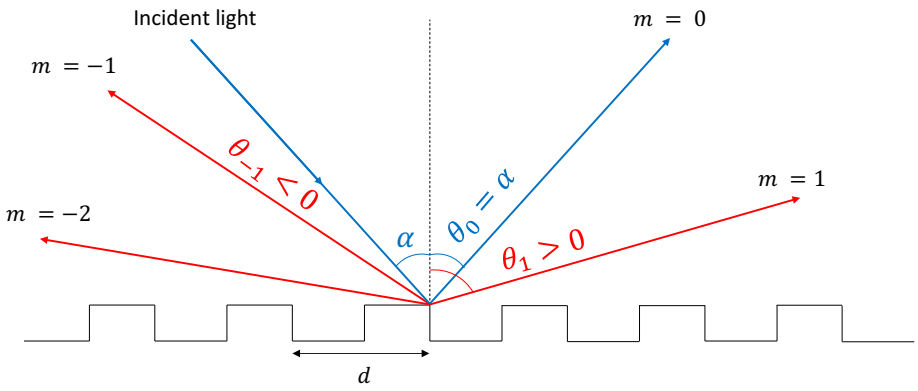

Figure 2.1: Diagram of a diffraction grating with periodicity d. The zeroth order of diffraction is reflection at an angle same as angle if incidence and is represented by the blue light ray. The higher orders of diffraction ($|m| > 0$) are represented by the red light rays.

reflection is different for higher orders of diffraction. Negative values of m correspond to negative angle of reflections.

The order of diffraction is determined by the grating equation given in Eqn. 2.1, where d is the size of one period, θ is the angle of reflection, α is the angle of incidence, $m \in \mathbb{Z}$ is the diffraction order and λ is the wavelength.

$$d(\sin\theta - \sin\alpha) = m\lambda \tag{2.1}$$

Non-zero m mean that diffraction occurs, and the incident light reflects at an angle $\theta \neq \alpha$. The simplest diffraction grating is a barrier with multiple slits. However, a periodic structure of dielectric elements also act as a diffraction grating, which is the case for metasurfaces. Non-zero orders of diffraction are not desired for most metasurface applications, including the mirror application in this study.

Assuming normal incidence ($\alpha = 0$), we can reorder the terms in Eqn. 2.1 as:

$$\sin\theta = \frac{m\lambda}{d} \tag{2.2}$$

For the minimum non-zero order, $m = 1$:

$$\theta = \arcsin\left(\frac{\lambda}{d}\right) \tag{2.3}$$

Domain of an arcsin function cannot be greater than 1 or less than -1, so no physical solution to the grating equation exists for $\lambda > d$. Therefore, a periodic structure where the periodicity is shorter than the wavelength of light should not have higher orders of diffraction. We will see later in Chapter 3 that this puts a limitation to our design periodicity.

Now the assumption of normal incidence is discarded ($\alpha \neq 0$), and the structure is treated as a mirror with some numerical aperture NA. NA is a quantity describing the operation of an imaging component for maximum possible angle of light incident on the structure or emitted from the structure, defined by $NA = n \sin\alpha$, where n is the refractive index of the surrounding medium and α is the angle of incidence (or reflection). For this system, the surrounding medium is air, so $n = 1$. Eqn. 2.1 can be rewritten as

$$d(\sin\theta - NA) = m\lambda \tag{2.4}$$

where the definition of NA is used. Following a similar reordering of terms for $m = 1$ and $m = -1$ will result with

$$\theta = \arcsin\left(NA \pm \frac{\lambda}{d}\right) \tag{2.5}$$

Here, $m = 1$ and $m = -1$ cases are distinguished by the term $\pm\lambda/d$. In order to prevent any high orders of diffraction, the domain of the arcsin function has to be > 1 and/or < -1. The four conditions are listed in Table 2.1.

Table 2.1: Diffraction Limitations on Periodicity

	$\arcsin(x) > 1$	$\arcsin(x) < -1$
$m = 1$	$d < \frac{\lambda}{1-NA}$	$d < -\frac{\lambda}{NA+1}$
$m = -1$	$d > \frac{\lambda}{NA-1}$	$d < \frac{\lambda}{NA+1}$

The most restricting and physical ($d > 0$) limitation is $d < \lambda/(NA + 1)$, considering that a typical NA of a mirror is less than 1. In Chapter 4, we will see how this relation between d and NA will be an additional limiting factor for the mirror design.

2.2 Conservation of Circular Polarization

2.2.1 Polarization of Light

Polarization of light describes the direction of the net electric field vector. Light is linearly polarized when the x and y components are in phase, and the direction of the electric field vector stays in the same plane in time and space. In Fig. 2.2, three possible polarizations are sketched, with the corresponding electric field expressions:

$$\begin{aligned} &\text{a. } \mathbf{E} = E_0 e^{i(kz-\omega t)}\hat{\mathbf{i}} = E_x \\ &\text{b. } \mathbf{E} = E_0 e^{i(kz-\omega t)}\hat{\mathbf{j}} = E_y \\ &\text{c. } \mathbf{E} = E_0 e^{i(kz-\omega t)}(\cos\theta\hat{\mathbf{i}} + \sin\theta\hat{\mathbf{j}}). \end{aligned} \tag{2.6}$$

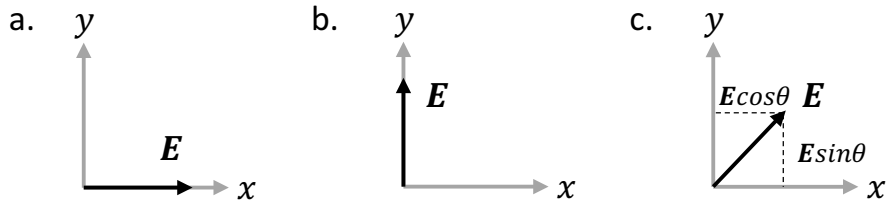

Figure 2.2: Electric field vector diagram showing three possible states of linear polarization. In a, light is polarized in the $x-$direction, in b, light is polarized in the $y-$direction, and in c, light has some arbitrary polarization in the $x-y$ plane, which is uniquely described by the angle θ.

E_x and E_y notations will be used to describe the x and y polarized light respectively.

Light is circularly polarized when the x and y components are out of phase by $\pi/2$, and the electric field is not confined to a plane but rotating in a circle in either clockwise or counter-clockwise direction.

Consider a wave propagating towards $+z$ direction and has E_x and E_y components of equal magnitude. If E_x component leads E_y component by $\pi/2$ phase (Eqn. 2.8), the wave is left handed circularly polarized (LHCP), and rotates in the counter-clockwise direction.

First row of Fig. 2.3 visualizes how a phase lag between E_x and E_y can cause the rotation of the electric field in the counter-clockwise direction.

$$\mathbf{E_l} = E_0 e^{i(kz-\omega t)} \left(\hat{\mathbf{i}} + e^{i\pi/2}\hat{\mathbf{j}}\right) \tag{2.7}$$

If E_y component leads E_x component by $\pi/2$ phase (Eqn. 2.7), the wave is right handed circularly polarized (RHCP), and rotates in the clockwise direction. Second row of Fig. 2.3 visualizes how a phase lag between E_x and E_y can cause the rotation of the electric field in the clockwise direction.

$$\mathbf{E_r} = E_0 e^{i(kz-\omega t)} \left(\hat{\mathbf{i}} + e^{-i\pi/2}\hat{\mathbf{j}}\right) \tag{2.8}$$

If the magnitudes of E_x and E_y are not equal, then the light is elliptically polarized, where the oscillation of the electric field vector covers an elliptical path rather than circular.

By convention, direction of rotation is defined such that the observer looks towards the direction of propagation. Therefore, the direction of propagation will be set to $+z$ throughout the project.

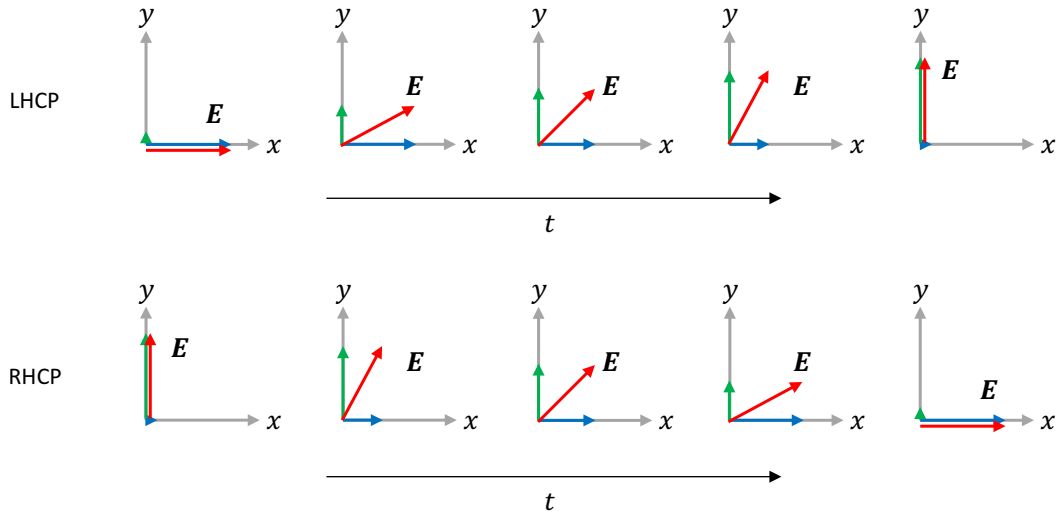

Figure 2.3: Electric field vector diagram showing the oscillations of E_x (blue) and E_y (green) over time and the rotation of the net vector (red). The upper row correspond to LHCP light where the net electric field rotates counter-clockwise and the lower row correspond to RHCP light where the net electric field rotates clockwise.

2.2.2 Jones Calculus

Jones Calculus is an alternative formulation of polarized light where polarization is described by Jones vectors and optical elements such as waveplates and mirrors are described by Jones matrices [15]. Table 2.2 lists some common and relevant Jones vectors and matrices.

2.2.3 Reflection from a Mirror

When a circularly polarized light of certain CP state reflects off a mirror, its state is reversed. Therefore, simply put, reflection off a mirror will result with the mirror image of a CP state, i.e. the other state.

In a more elaborate way, let's assume a LHCP light incident on a mirror, perpendicular to the surface. The coordinates are defined such that light propagates in the z direction and x and y axes are on the plane perpendicular to direction of propagation. The right-hand rule of orientation of axes dictates that $\hat{z} = \hat{x} \times \hat{y}$, where $\times$ denotes the cross product. At normal incidence, the electric field components stay the same (magnitude and phase) upon reflection. However, reflection changes the direction of propagation to $-\hat{z}$. In order to define the CP state of the reflected light, the coordinate system need to be reset where the new direction of propagation is $\hat{z}'$. The limiting condition on the new coordinate system is $\hat{z}' = -\hat{z}$. Therefore, $\hat{x}' \times \hat{y}' = -\hat{x} \times \hat{y}$. Two of many possible conditions to satisfy this are $\hat{x}' = -\hat{x}$ or $\hat{y}' = -\hat{y}$. Let's apply the latter and see how the electric field is affected. Starting from the expression for LHCP light in Eqn. 2.7, we change the sign of E_y.

$$\mathbf{E}_{ref} = E_0 e^{i(kz-wt)} \left(\hat{\mathbf{i}} - e^{i\pi/2}\hat{\mathbf{j}}\right) = E_0 e^{i(kz-wt)} \left(\hat{\mathbf{i}} + e^{-i\pi} e^{i\pi/2}\hat{\mathbf{j}}\right) = E_0 e^{i(kz-wt)} \left(\hat{\mathbf{i}} + e^{-i\pi/2}\hat{\mathbf{j}}\right) = \mathbf{E_r} \tag{2.9}$$

The reflected light becomes RHCP following the expression in Eqn. 2.7 due to the change in direction of propagation.

Additionally, as light travels from one medium to another medium with different refractive indices, different polarization states get reflected and transmitted by different amounts, which changes the polarization of the reflected and transmitted lights. Two types of polarization under consideration are p- and s-polarizations, which are special cases of linear polarization. P-polarized light is when the electric field is parallel to the plane of incidence, and s-polarized light is when the electric field is perpendicular to the plane of incidence.

We will only consider the case for reflection, but a similar result holds for transmission. Fresnel coefficients describe the reflection of p- and s-polarizations, and are given as

$$r_s = \frac{n_1 \cos\theta_i - n_2 \cos\theta_t}{n_1 \cos\theta_i + n_2 \cos\theta_t} \qquad r_p = \frac{n_1 \cos\theta_t - n_2 \cos\theta_i}{n_1 \cos\theta_t + n_2 \cos\theta_i} \tag{2.10}$$

n_1 and n_2 are indices of refraction of the first and second layers and θ_i and θ_t are the angles of incidence and transmission respectively. At normal incidence, p- and s-polarizations have the same orientation relative to the interface, therefore at normal incidence $r_s = r_p$. As the angle of incidence is increased, the reflection coefficients change for both polarizations. If a CP light is incident with $\theta_i \neq 0$, this would cause its two components to reflect by different amounts, causing the reflected light to become elliptically polarized. According to the expression, r_p reaches 0 when $n_1 \cos\theta_2 = n_2 \cos\theta_1$, so all of p-polarized light gets transmitted. The angle of incidence at which this condition occurs is called Brewster's Angle and is found by $\theta_B = \tan^{-1}(n_2/n_1)$. For angles beyond θ_B, r_p and r_s has negative signs, which means there is π phase offset between the two polarizations.

In general, air-to-metal interfaces have relatively constant Fresnel coefficients for varying incident angles because of very high refractive indices of metals. Also we are mostly concerned with close-to-normal incident angles, so its effect should be minimal.

The effect of air-to-dielectric layer will be mentioned in Section 2.4.

2.2.4 Preserving the CP State

It has shown that reflection from a conventional mirror changes the state of CP polarization. Now, an approach to preserve the CP state will be introduced, which will be useful when the geometric phase method is discussed. Let's consider a HWP and a RHCP light incident on the optical element. HWP is a birefringent optical element which induces a relative π phase to one linear polarization state along its axis. This switches the RHCP light to LHCP (and vice versa). Its Jones matrix is given in Table 2.2. A simple way to calculate the state after HWP is multiplying the Jones matrix of the HWP with the Jones vector of RHCP light as

$$\begin{pmatrix} 1 & 0 \\ 0 & -1 \end{pmatrix} \begin{pmatrix} 1 \\ -i \end{pmatrix} / \sqrt{2} = \begin{pmatrix} 1 \\ i \end{pmatrix} / \sqrt{2} \tag{2.11}$$

It is clear that the resulting vector represents LHCP light.

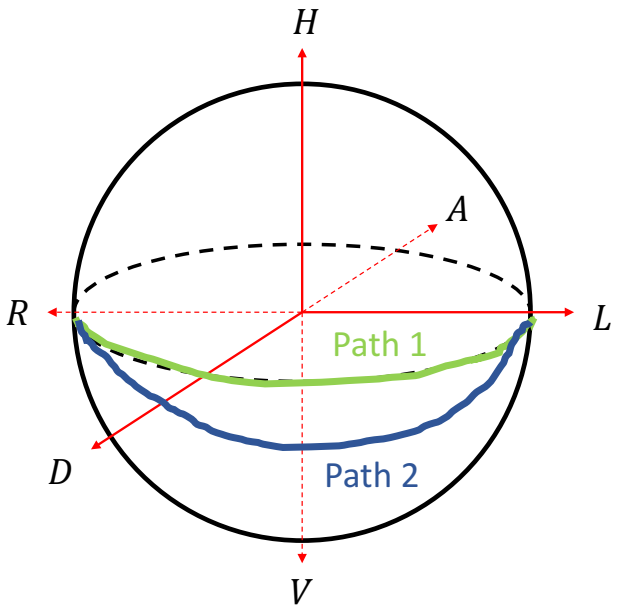

Figure 2.4: Poincaré sphere representing the polarization states of light. Two of many possible paths are shown as light goes through a HWP with rotational degree of freedom. The phase gained during the path is geometric phase, and is different for the two paths.

Now, let's add some mirror halfway through the HWP perpendicular to the direction of propagation. The two configurations are also given in Fig. 2.5 a and c. Now, the incident light travels half the length of HWP, reflects off the mirror, and travels the same path in the opposite direction. The propagation length through the HWP is exactly the same, therefore the CP state is reversed. However, the direction of propagation changes from $+z$ to $-z$, which also reverses the CP state, as it was discussed in Section 2.2.3. The overall effect of the combined operation should preserve the CP state overall. This is the idea of how geometric phase method also contributes to the preservation of the CP state, but we will see in detail how it also implements the necessary phase such that the wavefront of light can be manipulated to construct the focusing mirror.

2.3 Geometric (Berry) Phase Method

Geometric phase method is the main mechanism to understand the working principle of the CP state preserving focusing mirror. It allows to uniquely manipulate the wavefront of

light by discrete phase elements, so in order to reshape the wavefront accurately, one needs complete control over the wavefront of light, i.e. implement phase lag on the wavefront, ranging from $0 - 2\pi$ rad. We will see how geometric phase achieves this freedom of control over the wavefront, as well as preserving the CP state.

First, let's consider the representation of polarization by Poincaré sphere, given in Fig. 2.4. Polarized light can be represented by a vector lying on the sphere, and each axis represents different polarization states. A HWP changes the polarization state from LHCP to RHCP, so the polarization vector moves from L to R. The polarization vector can take any path on the sphere, and it is defined by the rotation of the HWP. Different rotation angles can cause phase to evolve by following different paths, as sketched in the figure. The distance of the path taken imparts global phase, which is called the geometric phase [9].

Now, geometric phase will be derived mathematically. Consider a CP plane wave incident on some transmissive optical element with rotational freedom about $z-$axis, as given in Fig. 2.5 b.

It has two optical axes called ordinary and extraordinary axes. The two axes have different effective refractive indices, so they cause birefringence. They are defined such that at $\theta = 0$ deg., the two axes are aligned with the $x-$ and $y-$axes. A general Jones matrix can be defined for this element, $\hat{t}$ as

$$\hat{t} = \begin{pmatrix} t_{xx} & t_{xy} \\ t_{yx} & t_{yy} \end{pmatrix} \tag{2.12}$$

The components are the transmission coefficients where the first subscript refers to the incident polarization and the second subscript refers to the output polarization. The system is simplified such that $t_{xy} = 0$ and $t_{yx} = 0$, so E_x and E_y are not coupled. Rotation of the optical element will misalign its optical axes with the incident light polarization. Therefore, Jones matrix of the optical element is transformed by rotation matrices. The Jones matrix as a function of angle of rotation (θ) can be written as

$$\hat{t}(\theta) = R(-\theta) \begin{pmatrix} t_x & 0 \\ 0 & t_y \end{pmatrix} R(\theta) = \begin{pmatrix} \cos\theta & \sin\theta \\ -\sin\theta & \cos\theta \end{pmatrix} \begin{pmatrix} t_x & 0 \\ 0 & t_y \end{pmatrix} \begin{pmatrix} \cos\theta & -\sin\theta \\ \sin\theta & \cos\theta \end{pmatrix} \tag{2.13}$$

where we have removed one subscript from transmission coefficients. Jones vector of the incident light is given as $\hat{e}_{r/l} = (\hat{x} \mp i\hat{y})/\sqrt{2}$ for two states of circular polarization. The

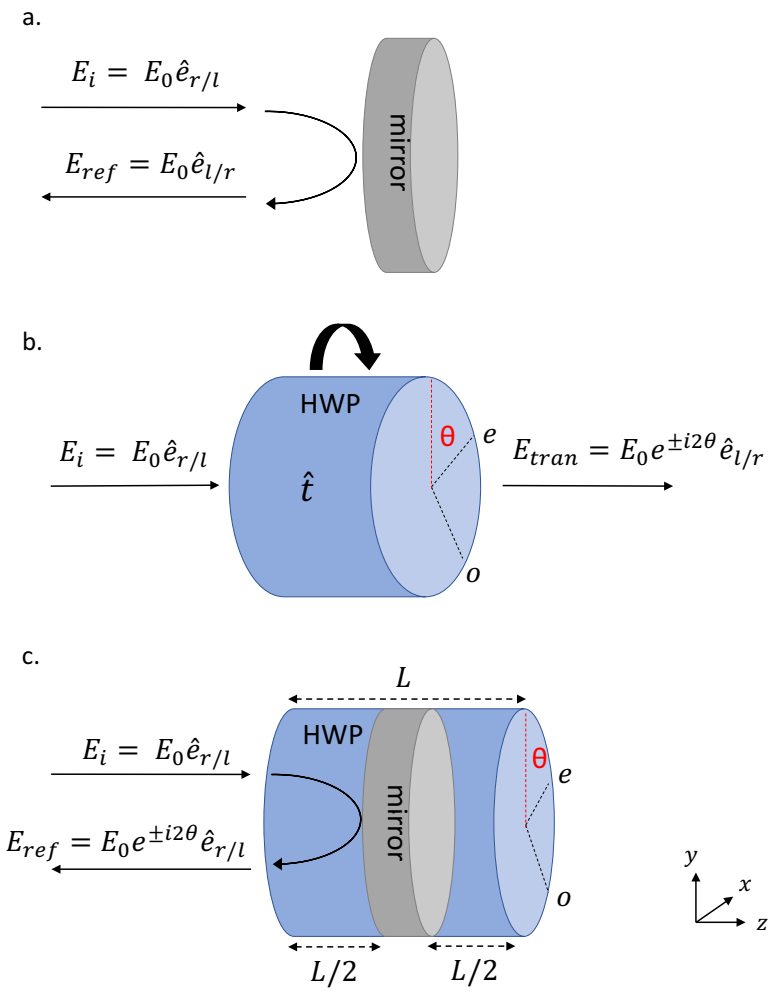

Figure 2.5: A three step diagram explaining CP state preservation and geometric phase. (a) The effect of reflection by a conventional mirror to the CP state. (b) The operation of a HWP and the geometric phase arising from the rotation of the optical element. The two axes of the element (ordinary, o, and extraordinary, e) are shown in the figure, which are aligned with $x-$ and $y-$axes at $\theta = 0$. (c) Combining the cases in a and b, a mirror is put halfway through the HWP. One round trip will combine the effects of the two cases, resulting with CP state preservation and geometric phase. The reflected field is also derived in text.

Jones vector of the transmitted light ($\hat{e}'$) can be derived simply by multiplying the incident Jones vector with the Jones matrix of the optical element.

$$\hat{e}' = \hat{t}(\theta)\hat{e}_{r/l} = \begin{pmatrix} t_x \cos^2\theta + t_y \sin^2\theta & -(t_x - t_y)\cos\theta\sin\theta \\ -(t_x - t_y)\sin\theta\cos\theta & t_x \sin^2\theta + t_y \cos^2\theta \end{pmatrix} \begin{pmatrix} 1 \\ \mp i \end{pmatrix} /\sqrt{2}$$

$$= \begin{pmatrix} t_x \cos^2\theta + t_y \sin^2\theta \pm i(t_x - t_y)\cos\theta\sin\theta \\ -(t_x - t_y)\sin\theta\cos\theta \mp i(t_x \sin^2\theta + t_y \cos^2\theta) \end{pmatrix} /\sqrt{2}$$

Now, the following trigonometric identities are applied:

$$\sin x \cos x = \frac{\sin 2x}{2}$$
$$\sin^2 x = \frac{1 - \cos 2x}{2}$$
$$\cos^2 x = \frac{\cos 2x + 1}{2}$$

The transmitted Jones vector can be written as

$$\hat{e}' = \begin{pmatrix} t_x \left(\frac{\cos 2\theta + 1}{2}\right) + t_y \left(\frac{1 - \cos 2\theta}{2}\right) \pm i(t_x - t_y)\frac{\sin 2\theta}{2} \\ -(t_x - t_y)\frac{\sin 2\theta}{2} \mp i\left[t_x \left(\frac{1 - \cos 2\theta}{2}\right) + t_y \left(\frac{\cos 2\theta + 1}{2}\right)\right] \end{pmatrix} /\sqrt{2}$$

$$= \begin{pmatrix} \frac{t_x + t_y}{2} + \frac{\cos 2\theta}{2}(t_x - t_y) \pm i(t_x - t_y)\frac{\sin 2\theta}{2} \\ -\frac{t_x - t_y}{2}\sin 2\theta \mp i\frac{t_x + t_y}{2} \pm i\frac{t_x - t_y}{2}\cos 2\theta \end{pmatrix} /\sqrt{2}$$

$$= \begin{pmatrix} \dfrac{t_x + t_y}{2} + \dfrac{t_x - t_y}{2}(\cos 2\theta \pm i \sin 2\theta) \\ \mp i\dfrac{t_x + t_y}{2} \pm i\dfrac{t_x - t_y}{2}(\pm i \sin 2\theta + \cos 2\theta) \end{pmatrix} /\sqrt{2}$$

The trigonometric functions are isolated. Now, Euler's formula $e^{\pm ix} = \cos x \pm i \sin x$ can replace the trigonometric part. Also, the component independent of θ can be separated into another vector as summation. Jones vector becomes

$$\begin{pmatrix} \dfrac{t_x + t_y}{2} \\ \mp i\dfrac{t_x + t_y}{2} \end{pmatrix} + \begin{pmatrix} \dfrac{t_x - t_y}{2} e^{\pm i2\theta} \\ \pm i\dfrac{t_x - t_y}{2} e^{\pm i2\theta} \end{pmatrix} /\sqrt{2} = \frac{t_x + t_y}{2} \begin{pmatrix} 1 \\ \mp i \end{pmatrix} /\sqrt{2} + \frac{t_x - t_y}{2} e^{\pm i2\theta} \begin{pmatrix} 1 \\ \pm i \end{pmatrix} /\sqrt{2}$$

$$\hat{e}' = \hat{t}(\theta)\hat{e}_{r/l} = \frac{t_x + t_y}{2}\hat{e}_{r/l} + \frac{t_x - t_y}{2} e^{\pm i2\theta}\hat{e}_{l/r} \tag{2.14}$$

A RHCP light incident on some rotating optical element will have RH and LH components depending on the transmission coefficient of the optical element. If $(t_x + t_y)/2 = 1$, the transmitted light will consist of only the incident CP state. If $(t_x + t_y)/2 = 0$, the transmitted light will change its CP state completely. The two cases can be compactly written as

$$\hat{e}^t = \hat{t}(\theta)\hat{e}_{r/l} = \begin{cases} \hat{e}_{r/l}, & \text{if } \dfrac{t_x + t_y}{2} = 1 \\ e^{i2\theta}\hat{e}_{l/r}, & \text{if } \dfrac{t_x - t_y}{2} = 1 \end{cases} \tag{2.15}$$

The second condition be implemented by setting $t_x = 1$ and $t_y = -1$ or vice versa. This is equivalent to the operation of a HWP, where $t_y = -1$ can be interpreted as $e^{i\pi}$ phase lag.

If the change of CP state due to reflection is also taken into account in Eqn. 2.14, it can be rewritten as

$$\hat{e}^t = \hat{t}(\theta)\hat{e}_{r/l} = \frac{t_x + t_y}{2}\hat{e}_{l/r} + \frac{t_x - t_y}{2} e^{\pm i2\theta}\hat{e}_{r/l} \tag{2.16}$$

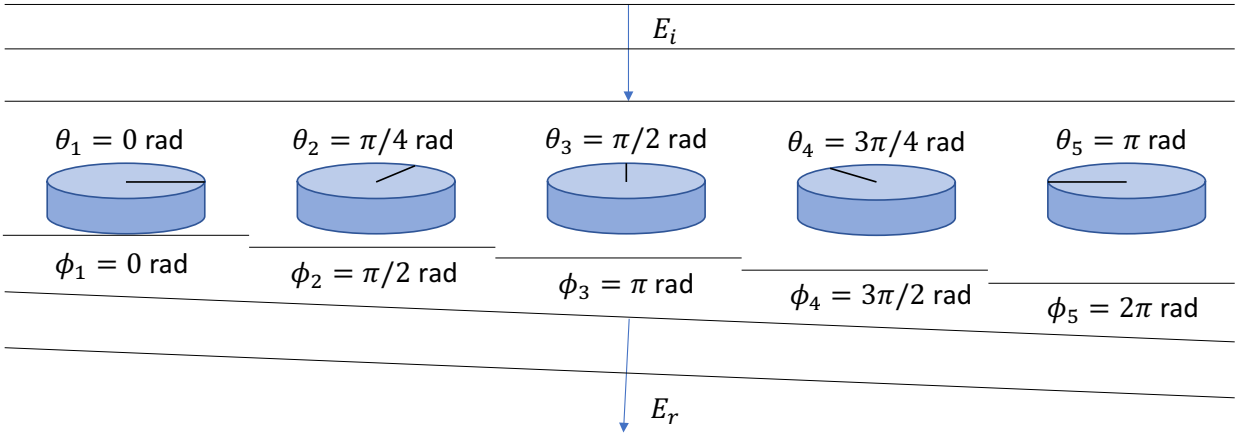

Figure 2.6: Diagram of five optical elements demonstrating refraction by geometric phase method. The optical elements are rotated by steps of $\pi/4$ rad., so they induce phase to the wavefront by an amount of 2θ. The discrete phase levels combine to make a continuous wavefront.

where the CP state of the output is switched. Another property that arise from this system is the phase factor in the second term of Eqn. 2.16. The phase $\pm 2\theta$ is gained by the same CP state of the incident light and is defined as the geometric phase:

$$\phi = \pm 2\theta \tag{2.17}$$

This is the overall effect of geometric phase when these optical elements are also incorporated with a mirror, such that they act as a HWP whilst changing the direction of propagation of light. The process is summarized in Fig. 2.5.

For a system with a single optical element, this is a global phase on the CP state and cannot be distinguished by itself. Instead, consider a system with multiple but identical phase elements given in Fig. 2.6, where each phase element is rotated by a different θ. There will be phase difference at the output of each phase element. Therefore, wavefront of light can be manipulated with complete freedom as the phase elements can be rotated by a range of $0 - 2\pi$ rad., giving phase manipulation of range $0 - 4\pi$ rad., which is much larger than the necessary $0 - 2\pi$ rad. phase range for complete manipulation of wavefront.

In the given system, refraction of light is demonstrated. The incident plane wave goes through the phase elements, each rotated between $0 - \pi$ rad. by increments of $\pi/4$

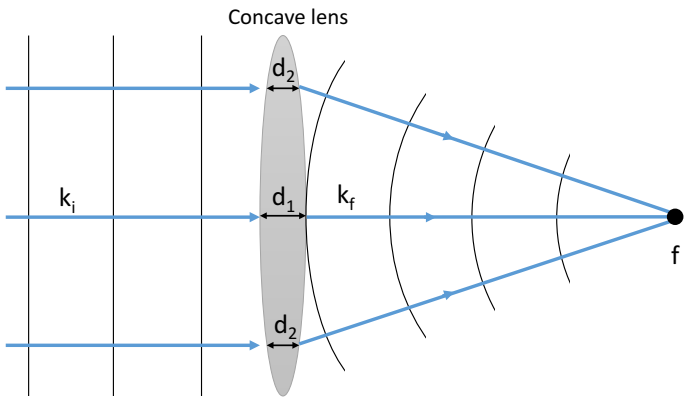

Figure 2.7: Ray and wavefront diagram of light being focused by a concave glass lens. Different positions on the lens cause light to propagate through different thicknesses of light, changing the shape of the wavefront to spherical.

as shown, and gains phase by increments of $\pi/2$, resulting with a phase gradient. The wavefront becomes a step function right after the optical elements, but they interfere to create a smooth planar wavefront propagating at an angle relative to the incident light.

This idea of wavefront shaping is identical to how lenses operate. Consider a plane wave incident on a concave lens surrounded by air, as shown in Fig. 2.7. The incident wave propagates in the $+z$ direction, and its phase is constant in the $x-y$ plane. As light enters the lens, which is made up of material with refractive index $n_m > n_{air}$, the propagation slows down to c/n_m, therefore the phase gained by the wave increases, relative to propagation in air. However, the thickness of the lens is the largest at the center, d_1, and decreases towards the edges, eg. d_2. The retardation of the wave is weaker at the tips, compared to the center. As the plane wave goes through the lens, its phase structure does not remain planar, as every position in the $x-y$ plane goes through different thickness of material, resulting with a unique wavefront. This is a spherical wavefront and expressed by Eqn. 2.18 in the $x-y$ plane for a concave lens, where f is the focal length and λ is the wavelength.

$$\psi(x,y) = \frac{2\pi}{\lambda}\left(f - \sqrt{x^2+y^2+f^2}\right) \tag{2.18}$$

Similarly, a planar focusing lens can be constructed by applying the wavefront shaping technique using the rotation of phase elements. If the phase elements are rotated according to the spherical wavefront expression given in Eqn. 2.18, the structure acts as a focusing

lens for an incident plane wave. Simply by adding a reflecting surface, the focusing lens can also operate as a mirror.

Surely, this implementation of wavefront shaping is different than the wavefront shaping induced by a lens made up of continuous material (eg. glass). The phase elements induce a discrete phase to the wavefront, which combine to create the final wavefront. Huygen's principle [25] states that light can be represented by superposition of light emitted from point sources if every point on the wavefront was acting like a point source. With metasurfaces consisting of discrete phase elements, the wavefront is in fact formed by superposition of light leaving the phase elements. Intuitively, a small number of phase elements cannot describe a complicated wavefront. The number of phase elements refer to the discrete phase levels in the phase range $0 - 2\pi$ rad. representing the wavefront.

Consider the refraction example discussed above. The wavefront of refracted light will be more distorted if only two phase elements are used instead of four, and same comparison can be made for four or more phase elements. Aieta *et al.* [2] have worked on quantifying the aberrations of flat focusing lenses caused by finite number of phase elements. They have defined a wave aberration function (WAF) which is the difference between the wavefront and the aberration-free wavefront. When $\langle WAF\rangle^2 - \langle WAF^2\rangle < \lambda/14$, where the brackets denote the mean value, diffraction is more dominant for the quality of imaging and therefore aberrations are negligible. They have calculated that this condition is satisfied for number of phase elements as small as four for a flat lens. Our mirror structure should have much more than four phase elements covering the phase range, therefore the discreteness should not distort the wavefront.

2.4 Dielectric Waveguides as Half-Waveplates

As we have established in Section 2.3, a birefringent phase element that will act as a HWP is a necessary component of our metasurface for implementing geometric phase. Rectangular dielectric waveguides (the nanopillars in the mirror design) can be used as the required phase elements. Dielectric materials with refractive indices larger than the surrounding refractive index can be used as waveguides by a phenomena called total internal reflection (TIR). TIR is the complete reflection of light as it travels from a high to low index material and is the working mechanism of fiber optic cables.

Consider the system in Fig. 2.8, where the layers are isotropic media with associated refractive indices. Light enters the system through layer 1, and reaches the interface between layers 1 and 2. Snell's Law describes the angle of refraction as light travels from layer 1 to layer 2, and is given in Eqn. 2.19.

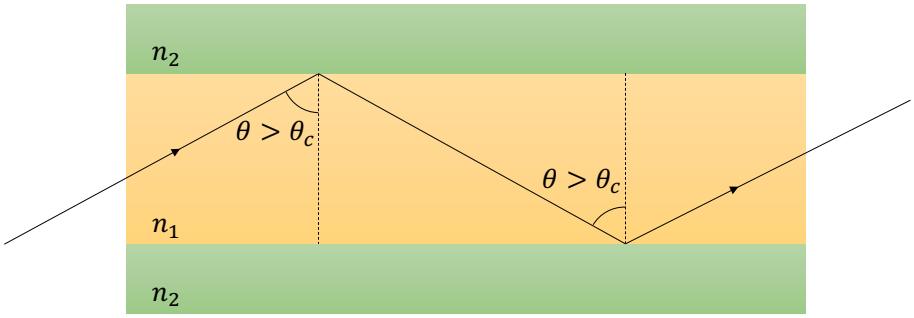

Figure 2.8: Total internal reflection (TIR) in a two-material structure. The yellow and green regions have refractive indices n_1 and n_2 respectively, where $n_1 > n_2$. TIR occurs for incident angles greater than the critical angle θ_c. TIR allows the propagation of light through the yellow region.

$$n_1 \sin\theta_1 = n_2 \sin\theta_2 \tag{2.19}$$

For $n_1 > n_2$, there exists some angle of incidence, called the critical angle θ_c, at which the angle of refraction is 90 deg. Light incident on the interface by an angle greater than the critical angle will undergo complete reflection, i.e. TIR. The critical angle can be calculated from Snell's Law, and is given as

$$\theta_c = \arcsin\frac{n_2}{n_1} \tag{2.20}$$

Therefore, high refractive index materials can confine light within the structure and can be used as waveguides.

A property of dielectric waveguides that is useful here is the dependence of refractive index on the size of the waveguide for sub-micrometer length scales. This relationship was analysed computationally using Lumerical's MODE analysis tool which calculates spatial profile of waveguide modes by solving Maxwell's equations at a cross-section of a waveguide. The simulations also return the effective refractive index experienced by that particular mode. Details of MODE simulations with Lumerical software can be found in Appendix A.

Let's consider a system where a square-shaped waveguide with $n = 3$ is surrounded by free space. The variation of n_{eff} by a change in D for such system is given in Fig. 2.9.

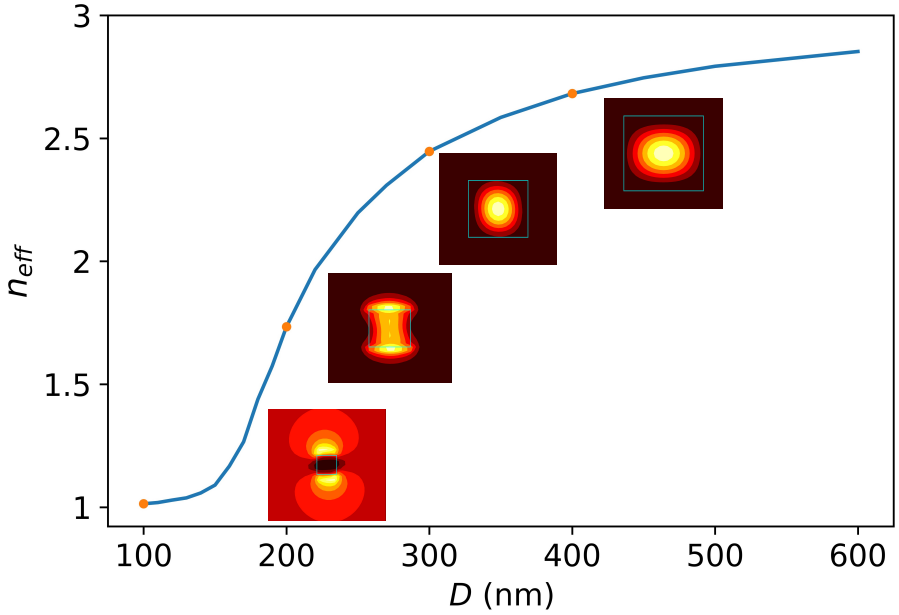

Figure 2.9: The effective refractive index of the fundamental mode of square-shaped waveguides of sizes varying from $100nm$ to $600nm$ is given. The four inset figures are the heat maps of the modes for sizes $D = 100nm$, $D = 200nm$, $D = 300nm$, $D = 400nm$.

There is a clear variation of n_{eff} between given waveguide sizes, and $n_{eff} \to n$ as $D \to \infty$. The distribution of electric field intensity of the fundamental mode at the cross-section of the waveguide is also given in the inset figures for certain values of D that are marked on the figure. Typically, the fundamental mode looks like the distributions in $D = 300nm$ and $D = 400nm$, which is a Gaussian function centered within the waveguide. If the width of the waveguide (D) is very short (eg. less than $100nm$), the effective refractive index reaches the index of the surrounding material because propagating modes are not supported.

Phase acquired by the propagating light can be expressed as

$$\Phi_{WG} = \frac{2\pi}{\lambda_d} n_{eff} H \tag{2.21}$$

where λ_d is the operating frequency, n_{eff} is the effective refractive index, and H is the length of the waveguide. Now, consider the same system, but the waveguide is rectangular-shaped with unequal sizes in x and y, where we define the width of two sides $W1$ and $W2$

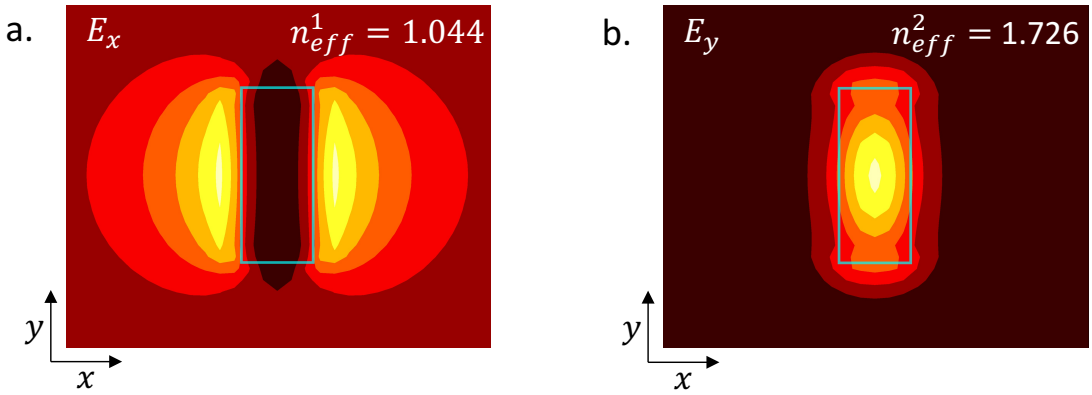

Figure 2.10: The fundamental x-polarized mode (a) and the fundamental y-polarized mode (b) of a waveguide with dimensions $100nm \times 300nm$ is plotted as a heat map, where the brighter regions correspond to higher intensity. The cross-section of the waveguide is outlined and the associated effective refractive index of the mode is given.

respectively.

Taking $W1 = 100nm$ and $W2 = 300nm$, the intensity distribution of fundamental modes of E_x and E_y are given in Fig. 2.10 a and b respectively. In a, light is guided from the outside of the waveguide due to its small size, while in b light is inside the waveguide. The corresponding effective refractive indices are $n^1_{eff} = 1.044$ and $n^2_{eff} = 1.726$ for E_x and E_y polarizations. The asymmetry of the waveguide reduces the n_{eff} value associated with a square-shaped waveguide of same size, which was found to be 1.0139 for $D = 100nm$ and 2.447 for $D = 300nm$. However, there is a clear difference between the two effective refractive indices. E_x and E_y components will gain different phases, which means the waveguide acts as a birefringent element. A HWP can be constructed if the phase difference gained by the two polarization states differ by π rad. This condition can be expressed as

$$\Delta\Phi_{WG} = \frac{2\pi}{\lambda_d} \left| n^1_{eff} - n^2_{eff} \right| H = \pi \tag{2.22}$$

Rectangular waveguides can operate as HWP's, and due to their shape, rotating them to induce geometric phase is not challenging. Therefore, they are good candidates for the dielectric metasurface phase elements.

We have assumed no reflection as light travels from air to the waveguide, but there will be some reflection described by Fresnel coefficients (Eqn. 2.10). For example, as

light travels from air to glass ($n = 1.5$), 4% of light is reflected for both polarizations, assuming normal incidence. Higher values of n will cause larger reflection. For example, if our material has $n = 3$, the amount of light getting reflected becomes 25%, and r_p and r_s will have a stronger dependence on the angle of incidence. High amount of reflection can interfere with the phase transmitted light acquires. In order to account for the reflected light, waveguide dimensions are set when the net electric field at the output has π phase difference.

2.5 Fabry Pérot Cavity

2.5.1 Cavity Parameters

A simple cavity can be constructed by positioning two parallel mirrors apart by a distance d, so that light is confined between the two mirrors. This structure is called a Fabry Pérot cavity. Let's consider the system in Fig. 2.11 a. The mirrors have complex reflectivity coefficients r_1 and r_2 and transmission coefficients t_1 and t_2. Light that transmits into the cavity will either leave the mirror via mirror 2, or reflect from mirror 2 for a round trip. There will be additional phase shift of e^{i2mkd} for m number of round trips. Therefore, in the transmission side, there will be field components with $m = 1, 2, 3....$ We would like to find the transmission coefficient T, so we can write down the field transmitted though the cavity as

$$E_T = E_0 t_1 t_2 + E_0 t_1 (r_2 r_1 e^{i2kd}) t_2 + E_0 t_1 (r_2 r_1 e^{i2kd})^2 t_2 + ... \tag{2.23}$$

$$= E_0 t_1 t_2 \left(1 + (r_2 r_1 e^{i2kd}) + (r_2 r_1 e^{i2kd})^2 + ...\right) \tag{2.24}$$

$$= \frac{E_0 t_1 t_2}{1 - r_1 r_2 e^{i2kd}} \tag{2.25}$$

In the final step, the property of geometric series is used with the assumption $r_1 r_2 e^{i2kd} < 1$, which should hold for all possible values of r_1 and r_2. We will only consider the case where the two mirrors have the same reflectivity and transmission, so $r_1 = r_2 = r$ and $t_1 = t_2 = t$. The reflection of one mirror is defined as $R = r^2$. The transmission coefficient for the whole system is then given as

$$T_c = \left|\frac{E_T}{E_0}\right|^2 = \frac{1}{1 + \left(\frac{2\mathcal{F}}{\pi}\right)^2 \sin^2(kd)} \tag{2.26}$$

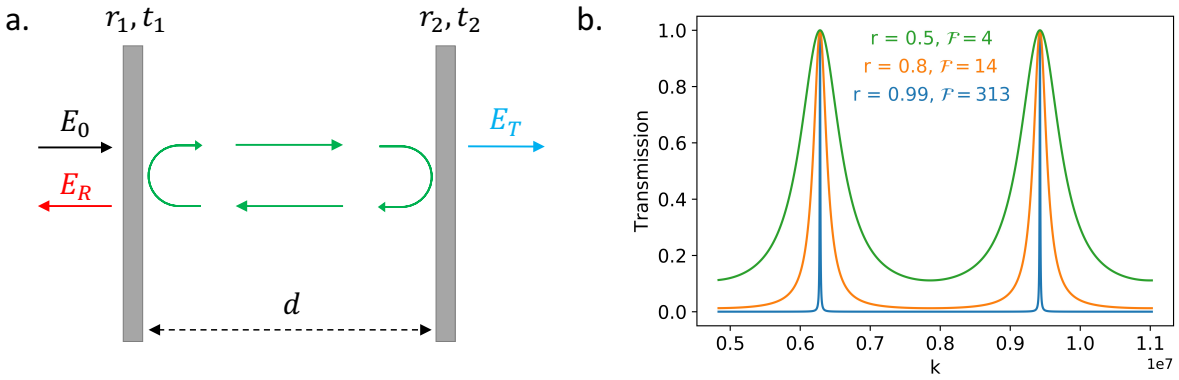

Figure 2.11: (a) Fabry Pérot cavity diagram where the two mirrors have reflection and transmission coefficients r_1, t_1 and r_2, t_2. The cavity has the size d and electric fields corresponding to incident, reflected and transmitted light are given in the figure. (b) The transmission through the cavity is given for different values of finesse.

where $\mathcal{F}$ is the finesse of the cavity, expressed as

$$\mathcal{F} = \frac{\pi\sqrt{R}}{1-R} \tag{2.27}$$

Finesse depends only on the reflection coefficient, so it quantifies how much light is confined within the cavity. The transmission spectrum for different finesse values are given in Fig. 2.11 b. The peaks correspond to a transmission of 1, regardless of r and t, but the minimum transmission depends on r and t. The peaks occur when the forward propagating light destructively interferes with the backwards travelling light before the first mirror and constructively interferes after the second mirror. This happens when the optical path length (size of the cavity multiplied with the refractive index of medium between mirrors, 1 in this case) between transmitted light through the first mirror and the light reaching the first mirror after one round trip is an integer multiple of the wavelength, so it depends on the cavity size.

Consider the electric field as it travels through a round trip in the cavity, $E(t)$. If the medium between the mirrors are free-space and mirrors have reflection coefficients r, then the electric field after one round trip is reduced to

$$E(t_1) = E(t=0)e^{i\omega_0 t_1} r^2 \tag{2.28}$$

We can also define a quantity called the quality factor (Q) of a cavity as

$$Q = 2\pi \frac{\text{Optical energy stored in the cavity}}{\text{Optical energy lost in one round trip}} \tag{2.29}$$

An alternative definition related to the broadening of the cavity resonance frequency is $Q = \omega_0/\Delta\omega$, where ω_0 is the resonant frequency of the cavity and $\Delta\omega$ is the full-width at half-maximum (FWHM) of the resonance. If the cavity is completely lossless, $\Delta\omega \to 0$ and $Q \to \infty$. However, any physical cavity will have some loss mechanism due to less than unity reflection, material loss, or light escaping from the cavity by other means etc. The quality factor is another quantity to describe the performance of the cavity.

For a lossy cavity, the electric field inside the cavity evolves by the following expression

$$E(t) = E(t=0)e^{-\omega_0 t/2Q}e^{i\omega_0 t} \tag{2.30}$$

The second exponential term is the oscillatory evolution over time, but the first exponential term describes the decay over time. The decay rate is $\omega_0/2Q$, which is inversely proportional to the quality factor. The two expressions for the electric field as a function of time (Eqn. 2.28 and 2.30) can be equated at t_1, i.e. time for one round trip, to find an expression for the quality factor.

$$r^2 = e^{-\omega_0 t_1/2Q} \quad \to \quad 2\ln r^2 = -\omega_0 t_1/Q \quad \to \quad Q = \frac{-\omega_0 t_1}{\ln r^4} \tag{2.31}$$

Time of one round trip can be written as $t_1 = 2d/c$. Putting this into the expression, the quality factor for this system can be written as

$$Q = \frac{-2\omega_0 d}{c \ln R^2} \tag{2.32}$$

Finally, we can define the mode volume of a cavity as

$$V = \frac{\iiint_V \epsilon(\mathbf{r})|\mathbf{E}(\mathbf{r})|^2 \, d^3\mathbf{r}}{\max\left[\epsilon(\mathbf{r})|\mathbf{E}(\mathbf{r})|^2\right]} \tag{2.33}$$

The numerator is the integral of the intensity within the cavity, and the denominator is the maximum intensity. Mode volume directly depends on the size of the cavity in all axes, as well as having high intensity due to confinement of light.

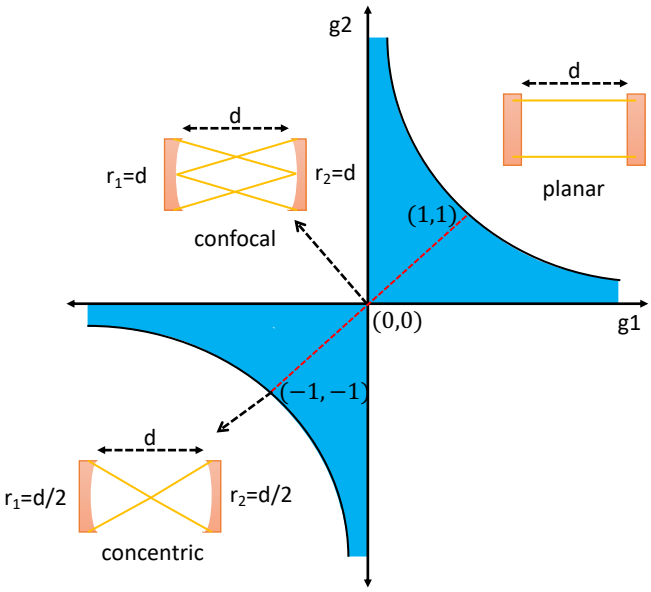

Figure 2.12: Cavity stability curve, where the blue region is considered to form a stable cavity. Three cavity types are given in the figure at various regions of the curve.

2.5.2 Cavity Stability

When constructing a cavity, it is important to consider the stability, i.e. is light truly confined within the cavity? For example, the Fabry Pérot cavity given in Fig. 2.11 has planar mirrors. This configuration is very sensitive to angular misalignments of the mirrors, and light can escape the cavity by a significant amount in such case. One option is to replace planar mirrors with concave mirrors. Diagram in Fig. 2.12 shows the region of stable cavities as a function of mirror and cavity parameters. The g parameter is given as $1 - d/r$ for each mirror, where r is the radius of curvature. r is related to the focal length as $r = 2f$, so we redefine $g_i = 1 - d/2f_i$. The red dashed line represents symmetric mirrors, $g_1 = g_2$. As marked on the figure, planar mirrors are right at the edge of the stability region. Confocal cavity, where $d = 2f$, lies at the center of the region. One can construct a confocal cavity with some cavity size d_0, then change the cavity size by small amounts. This will allow the cavity to lie along the dashed line but slightly off from the center in the stability curve, so that the cavity will be stable. As the cavity size and focal length of mirrors are related, the possible cavity sizes need to be considered for the design of the individual mirrors and their focal lengths.

Table 2.2: List of relevant Jones vectors and matrices

Polarization	Jones Vector
$H(x)$	$\begin{pmatrix}1\\0\end{pmatrix}$
$V(y)$	$\begin{pmatrix}0\\1\end{pmatrix}$
D	$\begin{pmatrix}1\\1\end{pmatrix}/\sqrt{2}$
A	$\begin{pmatrix}1\\-1\end{pmatrix}/\sqrt{2}$
L	$\begin{pmatrix}1\\i\end{pmatrix}/\sqrt{2}$
R	$\begin{pmatrix}1\\-i\end{pmatrix}/\sqrt{2}$
Optical Element	**Jones Matrix**
Linear (x) Polarizer	$\begin{pmatrix}1&0\\0&0\end{pmatrix}$
Linear (y) Polarizer	$\begin{pmatrix}0&0\\0&1\end{pmatrix}$
QWP	$\begin{pmatrix}1&0\\0&\pm i\end{pmatrix}$
HWP	$\begin{pmatrix}1&0\\0&-1\end{pmatrix}$

Chapter 3

Early Design Analysis

In this chapter, we will put together the ideas that were introduced previously. In Section 2.3, it was shown how geometric phase method can be applied to achieve the two unique characteristics of the mirror: circular polarization (CP) state preservation and focusing. In Section 2.4, the working principle of dielectric waveguides acting as a HWP to apply the theory of geometric phase was discussed. Now, we can develop the design of a CP state preserving metasurface focusing mirror. First, the key points and choices that need to be made will be explained. Second, a nanopillar design will be introduced, and its performance will be discussed. This design is an early version of the final product and has some performance issues. Finally, the diagnosis of these issues will be studied, which leads to Chapter 4, where the final product and its results are listed. The goal of this chapter is to introduce how one can develop a metasurface design and to highlight what kind of design choices can result with performance reduction. Throughout the chapter, simulations are run in Lumerical's Finite Difference Time Domain (FDTD) method unless otherwise stated. Simulation details are given in Appendix B and the code used in Appendix C.

3.1 Construction of the Unit Cell

In order to develop the design for this metasurface mirror, a step-by-step approach should be taken.

1. The initial step is to decide what the layers will be, materials used for the layers and the operating wavelength of the device. For this project, the operating wavelength

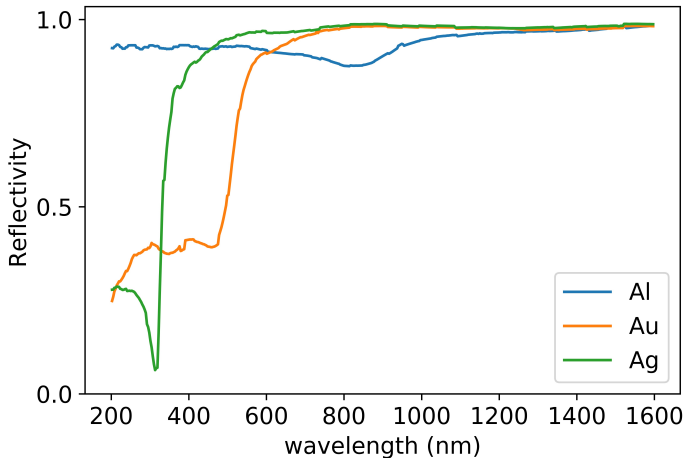

Figure 3.1: Reflectivity spectrum of aluminium (Al), gold (Au) and silver (Ag).

was chosen to be $850nm$ because the product is expected to be used in experiments involving cesium atoms, which have the D2 transition line at $852nm$ [47]. The main layers are the mirror and dielectric layers. The mirror layer executes the reflection of light. The two good candidates for the mirror are Bragg mirror, which is a periodic structure of dielectric layers that can be constructed for any operating wavelength, and metallic mirror, which is a thin layer of metal that has low absorption at near-infrared wavelengths. In order to reach high reflectivity, a Bragg mirror needs high periodicity (~ 20), which would make the total size in the order of micrometers. Therefore, for its simple and compact structure, metallic mirror is chosen. The most common metals used for reflection purposes are aluminium, silver and gold. Metallic sheets of thickness $100nm$ are simulated. The reflection spectrum for each material are given in Fig. 3.1. Among the three metals, gold and silver have the highest reflectivity at $850nm$, so silver is chosen with $R = 0.987$.

The dielectric layer consists of a rectangular nanopillar (i.e. the phase element) that is a HWP and has rotational freedom, and its material need to be determined. The final mirror should be as lossless as possible, so the main criteria is low extinction ratio. The extinction ratio is the imaginary component of refractive index and it determines the decay in the field as light propagates through the material. In literature, dielectric metamaterials are commonly devised using silicon nitride (SiN, $n \sim 2$) [58, 16], titanium dioxide (TiO2, $n \sim 2.4$) [29, 23] and amorphous silicon (a-Si, $n \sim 3.6$) [4, 3]. The extinction ratios of silicon nitride and titanium dioxide are negligible while amorphous

silicon has a non-zero extinction ratio according to Pierce *et al.* [39], but has zero extinction ratio for wavelengths $> 670nm$ according to Arbabi *et al.* [3]. Considering the extinction ratio and the practicality of their fabrication, SiN is chosen for the dielectric layer.

2. The parameters of the unit cell design (except for $W1$ and $W2$) need to be determined. The aspect ratio of nanopillars (ratio of width to height) should be large enough so that nanopillars are not too tall or too thin, as nanoscale features with high aspect ratios are difficult to fabricate. Also, nanopillars should be tall enough for its birefringence to implement significant phase differences, which is the H term in Eqn. 2.21. Therefore, the height is fixed at $500nm$. The periodicity of the structure (U) is limited by the operating wavelength from above (as described in Section 2.1), so $U < 850nm$. Also, shorter U allows a higher numerical aperture of the mirror. U is limited from below by fabrication limitations of nanopillar sizes. As a starting point, U is set to $500nm$.

   Finally, the thickness of the metallic layer needs to be determined. The reflectivity and transmission of the mirror can be varied by changing the thickness of the layer. The reflectivity and transmission of the metallic layer can be calculated by matrices where the reflected and transmitted light are related to the incident light by a matrix.

   Consider three regions with refractive indices n_1, n_2 and n_1 (see Appendix D for the diagram). The three regions can be interpreted as air, metallic layer, and air again for this case. Light is incident on the right and travels through the three regions in order. The electric field in the first region can be written as $E_1 = A_1 e^{-ik_1 x} + B_1 e^{ik_1 x}$ where $k_1 = 2\pi n_1/\lambda$ and A_1 and B_1 are the coefficients of forward and backward (reflected) travelling waves respectively. Similarly the electric field in the third region can be written as $E_3 = A_3 e^{-ik_1 x}$ where A_3 is the coefficient of the forward travelling wave (transmitted). There is no B_3 because there is no backwards-travelling light from the third region. The coefficients are related by a matrix $\mathbf{M}$ such that

$$\begin{pmatrix} A_3 \\ 0 \end{pmatrix} = \mathbf{M} \begin{pmatrix} A_1 \\ B_1 \end{pmatrix} = \begin{pmatrix} M_{00} & M_{01} \\ M_{10} & M_{11} \end{pmatrix} \begin{pmatrix} A_1 \\ B_1 \end{pmatrix} \tag{3.1}$$

   The components of the matrix and the derivation of the matrix can be found in Appendix D. This expression is equivalent to two equations where the unknowns are A_3 and B_1, since the matrix elements are known and A_1 is the component of the incident field. The reflectivity is equal to

$$R = \left| \frac{B_1}{A_1} \right|^2 = \left| \frac{M_{10}}{M_{11}} \right|^2 \tag{3.2}$$

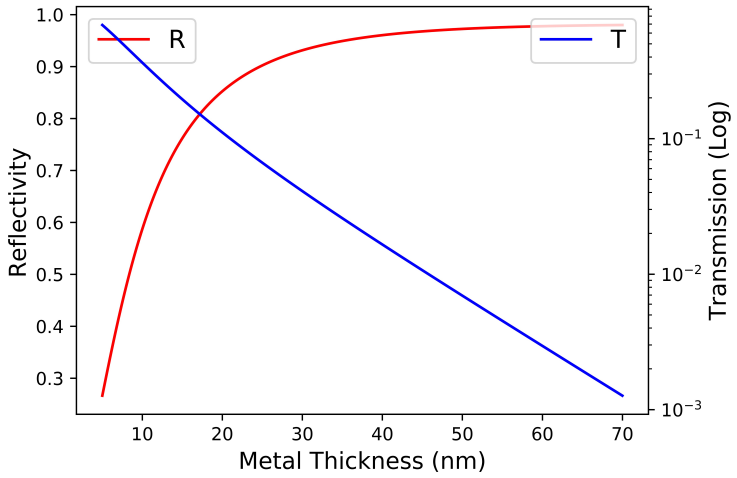

Figure 3.2: Reflectivity (red) and transmission (blue) of the silver metallic layer over thickness of the layer, calculated by matrices. The transmission is given in logarithmic scale.

Similarly, transmission is expressed as

$$T = \left|\frac{A_3}{A_1}\right|^2 = \left|M_{00} - \frac{M_{01}M_{10}}{M_{11}}\right|^2 \tag{3.3}$$

Using these expressions, the reflectivity and transmission of the metallic layer is calculated for varying thicknesses. The results are given in Fig. 3.2. Although highest reflectivity is desired for strong light-matter interactions, a non-zero transmission is required to couple light into the cavity. Therefore, the thickness is set to $50nm$. The associated reflectivity is 97.2% and transmission is 0.8%. The remaining 2% is lost in the structure. The final unit cell structure is given in Fig. 3.3.

3. Now, $W1$ and $W2$ are left to determine the unit cell structure of the mirror design. The nanopillars are expected to induce a π rad. phase difference between E_x and E_y to act as HWP's. First, let's determine if the nanopillars induce the required phase difference by a proof-of-concept simulation. A periodic structure of the given unit cell with already-determined parameters is built, except the metallic layer is build up by a Perfect Electrical Conductor (PEC), which is a built-in structure to Lumerical that acts as a perfect metallic mirror to make sure no unwanted resonances or excitations within the metallic layer occur. Light is incident on the structure from above and is given as

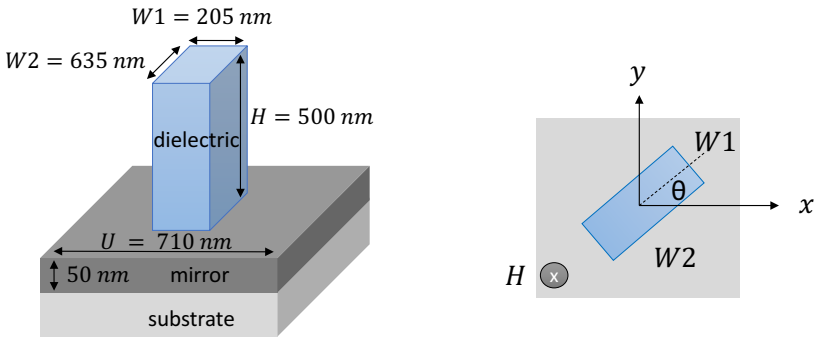

Figure 3.3: Unit cell design of the metasurface mirror. The dielectric nanopillar is SiN, the spacer is SiO2 and the mirror is silver. On the right, a top view of the unit cell is given to define the rotation angle of nanopillars.

$$\mathbf{E_i} = E_0 e^{i(kz-\omega t)} \left(\hat{\mathbf{i}} + \hat{\mathbf{j}}\right) \tag{3.4}$$

It is linearly polarized, so it does not have relative phase difference between E_x and E_y. After reflection, both components of the electric field are expected to have gained certain phase, depending on the shape of the nanopillar. The nanopillar is first set to have square cross-section, so $W1 = W2 = 100nm$, and $W2$ is increased while $W1$ is kept constant. The phases of E_x and E_y, along with their differences are plotted in Fig. 3.4.

As expected, at $W2 = 100nm$ the phase difference is 0. As $W2$ is increased, E_y reaches a phase of 0.5π rad. However, the phase of E_x also increases to a phase of 0.1π rad. In Section 2.4, it was shown that a change in size in one axis can slightly affect the n_{eff} experienced by the electric field component in the other axis. This is the reason behind the increase in phase of E_x, even though $W1$ is kept constant. Regardless, we observe a clear increase in the phase difference as the structure becomes more asymmetric. It must be noted that the phase difference is only 0.4π rad., which is much lower than the expected π rad. phase. The index of SiN, $n = 2$, is quite low to achieve large phase difference.

In order to reach the required phase difference, U is gradually increased in small steps. At each U, possible ranges of $W1$ and $W2$ are scanned over by simulating the structure and extracting the phase difference. A higher value of U allows a better contrast of nanopillar widths, achieving higher phase differences. Finally, nanopillar dimensions

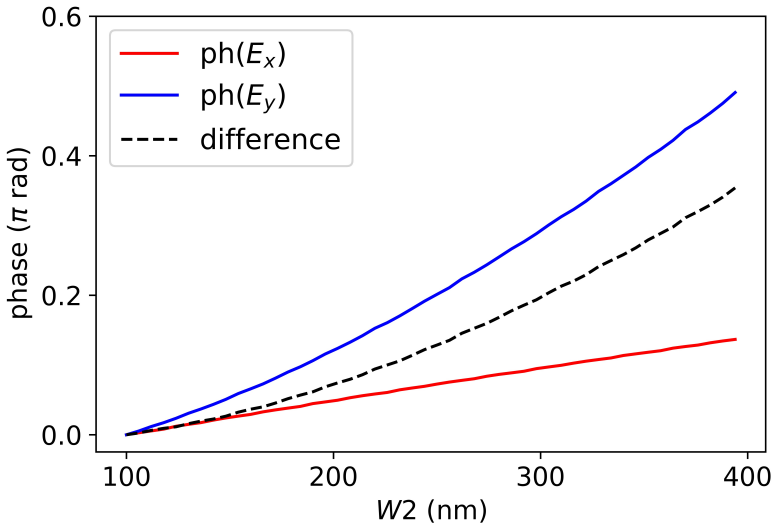

Figure 3.4: The results of the proof-of-concept simulation where $W2$ of the nanopillar is increased, starting from $W2 = W1 = 100nm$, where $U = 500nm$. The nanopillars are made of silicon nitride with refractive index $n = 2$. The phase gained by E_x and E_y are shown in red and blue respectively, along with their difference (dashed line).

that impart π rad. phase difference is found: $W1 = 205nm$, $W2 = 635nm$ and $U = 710nm$. This concludes the unit cell design.

4. The final step is to construct the mirror using the unit cell design that is determined. It was established in Section 2.3 that rotation of optical elements impart geometric phase by the relation $\phi = 2\theta$. To construct a focusing mirror, the nanopillars need to be rotated following the spherical wavefront function given in Eqn. 2.18. This function is the phase distribution of the wavefront in the $x - y$ plane, given the light propagates in the z direction. The nanopillars are rotated according to their positions (x, y), but there is still an unknown, which is the focal length f of the mirror being constructed. The focal length is determined freely depending on the application and considering the cavity size to satisfy stability condition explained in Section 2.5.2. The construction and analysis of a mirror will be discussed in Chapter 4.

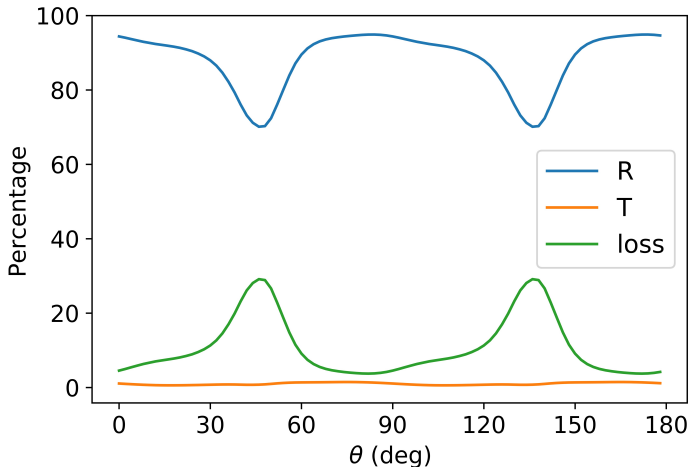

Figure 3.5: Reflectivity (blue), transmission (orange) and loss (green) of the unit cell structure are given over nanopillar angles.

3.2 Unit Cell Simulation Results

Now, the design is analysed for CP state preservation and geometric phase. While we maintain the infinite crystal structure of the unit cell design, the orientation angle of the nanopillar is swept from 0 to 180 deg. (equivalently 0 to π rad). This range is sufficient to cover the required $0 - 2\pi$ rad. geometric phase. For this analysis, the incident wave is changed to RHCP, given in Eqn. 2.8. The reflection and field information are recorded after reflection. The analysis includes reflection, transmission, the amount of RH and LH component after reflection, and the phase acquired by the RH component. Ideally, no LH component should be detected at the output.

The design gives a phase difference of $3.142 \approx \pi$ rad. and a reflectivity of $R = 0.944$ at $\lambda = 850nm$ and $\theta = 0$ deg.

Reflectivity (R), transmission (T) and the amount of loss is given in Fig. 3.5. The loss is defined as $1 - (R + T)$. Due to the symmetry of the structure, nanopillars oriented at θ should have the same result at $\theta + 90$deg. The reflectivity, transmission and loss pattern of this structure for the first 90 deg. is repeated in the second half of the data. High reflectivity is maintained at low angles, but especially between 25 and 70 deg., reflectivity drops significantly to 65%. The energy lost does not get transmitted but is lost inside the structure. Transmission is close to $\sim 0.8\%$ with insignificant variations.

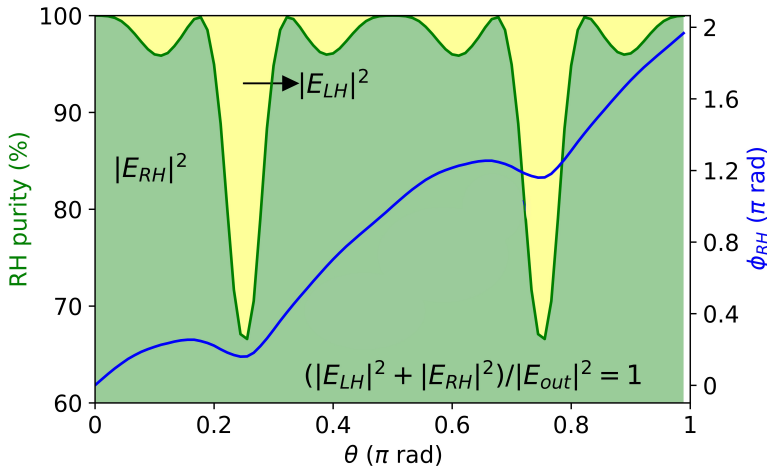

Figure 3.6: Right handed (RH) purity is shown by the green region, and left handed (LH) component is the yellow region by percentage over nanopillar angles. The blue curve shows the geometric phase on RH component, ϕ_{RH}, which should satisfy $\phi = 2\theta$. The data for RH purity is given in the left $y-$axis and the data for geometric phase is given in the right $y-$axis.

The amount of RH component preserved upon reflection has an equal significance to having high reflectivity. Any CP state impurity, i.e. LH component, will cause some amount of light to be lost. Now the same simulation results are analysed for the CP state at the output. The reflected light is separated into the RH and LH components, and their intensity and phases are calculated. A quantity called RH purity is defined as the intensity of RH component relative to the intensity of the output field. This implies the following normalization

$$|E_{RH}|^2 + |E_{LH}|^2 = |E_{out}|^2 \tag{3.5}$$

where $|E_{RH(LH)}|^2$ is the intensity of the RH (LH) component and $|E_{out}|^2$ is the intensity at the output. This allows the separation of material loss and impurity of CP state.

In Fig. 3.6, the purity and phase of the RH component is given in green and blue respectively. The $x-$axis is given in the unit of radians, so that the comparison with the geometric phase will be clearer. The geometric phase is normalized such that at $\theta = 0, \phi = 0$. Similar to the previous result, the design performs well at 0 rad. However, there is a 4% decrease in purity at angles $0.1\pi, 0.4\pi...$ rad, and a strong dip to 70% at 0.25π

rad. (45 deg). As explained in Section 2.3, the rotation of nanopillars ($x-$axis) and the geometric phase (blue curve) should have 1:2 relationship, following Eqn. 2.17. Overall, the 1:2 mapping is observed. However, the relation is not linear as expected, with the imperfection recurring at the 0.25π rad. position.

Although the design performs well at $\theta = 0$ deg., its performance decreases significantly as the nanopillars are rotated, so the design is not suitable for the final product. This performance issue is diagnosed in Section 3.3, and it will lead us to the better-performing design in Chapter 4.

3.3 Problem Diagnostics

There are two hypotheses to the cause of the problem: Plasmonic excitations inside the silver layer that result in absorption, and cross-coupling between adjacent nanopillars that disturbs the propagation mode.

3.3.1 Absorption in Metal

The first proposed issue is the loss due to absorption in the metal. First, all the layers in the structure are covered with 2D monitors that record the transmission of light through the surface covered by the monitor. Therefore, the amount of light going in and coming out of all the layers are measured. The source of the 35% loss in the structure reveals itself in the metallic layer.

For wavelengths greater than $\sim 400nm$, metals have high reflectivity. However, a small amount of light gets absorbed as the light excites electrons. According to the Drude-Sommerfeld model describing metals [36], the electrons in the metal are not bound, i.e. free to move around, and their resonance frequency is at plasma frequency ω_p, at which the absorption should be maximum. For silver, the wavelength corresponding to the plasma frequency is $130nm$ [11], which is much shorter than the operating wavelength. The amount of absorption of the silver layer is found as 2% at $850nm$ without the nanopillars. However, the field distribution arising from the presence of the nanopillars can result in higher losses compared to a simple silver layer.

The unit cell structure is simulated where the nanopillars are oriented at 0 deg. first, then at 45 deg. The magnitude of Poynting vector through a cross-section of the structure in the $x - z$ plane, where $y = 0nm$ is recorded for both cases. Poynting vector is defined

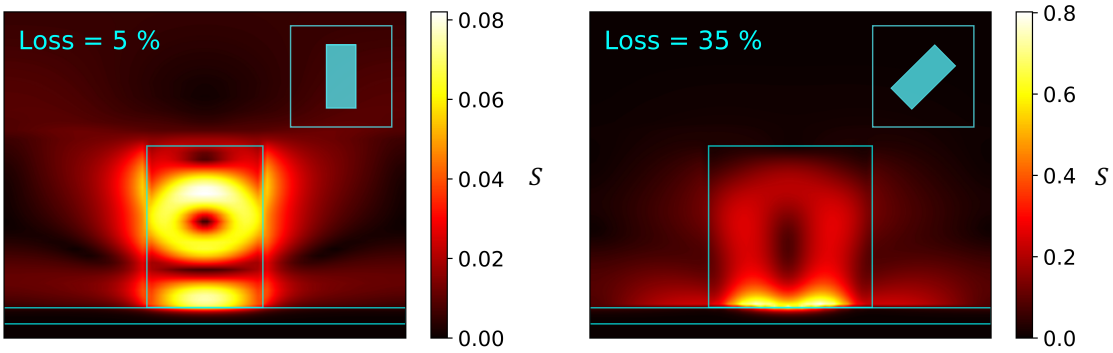

Figure 3.7: The distribution of the Poynting vector magnitude in the $x-z$ plane of the unit cell when the nanopillar is oriented at 0 deg (left) and at 45 deg (right). The outline of the unit cell structure and angular orientations of nanopillars are sketched on the figure. The associated loss through the structure for each nanopillar orientation is also given.

as the directional electromagnetic energy flux [22], and is given as $\mathbf{S} = \mathbf{E} \times \mathbf{H}$ where $\mathbf{H}$ is the magnetic field vector inside the material. It quantifies the electromagnetic energy carried by the propagation of light at a given point. The distribution of $|\mathbf{S}|$ through the cross-section of the structure is given in Fig. 3.7 for $\theta = 0$ deg. (a) and $\theta = 45$ deg. (b). At $\theta = 0$ deg., the Poynting vector has a ring shape, and the power is distributed somewhat evenly within the nanopillar. However, at $\theta = 45$ deg., at which the strong loss occurs, the Poynting vector is very strong at the dielectric-metal interface. Although the magnitude of the distribution is redundant, there is one order of magnitude difference in the two cases. Poynting vector inside the metal is also non-zero near the highest energy density region for both cases, but the energy is 10 times larger for the second case. This can excite the electrons and phonons more strongly and cause larger amounts of loss.

The metallic layer is replaced with PEC to analyse the performance of the structure by eliminating the metallic effects, and the same simulations are run. The results (solid), along with the previous results (dashed) are given in Fig. 3.8. In Fig. 3.8 a, the loss disappears and the reflectivity is 100%. This means that the strong decrease in reflectivity is due to the metallic absorption and that there is no absorption in the dielectric layer. In Fig. 3.8 b, the strong, narrower dip is lost, but a weaker, wider loss in the RH component still exists. This is an indicator that it is not explained by the metallic absorption, but by some other phenomena. The geometric phase acquired by the RH component also improves and is very smooth, and satisfies the relation $\phi = 2\theta$.

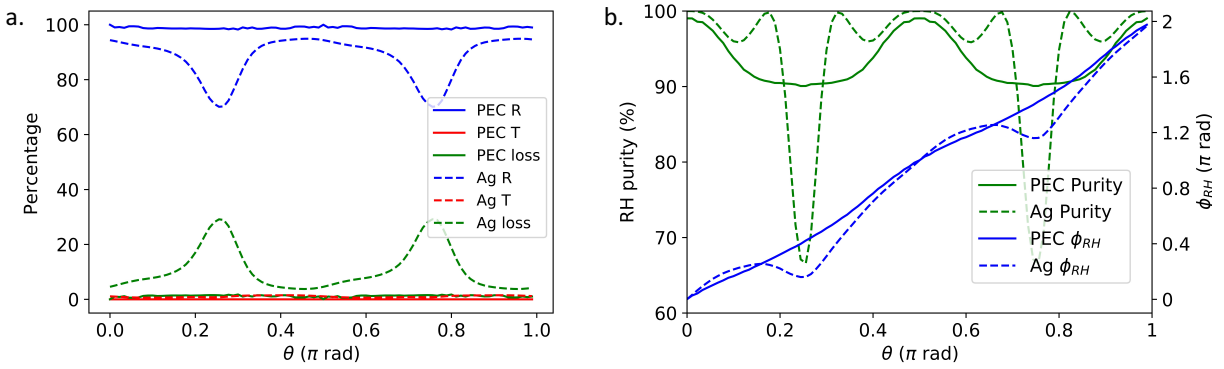

Figure 3.8: (a) Reflectivity (blue), transmission (red) and loss (green) of the unit cell structure over rotation of nanopillars between 0 and π rad. (b) RH purity (green) and the geometric phase acquired by RH component (blue) of the unit cell structure over rotation of nanopillars between 0 and π rad. The solid curves correspond to the case where the metallic mirror is replaced with PEC, and dashed curves are the results with the silver mirror.

3.3.2 Cross-Coupling

The second proposed cause of impurity is the cross-coupling between nanopillars that act as waveguides, which is called evanescent waveguide coupling (EWC). EWC occurs when two waveguides are in close proximity and the field inside one waveguide leaks into the second waveguide. Usually, this condition is taken advantage of to transfer light between waveguides, most commonly to excite ring resonators [12]. Here, this phenomena is unwanted, and the extend of its effect is analysed.

Let's call the modes that are travelling through the nanopillars the propagation mode, which is independent of the surrounding waveguides, and let's call the mode that exists due to a neighbouring waveguide the coupled mode. Using Lumerical's MODE analysis tool, the two modes are simulated. The simulation details can be found in Appendix A. In Fig. 3.9 a, the system under consideration is sketched. The dark blue region is the cross-section at which the modes are simulated. The waveguides have the dimensions of the nanopillars, which has a separation of $75nm$. Fig. 3.9 b shows the intensity profile of the coupled mode. The field is intense at the center of the two waveguides, but also the region between them is excited. This is clearly a result of having multiple nanopillars. Fig. 3.9 c shows the intensity profile of the propagation mode, where the field is most intense at the center and the intensity decays towards the end of nanopillars. The two

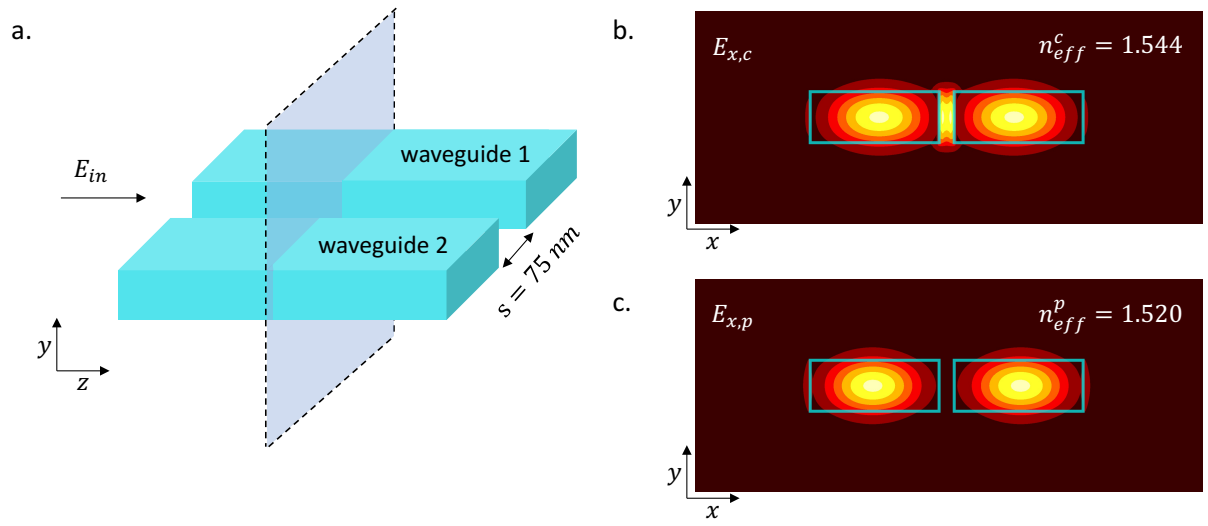

Figure 3.9: (a) Simulation setup of MODE analysis of two waveguides representing nanopillars in the metasurface design. The dark blue region is being simulated, and has size $2U \times U$. The modes supported in the shaded region are calculated. (b) The fundamental $x-$polarized mode profile (coupling mode) is plotted, and the associated n_{eff} is given. (c) The first higher order $x-$polarized mode profile (propagation mode) is plotted, and the associated n_{eff} is given.

fields propagate independently (no EWC). In both cases, the field is x polarized.

The coupled mode has a different n_{eff} than the propagation mode, and it is a function of separation of nanopillars. As nanopillars get closer to each other, the difference between n_{eff} of propagation and coupling modes become larger. This equivalently means more coupling occurs as nanopillars are closer.

Assume a system with two waveguides in close proximity. The field is injected into the first waveguide, while the second waveguide is empty. As light propagates through the first waveguide, it also leaks into the second waveguide.

The power of light coupled into the second waveguide is given in Eqn. 3.6. P_c is the power coupled to the second waveguide, P_0 is the initial power injected, L is the length of propagation inside waveguide, λ_0 is the wavelength of the field, and Δn is the difference in n_{eff} of the propagation and coupled modes.

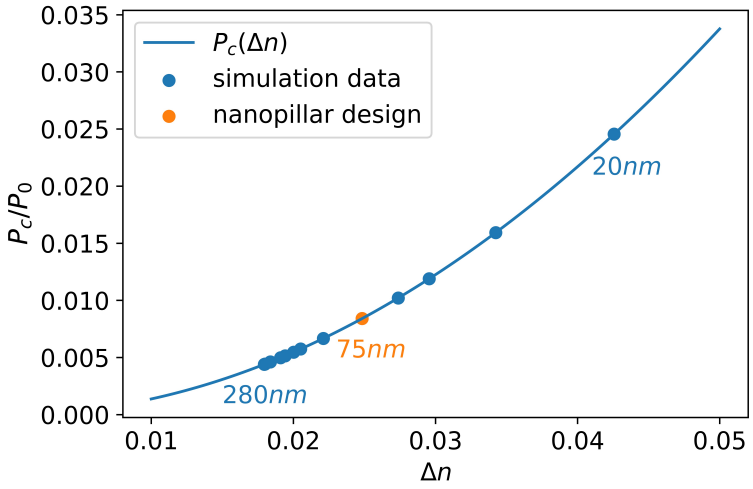

Figure 3.10: The ratio of coupled power to initial power when two waveguides are placed in close proximity. The solid line is the plot of Eqn. 3.6 and the dots are simulation data. The orange dot is the nanopillar separation of the design. The minimum and maximum waveguide separations are given below each data.

$$P_c = P_0 \sin^2\left(\frac{\pi L \Delta n}{\lambda_0}\right) \rightarrow P_c/P_0 = \sin^2\left(\frac{\pi L \Delta n}{\lambda_0}\right) \tag{3.6}$$

Δn is a function of waveguide separation, and is directly obtained from MODE simulations at wavelength of $850nm$. The first and second dominant modes are given in Fig. 3.9 b and c respectively for nanopillar parameters (separation of $75nm$). The mode in b is the coupled mode, and the associated n^c_{eff} is 1.544. The mode in c is the propagation mode, and the associated n^p_{eff} is 1.52. Δn in Eqn. 3.6 is the difference of the two: $\Delta n = |n^c_{eff} - n^p_{eff}| = 0.024$. This difference in the effective refractive indices of coupled and propagation modes is found for various nanopillar separations and the corresponding P_c/P_0 ratio is calculated according to Eqn. 3.6. The results are given in Fig. 3.10. The blue curve is the plot of Eqn. 3.6 and the dots are Δn obtained from simulations for various waveguide separations. The yellow dot is Δn of the design nanopillar separation, and the associated ratio is $P_c/P_0 \sim 0.0085$. In the rectangular lattice, one nanopillar is surrounded by 4 others, 2 of which are along the longer side. Assuming the central nanopillar is coupled to the 2 nearest nanopillars independently, we can extend our result to $2 \times P_c/P_0 \sim 0.017 = 1.7\%$. Taking the square root of this, 1.7% power coupling will result with a 13% coupling for the fields.

We concluded that in Fig. 3.8 b, the strong decrease in RH purity is due to the metallic layer, but there is 10% purity loss when the structure is simulated with a PEC layer. This can be explained by the excitation of the coupled mode disturbing the phase acquired by the propagation mode.

It should be noted that the RH purity is closest to 100% at $\theta = 0$ deg., but the distance between the nanopillars are smallest in this configuration. The distance goes up to $370nm$ when the nanopillars are oriented at 45 deg., which is significantly longer than $75nm$ at 0 deg. orientation. The analysis implies that the purity should be low when nanopillars are closer together (i.e. at 0 deg.), and it should be high at 45 deg. This is not necessarily true. The nanopillar dimensions are determined at 0 deg. orientation to provide π rad. phase difference, where the effect of EWC is at maximum. Then, as nanopillars are rotated, effect of EWC decreases, revealing the true phase difference induced by the propagation mode which is not exactly π rad. Therefore, the impurity is caused by the inconsistency in nanopillar separations, rather than EWC itself.

The large size of the nanopillars cause some EWC between nanopillars, which can explain the RH impurities that exist when the structure is simulated with PEC. Either the nanopillar sizes should decrease or the unit cell size should be larger. The latter is not feasible because U is limited by the wavelength, so the former will be attempted.

Chapter 4

Final Metasurface Mirror Design

The performance issues with the design in Chapter 3 was diagnosed to arise from accumulation of the field at the dielectric-metal interface and the resulting plasmonic loss inside the metallic layer. Additionally, close proximity of the nanopillars contributed to evanescent waveguide coupling, which was another factor to the poor performance of the design. Following these outcomes, major improvements were made to the design. In this Chapter, these improvements will be introduced, and the analysis of the improved design will be presented. Furthermore, the full-sized mirror will be constructed by selecting the size and focal length of the mirror, and its performance for CP state preservation and focusing will be analysed by simulations. Then, we will discuss how to couple light inside a cavity built by these mirrors. Finally, by extending the response of the mirror found in simulations numerically for multiple mirror bounces, we will simulate the mode of the cavity, and observe the effect of 15 roundtrips. Throughout the chapter, simulations are run in Lumerical's Finite Difference Time Domain (FDTD) method unless otherwise stated. Simulation details are given in Appendix B and the code used in Appendix C.

4.1 Updated Unit Cell

First, we discuss the updates made to the design. There are two major updates:

1. The main issue was found to be the accumulation of the field at the metal-dielectric interface. The proposed solution is to introduce a spacer between the two layers, made of a lossless material, to prevent the existence of the mode in Fig. 3.7 b. The material

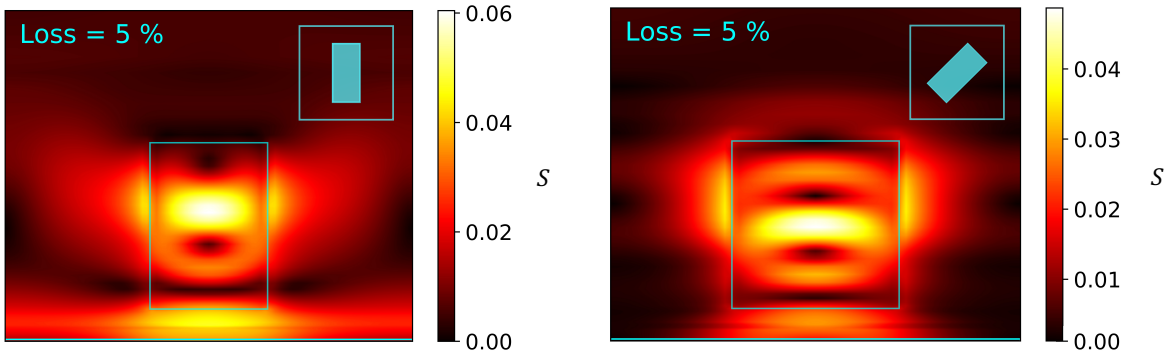

Figure 4.1: The distribution of the Poynting vector magnitude in the $x - z$ plane of the early mirror design, updated with a spacer. The two cases are for nanopillar angles of 0 deg. (left) and 45 deg. (right). The outline of the unit cell structure and angular orientations of nanopillars are sketched on the figure and the associated loss is given.

is chosen to be SiO2 because it has negligible loss, is robust, and is very flexible with fabrication in the sense that it can be placed between metallic layers or dielectrics. The thickness is set to $100nm$ and the new structure is simulated to check if the accumulation has disappeared. The distributions of the Poynting vector for $\theta = 0$ deg. and $\theta = 45$ deg. are given in Fig. 4.1. Although the spacer region has high magnitudes of Poynting vector, the loss is maintained at 5% as the nanopillars are rotated.

Later on, a more optimal spacer thickness has been found, but it was not incorporated to the design. A spacer thickness that provides an optical path of $\lambda/2$ is predicted to overcome the excitation of electrons in metal. For such optical path length, light propagating towards and away from the metallic layer will have equal magnitude but opposite direction of electric field, which will cause destructive interference. This will reduce the intensity of light at the surface of the metallic layer, thus reducing the electronic excitations. Therefore, the new proposed thickness is calculated by setting the optical path length $OPL = nt_{new} = \lambda/2$. As light goes through a higher refractive index material than air, it slows down. This causes the path taken by light to be longer than the physical length of the material. Using the expression for OPL, the new thickness is calculated as $t_{new} = 297nm$ for $n = 1.45$. The simulations show that the metallic loss is reduced to 2% when the spacer thickness is changed, so there is potential improvements to the design. The nanopillar dimensions need to be altered slightly to optimize the design. The new design is discussed in Appendix E.

This proposed solution (spacer with thickness of $100nm$) fixes the accumulation of the

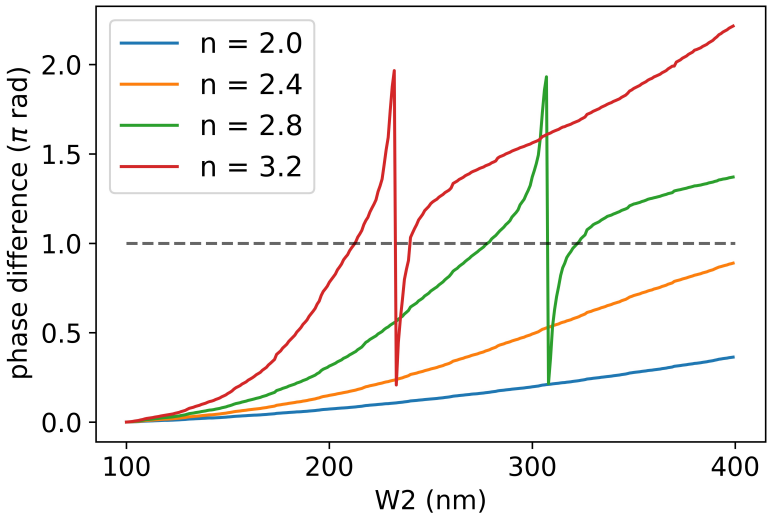

Figure 4.2: The phase difference acquired in simulations is given over $W2$ ranging from $100nm$ to $400nm$, where $W1 = 100nm$. This is repeated for different values of refractive index. $U = 500nm$ and $H = 500nm$.

energy at the boundary, and allows it to get distributed within the nanopillar. The results of the simulation show that the phase difference is 0.81π rad., while we achieved π rad. phase difference for the same structure without the spacer. The updated design was further simulated for different $W1$ and $W2$, but π phase could not be achieved for low refractive index. This leads to the second update.

2. It was shown that EWC has effects on the phase evolution of the field, which reduces the purity of RH component. The cause of EWC is that nanopillars are in close proximity, which is the result of using low index dielectric material. To understand the effect of refractive index on phase difference by a small increase in nanopillar asymmetry, the proof-of-concept simulation that was presented in Section 3.1 is repeated for different values of refractive indices. The phase differences obtained from the simulations is given in Fig. 4.2.

   The blue and yellow curves, corresponding to refractive index of 2 and 2.4 do not reach π rad. phase difference over the given domain of $W2$. The green and red curves, corresponding to refractive index of 2.8 and 3.2 reach π rad. phase difference at reasonable values of $W2$ that would give a nanopillar shape of good aspect ratio and long separations. The resonance jumps observed in these two curves can be ignored as long as

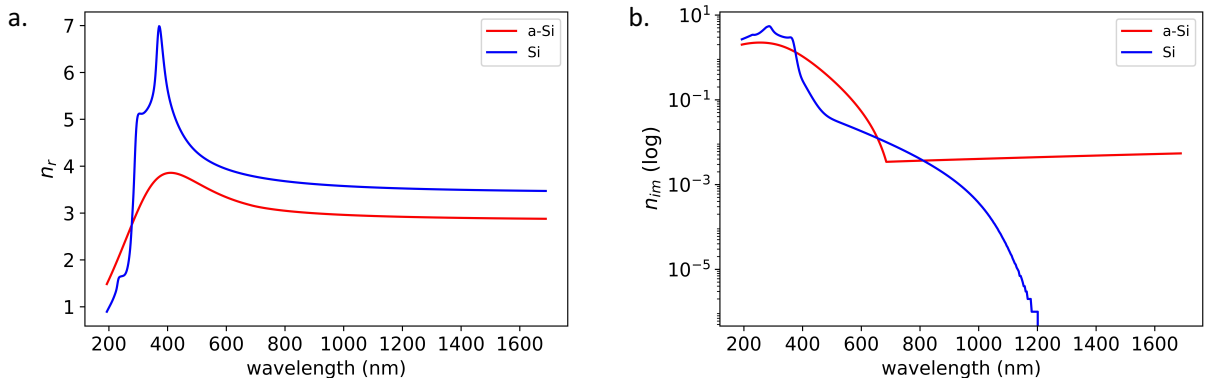

Figure 4.3: Experimental refractive indices of a-Si and Si. The real part is given in a, and the imaginary part is given in b with logarithmic scale.

the nanopillar design is far from these parameters. These resonances are explained in Zhan *et al.* [58]. Clearly, the refractive index of the nanopillars significantly affect their birefringence, and a higher index material would allow smaller sized nanopillars.

The material is switched to amorphous silicon (a-Si), which has a measured refractive index of 3.596 according to Arbabi *et al.* [3], and they have achieved a 0 extinction coefficient (imaginary component of refractive index) with their fabrication techniques. However, refractive index of this material highly depends on the fabrication techniques. Therefore, my colleague from our group, Dr. Rubayet Al-Maruf, has characterized a-Si and silicon (Si) that is deposited at University of Waterloo's Quantum Nanofab, so the simulation parameters will match the experimental parameters.

The experimental real and imaginary refractive indices are given in Fig. 4.3 a and b respectively. The imaginary component is also called the extinction ratio.

The relevant wavelength is $850nm$, so the data associated with this wavelength is listed in Table 4.1. The imaginary part is crucial to the design because it causes decay in the field and thus defines the amount of loss through the material. The decay can be calculated analytically, so that the material loss is predicted before the simulations. Recall that the magnitude of electric field with arbitrary polarization propagating in the z direction is represented as

$$E = E_0 e^{i(knz - wt)} \tag{4.1}$$

When the real and imaginary components are separated, this becomes

$$E = E_0 e^{i(kn_r z - wt) - kn_{im} z} \tag{4.2}$$

The last term in the exponential does not oscillate, but causes the decay of the field.

Now, consider the magnitude of the electric field at the output of a dielectric waveguide of length L. The magnitude of the incident electric field is E_i, and the output electric field is E_{out}. E_{out} is related to E_i by

$$E_{out} = E_i e^{-2\pi n_{im} L/\lambda} \tag{4.3}$$

where $k = 2\pi/\lambda$. By rearranging the terms, we get the ratio $1 - |E_{out}/E_i|^2$, that is the intensity lost through the material:

$$I_{lost} = 1 - |E_{out}/E_i|^2 = 1 - e^{-4\pi k L/\lambda} \tag{4.4}$$

For our structure, L is two times the height of the nanopillars, as light travels through the nanopillars twice, so $L = 1\mu m$. By inserting the n_{im} values from the experimental data, the expected material loss is calculated. The last column of Table 4.1 is the corresponding I_{lost}.

Table 4.1: Refractive Index and Corresponding Loss of a-Si and Si at $850nm$

Material	n_r	n_{im}	loss per μm
a-Si	3.018435	0.003752	5.4 %
Si	3.645301	0.002555	3.7 %

Both have similar amounts of losses, so, we choose a-Si considering it has a potential to reduce the imaginary component with improved fabrication techniques.

Applying the changes to the unit cell design, the new design is given in Fig. 4.4. The $W1$ and $W2$ are found similar to before, and the design successfully induces the π rad. phase difference when nanopillars are oriented at 0 deg. at $850nm$.

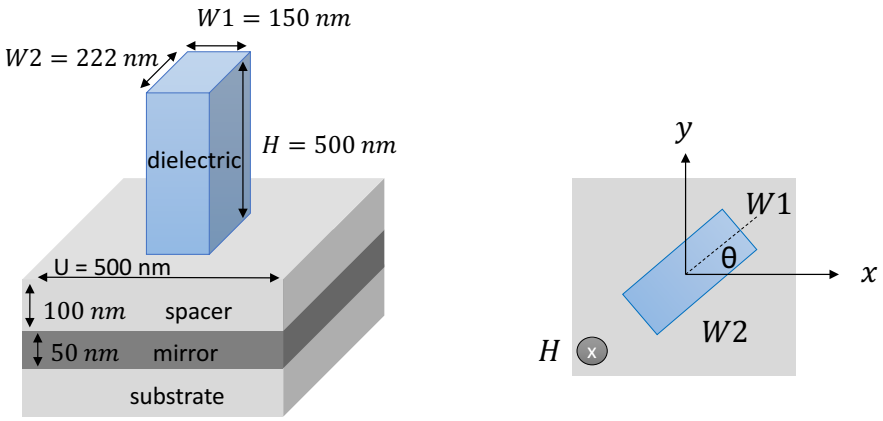

Figure 4.4: Unit cell design of the metasurface mirror. The dielectric nanopillar is a-Si, the spacer is SiO2 and the mirror is silver. On the right, a top view of the unit cell is given to define the rotation angle of nanopillars.

4.2 Unit Cell Performance Analysis

Similar to Section 3.2, the infinite crystal structure of the unit cell is simulated by rotating the nanopillars from 0 to 180 deg. to confirm the conservation of CP state, to verify the relation between θ and ϕ and to identify the sources of loss. Here, there are two loss mechanisms: material loss and CP state impurity. First is due to the energy dissipation through the materials, and second is due to any LH component left at the output of the structure. The structure is illuminated with a RHCP plane wave, and the reflected field is recorded at the output. High reflectivity and 100% RH component at the output are expected from the simulation results.

Fig. 4.5 shows the reflectivity (R), transmission (T) and loss of the structure when the nanopillars are rotated covering $0-180$ deg. about the z-axis. The results are constant through the domain, with values $R \sim 89.5\%$, $T \sim 1\%$ and loss$\sim 9.5\%$. Here, only material loss is observable, with 5.5% lost through the dielectric material and 4% lost through the metallic layer, measured by monitors recording the transmission in and out of each layer. The loss through the dielectric layer agrees with the calculated value, given in Table 4.1 as 5.4% per μm. The metallic loss of a silver sheet of thickness $50nm$ is 1.3% without nanopillars, but it increases to 4%. One possible source of this increase is the 25% Fresnel reflection from the dielectric layer (recall Section 2.4) which will cause light to undergo

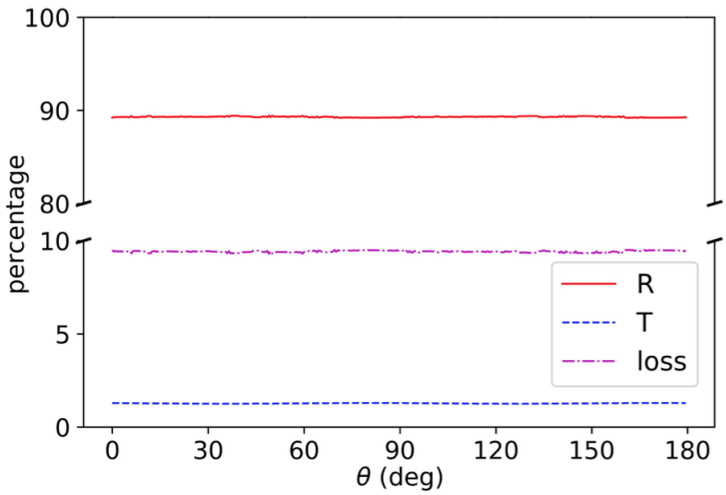

Figure 4.5: Reflectivity, transmission and loss of the unit cell design at $\lambda = 850nm$ are given over nanopillar angles θ.

many roundtrips within the spacer region, causing multiple reflections from the metal that might lead to additional loss.

The output field is separated into RH and LH components to observe the RH purity, which is defined as the percentage of RH component at the output by intensity, i.e. second term in Eqn. 2.16. Same definition applies to LH component, i.e. first term in Eqn. 2.16. This definition allows us to identify the success of CP state conservation while discarding the material loss. The purities follow the same normalization condition in Eqn. 3.5.

The green curve in Fig. 4.6 a shows the percentage of RH component, while the regions of RH and LH components are shaded in green and yellow respectively. 99.6% of the output is RHCP, which confirms that structure is highly CP state preserving. The remaining 0.4% contributes to overall loss as CP state impurity. The blue curve shows the geometric phase gained by the RH component as θ is varied. The expected 1:2 relation is achieved by a smooth linear curve. Any desired wavefront function can be constructed by rotating the nanopillars by $2\theta = \psi(x, y)$, where $\psi(x, y)$ is a wavefront function, e.g. Eqn. 2.18 for a focusing mirror. Fig. 4.6 b shows the same result for LH component. The yellow and green regions are the inverse of the RH plot, but the phase is unique. Unlike the RH component, LH component does not gain geometric phase and reflects as a plane wave. This agrees with the Eqn. 2.16, where the coefficient of $\hat{e}_{l/r}$ does not have the phase term. This should not be confused with the $-\phi$ phase gained by an incident LH field. The mirror diverges the incident LH field by $-\phi$ geometric phase, but LH component arising due to conversion

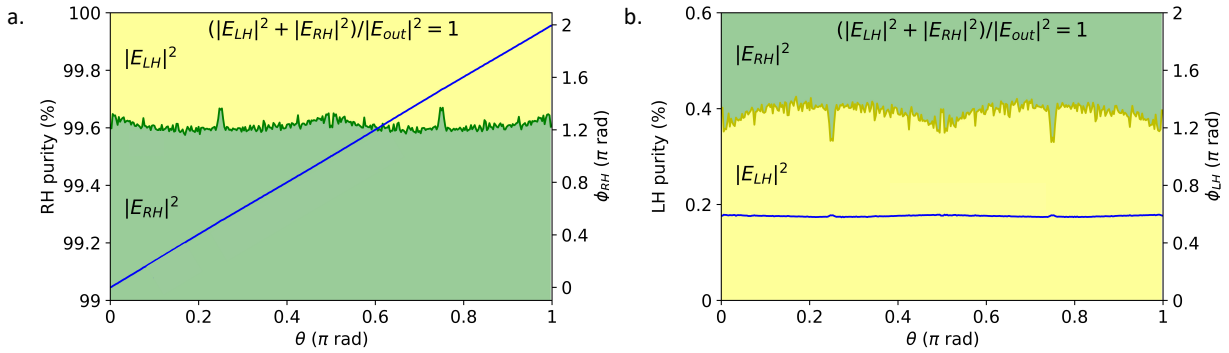

Figure 4.6: (a) Right handed (RH) purity at the output is shown by the green region, and left handed (LH) component is the yellow region over nanopillar angles. The normalization of the terms is given on the figure. The blue curve shows the geometric phase on RH component, ϕ_{RH}, which should have 1:2 ratio with θ. The units of θ is switched to radians to highlight the ratio. (b) Same plot as a, but here LH purity and phase of LH component is given.

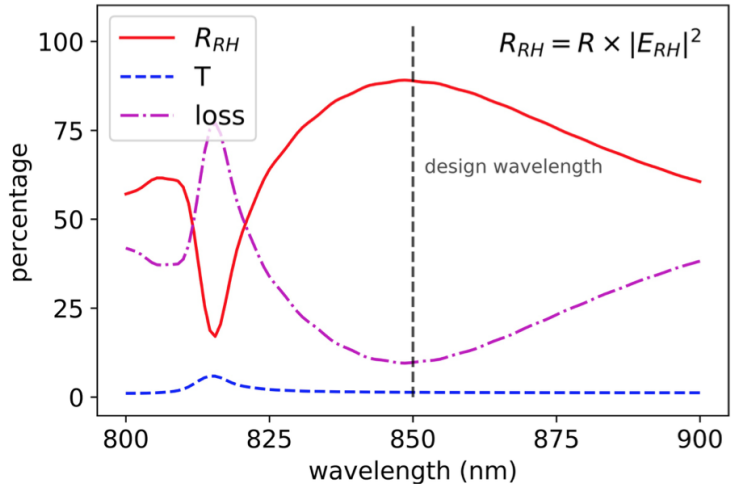

Figure 4.7: Wavelength dependence of the design is given. R_{RH} is the RH component of the reflected wave, T is transmission and loss includes both the material loss and any LH component that is reflected.

impurity does not experience geometric phase.

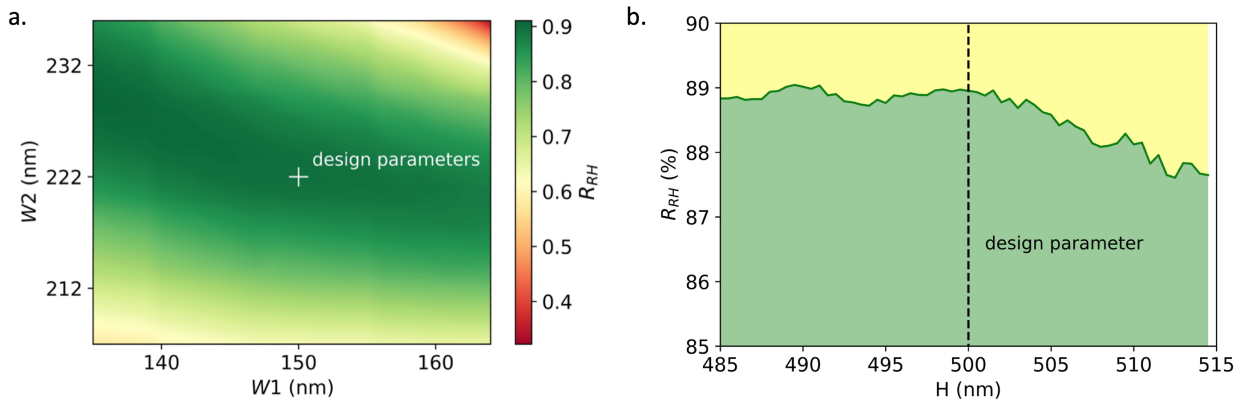

Figure 4.8: Sensitivity analysis of the design to nanopillar dimensions $W1, W2$ and H. (a) The 2D plot shows the R_{RH} quantity for different combinations of $W1$ and $W2$, a maximum of $15nm$ longer and shorter from the design parameters. (b) R_{RH} quantity is given for a range of nanopillar heights, a maximum of $15nm$ longer and shorter from the design parameter.

Overall, the two sources of loss can be combined to define a new quantity for the overall efficiency of the mirror, which is the reflected RH component relative to the incident wave:

$$R_{RH} = |E_{RH}|^2 \times R = 89.1\% \tag{4.5}$$

The wavelength dependence of the structure is given in Fig. 4.7. R_{RH} quantity (Eqn. 4.5) is used here to combine two plots, one for reflectivity and one for RH purity, and report only the combined efficiency. The efficiency, defined as R_{RH}, is maximum at $850nm$, and decreases as the wavelength deviates. The structure is not sensitive to small variations of wavelength, but it is not a good fit for more broadband applications.

The performance of the device strongly depends on the dimensions of nanopillars, especially $W1$ and $W2$. In Fig. 4.2, the gradient of phase difference over $W2$ is significant for higher refractive indices. The fabrication of the structure will have dimensional imperfections in the order of nanometers, which will effect the performance by deviating the phase difference condition from π rad. To quantify this, unit cell simulations are run with different combinations of $W1$ and $W2$ and the reflectivity and the electric field are recorded. The resulting R_{RH} (defined as Eqn. 4.5) is given in Fig. 4.8 a. Total reflectivity, R, is constant throughout the whole domain, so the main source of loss is the reduction in RH purity. A change in width will result with a different n_{eff} of the waveguide, so HWP condition is not fully satisfied. The change in R_{RH} as $W1$ deviates from $150nm$ is

much smaller than when $W2$ deviates from $222nm$. R_{RH} decreases by more than 1% per nm change of $W2$, while it decreases by less than 5% over a $W1$ change of $15nm$. Recall the n_{eff} plot in Fig. 2.9 for square-shaped waveguide with $n = 3$. Comparing this with the structure here, it is clear that $W1$ lies within the small tail where the plot is close to horizontal. Meanwhile $W2$ is at the region where the gradient of the plot is high. The sensitivity to height of nanopillars is given in Fig. 4.8 b. The decrease in R_{RH} is weaker, so the fabrication errors of height is more tolerable compared to $W1$ and $W2$.

4.3 Construction and Analysis of the Metasurface Mirror

Now we have a unit cell design which performs well under simulation conditions of the infinite crystal of the unit cell. However, the real mirror lacks the symmetry where all the nanopillars have the same angular orientation. Although breaking this symmetry should not cause any performance issues, it needs to be verified. Therefore, we will attempt to simulate the finite mirror structure and analyse whether the mirror maintains the CP state conservation and implements the focusing of light.

4.3.1 Unit Cell to Full-Sized Mirror

First, let's discuss the real-sized mirror, which will have $100\mu m$ long diameter. The nanopillars are rotated according to the spherical wavefront function given in Eqn. 2.18. The only unknown in the equation is the focal length. To determine the focal length, three things need to be considered if a cavity will be formed by the mirrors: minimizing the size of the cavity, numerical aperture and cavity stability. According to the cavity stability condition, a short cavity size corresponds to a short focal length. One commonly used stable cavity type is a confocal cavity, where $d = 2f$. However, shorter focal length results with a high numerical aperture for the mirror, which has an upper limit of $NA_{max} = 0.7$ due to the unit cell size $U = 500nm$, as discussed in Section 2.1. The NA limitation puts a lower limit on the focal length, $f_{min} = 65\mu m$. When the mirror is fabricated, the focal length can be chosen freely as long as the three conditions are satisfied. However, the simulation of a real-sized mirror is not possible, due to insufficient computational resources. We will attempt to simulate a smaller mirror structure to predict how the real product would perform.

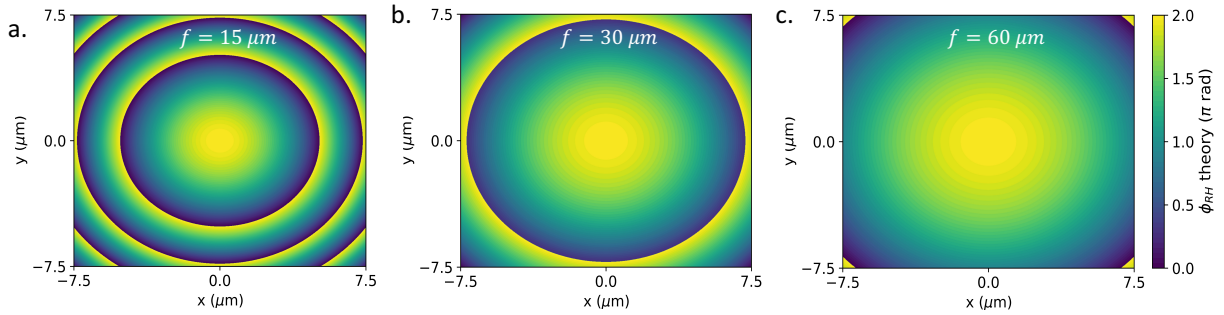

Figure 4.9: The phase profile of the RHCP light reflected off from a rectangular mirror of size $15\mu m$ with $f = 15\mu m$ (a), $f = 30\mu m$ (b), $f = 60\mu m$ (c). This follows the spherical wave profile given in Eqn. 2.18 and is equivalent to the geometric phase of RH component. All plots follow the colormap at the right.

The largest possible mirror structure the computer can simulate has a diameter of $15\mu m$. Now, a suitable focal length need to be chosen. The lower limit on the focal length for this mirror size due to the maximum numerical aperture value of 0.7 is $9.6\mu m$. Shorter focal lengths correspond to a larger gradient of phase profile, i.e. the phase of light changes more quickly per μm in the $x - y$ plane. The mirror can only exhibit good quality of focusing if the phase profile covers the whole $0 - 2\pi$ rad. range. This becomes an issue if the mirror size is small. In Fig. 4.9, the theoretical phase profile of the reflected light is plotted in the $x - y$ plane for focal lengths $15\mu m$, $30\mu m$ and $60\mu m$. This is equivalent to the geometric phase of RHCP light. The 2π phase coverage is fully satisfied for the case with $f = 15\mu m$ and $f = 30\mu m$. The phase gradient for $f = 15\mu m$ is large, which would correspond to neighbouring nanopillars having large rotation angle differences. A real-sized mirror with $f = 250\mu m$ has an average of 10.4 deg. angle difference between neighbouring nanopillars, while it is 12.9 deg. for the $30\mu m$ focal length and 24.1 deg. for the $15\mu m$ focal length. Therefore, in order to represent the real-sized mirror accurately, $30\mu m$ is chosen as the focal length for the demonstration, which corresponds to a NA of 0.25.

The simulation for the mirror is set up in Lumerical. The simulation region covers the mirror structure, but does not extend to the focal plane at $z = 30\mu m$ due to limited computational resources. Instead, the electric field data is collected at the output of the mirror and light is propagated analytically using Fourier optics. The electric field travels in free space by the phase evolution term $e^{ik_z z}$. For a plane wave, the only operation would be multiplying the electric field with the phase factor with a known k_z and z value. However, a focusing light consists of many plane waves propagating towards the focal point, where

each component have a different k vector. Each component need to be multiplied with its own unique phase factor.

First, the electric field in the physical space is Fourier transformed (2D) into the k-space to get the amplitude function $U(k_x, k_y)$. The amplitude function describes the amplitude of electric field that has the unique (k_x, k_y) values at z_0, where z_0 is the position at which the reflection data is recorded.

$$U(k_x, k_y)|_{z_0} = \frac{1}{\sqrt{2\pi}} \iint_{-7.5\mu}^{7.5\mu} E(x, y)|_{z_0} e^{i(k_x x + k_y y)} \, dx \, dy \tag{4.6}$$

After the amplitude function is calculated at z_0, the z component of the k vector ($\mathbf{k}$) is also need to be calculated.

$$k_z = \sqrt{|\mathbf{k}|^2 - k_x^2 - k_y^2} \tag{4.7}$$

$|\mathbf{k}|^2$ is equal to $2\pi/\lambda$ and is the same for every component of the amplitude function. Therefore, by evaluating k_z, the amplitude function at any desired z position can be found by

$$U(k_x, k_y)|_{z_1} = U(k_x, k_y)|_{z_0} e^{ik_z(z_1 - z_0)} \tag{4.8}$$

Now, the electric field is computed by applying inverse Fourier transform (2D) at the new z position z_1.

$$E(x, y)|_{z_1} = \frac{1}{\sqrt{2\pi}} \iint_{-7.5\mu}^{7.5\mu} U(k_x, k_y)|_{z_1} e^{-i(k_x x + k_y y)} \, dk_x \, dk_y \tag{4.9}$$

This technique is used to find the intensity of light away from the mirror for various z positions, including the focal plane z_f.

The Fourier transform is implemented using the fast Fourier transform (FFT) tool in python and the code is given in Appendix C.

4.3.2 Mirror Simulation Results and Focusing

Here, the simulation results for the $15\mu m$ sized mirror will be discussed. The set up is given in Fig. 4.10 a. The nanopillars on the structure are representative and does not reflect the

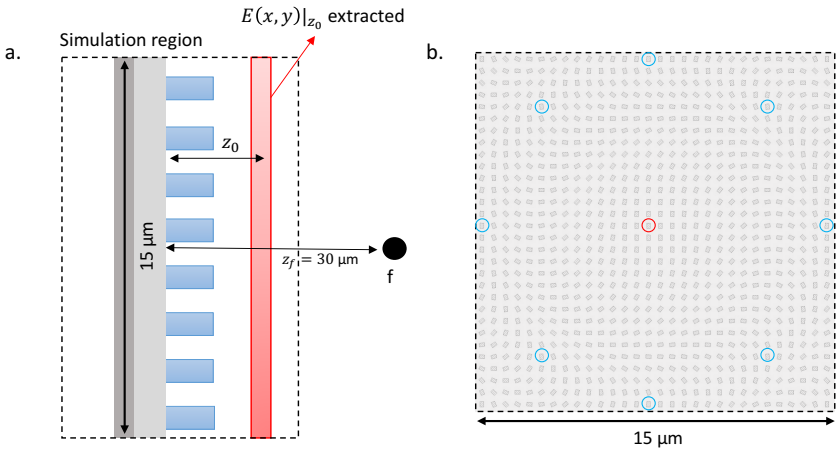

Figure 4.10: Simulation setup of full-mirror analysis. (a) The simulation region covers the structure, but does not extend towards the focal point. The field information is recorded at the red shaded region, then numerically propagated until the focal point. z_0 is $200nm$ from nanopillars. (b) The top view of the nanopillars in the mirror structure. The red and blue circles mark some nanopillars that are rotated by 0 and 180 deg. respectively.

real number or rotation. The nanopillars are rotated according to their position relative to the center of the structure in the $x-y$ plane, and the top view is given in Fig. 4.10 b. One of the central nanopillars with $\theta = 0$ deg. is marked by a red circle, and some of the nanopillars reaching $\theta = 180$ deg. are marked by blue circles to highlight the coverage of $0 - 2\pi$ rad. phase range.

First, the conservation of CP state and the geometric phase gained by the RH component are analysed. As shown in Fig. 4.10 a, the data is extracted from the red region, which is $200nm$ away from the top end of nanopillars. The distribution of R_{RH} in the $x-y$ plane at this position is given in Fig. 4.11. Majority of the region is dark green, which corresponds to a reflectivity of 89.5% and RH purity of $\sim$ 100%. However, around the edges, a significant decrease of R_{RH} occurs, which is a decrease of RH purity. Although the reason for this is unclear, the nanopillars located farther from the center have larger angular orientation difference between their neighbouring nanopillars, which gets as high as 25 deg. for this mirror. This might be a reason why the impurities occur at the edges. The other reason could be some boundary effect. This issue is recurrent with almost all of the finite mirror simulations, regardless of nanopillar rotations. This suggests that the effect could be either a simulation issue or an actual boundary effect which will also exist in the physical structure. This issue occurs in the space covered by the last or last

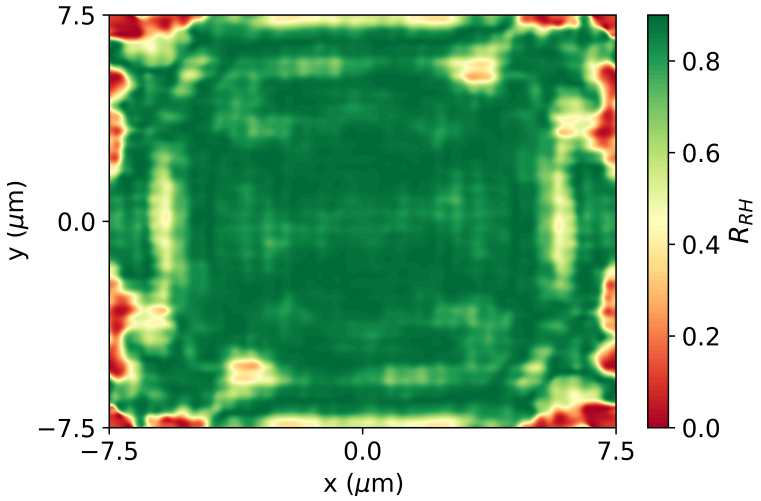

Figure 4.11: The distribution of R_{RH} after the mirror as RHCP plane wave is reflected from the mirror of $D = 15\mu m$. The reflectivity is consistent throughout the region, so low values correspond to low RH purity.

two nanopillars, which means that its effect should be less dominant for a larger diameter structure. This impurities cause the average R_{RH} within the $x - y$ plane to decrease to 81%, which means the average RH purity becomes 90.5%.

The geometric phase acquired by the RH component is given in Fig. 4.12. The upper half of the plot is the simulation results and the lower half is the theoretical phase distribution, equivalent to Fig. 4.9 b. The two distributions are added to the same plot for comparison purposes. Both of the plots are symmetric about the $x-$axis at $y = 0nm$, so no significant information is lost. Overall, the geometric phase agrees with the theoretical distribution except for the offset at the blue-to-red region. The offset is less significant than it appears because dark blue and dark red represent the same phase. The small mismatches in phase will reveal itself in the quality of focusing.

Now, the focusing is analysed. First let's see how the field propagates to and beyond the intended focal length of $30\mu m$. The field extracted at z_0 is propagated using Fourier optics. Fig. 4.13 shows the intensity of light in the $x - z$ plane at $y = 0nm$. The blue curve shows the intensity at the center of the 2D intensity graph with arbitrary units. The maximum of the blue curve is used to measure the actual focal length, which is found to be $28\mu m$, $2\mu m$ off from the design focal length.

The focusing quality is analysed at the measured focal length. First, let's discuss the

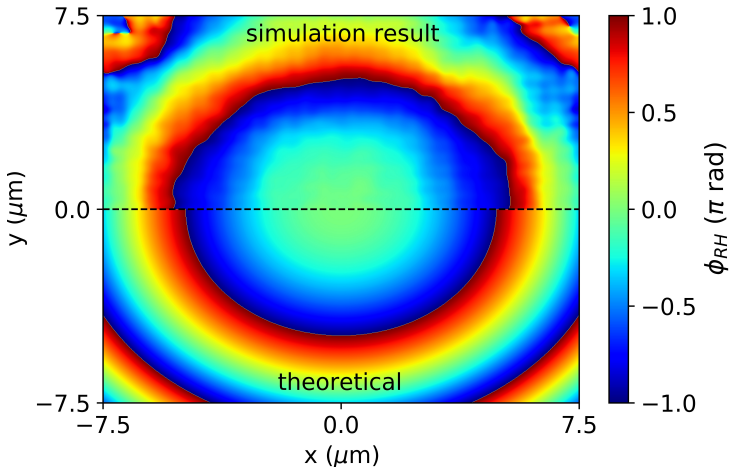

Figure 4.12: The geometric phase acquired by the RHCP light as RHCP plane wave is reflected from the mirror of $D = 15\mu m$. The upper half is the simulation results and the lower half is the expected distribution following the spherical wavefront Eqn. 2.18.

diffraction limit of our system. Consider a plane wave propagating through a 2D barrier with a single rectangular slit of size a and hitting a screen away from the slit. As light goes through the slit, it gets diffracted, where each position on the slit acts like a point source emitting light. The light leaving the slit causes interference patterns at the screen. This interference pattern describes the diffraction of light. The diffraction on the screen can be calculated using Fourier transform. The Fourier transform is applied to the aperture function, which is a function describing a rectangle, $A(x, y) = A_0$ if $|x|, |y| < a/2$ and $A(x) = 0$ if $|x|, |y| > a/2$. The integral is given as

$$E(k_x, k_y) = C(L) \int_{-\infty}^{\infty} A(x) e^{-ik_x x - ik_y y} dx dy \tag{4.10}$$

where $C(L)$ is an oscillatory term dependent on the distance to the screen only. The Fourier transform of a rectangle function is the sinc function, defined as $\operatorname{sinc} \alpha = \sin \alpha / \alpha$, so the Fourier transform gives

$$E(k_x, k_y) = C' \operatorname{sinc}(k_x a/2) \operatorname{sinc}(k_y a/2) = C' \operatorname{sinc}(ka \sin\theta/2) \operatorname{sinc}(ka \sin\phi/2) \tag{4.11}$$

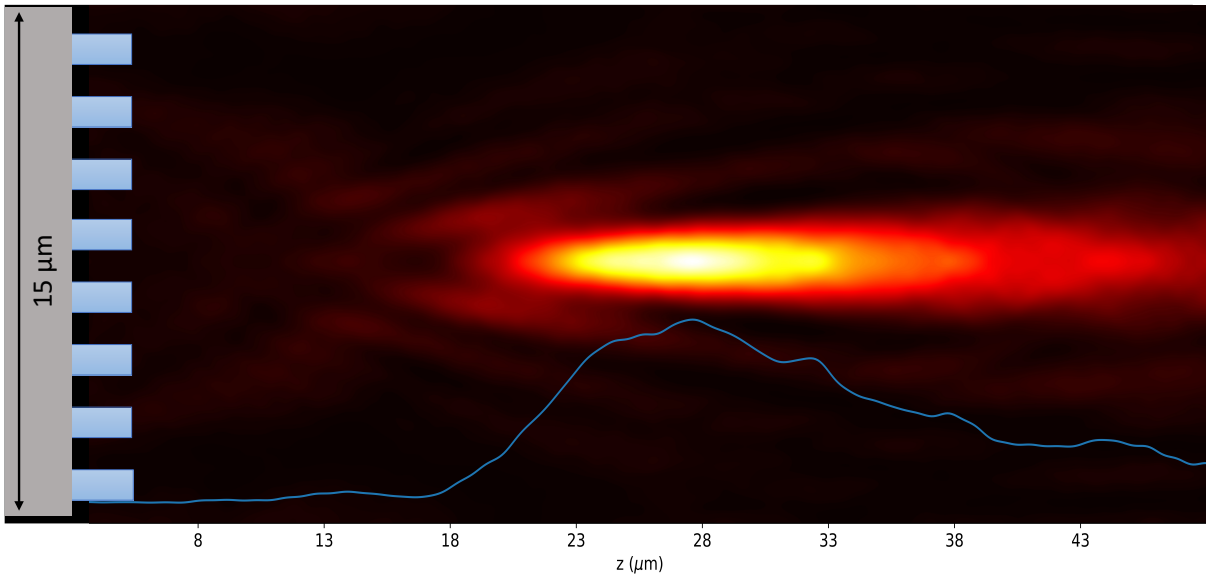

Figure 4.13: The intensity distribution in the $x-z$ plane as RHCP plane wave is reflected off the mirror with $D = 15\mu m$. The blue plot (of arbitrary unit) is the intensity at $x = 0$, which is used to find the observed focal length.

The two angles θ and ϕ are the angles between k and k_x (or k_y). The intensity distribution is simply a sinc^2 function, which is the intensity observed at the screen. The diffraction pattern looks like the orange curve in Fig. 4.14 b. For a concave lens of certain aperture size, the image created is limited by this diffraction pattern, i.e. light is fundamentally limited from focusing down to a single spot by diffraction. If light has aberrations, the width of the image will be greater than the width of the sinc function associated with the aperture size, so the light will be less focused.

In Fig. 4.14 a, the focal spot is given in the $x - y$ plane. The spot is most intense at the center and decreases in intensity away from the center, as expected. There are four secondary intensity peaks around the central dot, which is the result of diffraction for a rectangular aperture. The secondary peak would form a ring for a circular aperture. The intensity distribution in the x direction at $y = 0\mu m$ is given in Fig. 4.14 b. The blue curve is the result from the simulation and the orange curve is the diffraction limited distribution. The two curves are very similar in shape, and they are normalized such that the areas under two curves are the same.

If the focal spot is completely limited by diffraction, the peak of the intensity curve

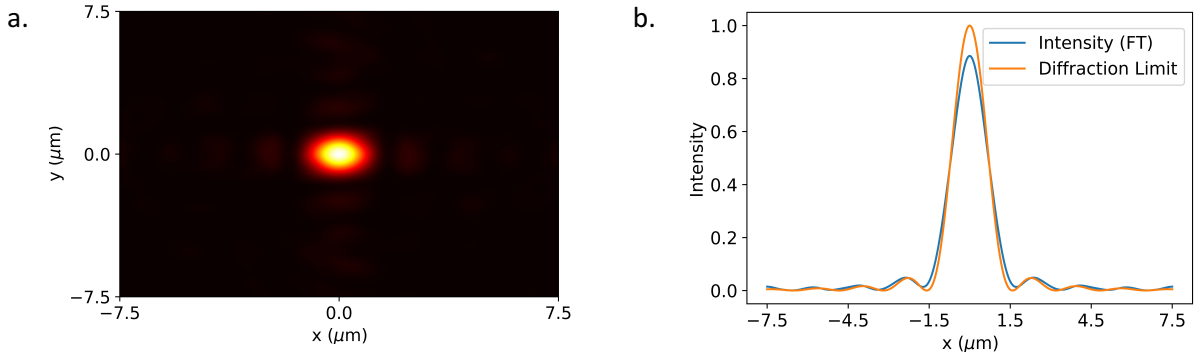

Figure 4.14: (a) The intensity distribution at the observed focal plane ($28\mu m$) of the finite mirror structure. (b) The intensity distribution at $y = 0$, normalized to the Airy function for rectangular aperture.

would match the peak of diffraction limited curve. A quantity called Strehl ratio is defined as the peak of the intensity distribution normalized to the diffraction limit, and here the ratio is 0.88. In general, Strehl ratio greater than 0.80 is considered good quality of focusing for imaging purposes. For our purposes, the quality of focusing is not of primary importance, but it shows that the mirror can be effectively applied to chiral imaging applications if needed.

The resulting FWHM (full width at half maximum) is also measured to be $1.38\mu m$, which quantifies the beam size at the center of a potential cavity built from these mirrors.

4.4 Fabry Pérot Cavity

In this Section, we consider a Fabry Pérot cavity of length $d = 2f = 56\mu m$ built by a pair of this mirror. The diagram of the cavity is given in Fig. 4.15. It supports only RHCP light, and should have high intensity at the center. Cavity supporting LHCP light can not be constructed by the same mirror, but another structure where the nanopillars are rotated by $-\theta$. The quality of the cavity can be represented by finesse and quality factor. For a Fabry Pérot cavity, the two parameters are given in Eqn. 2.27 and Eqn. 2.32. The final RH reflection value is 81% for the finite mirror. This reflectivity is used to calculate $\mathcal{F}$ and Q to get $\mathcal{F} = 15$ and $Q = 1964$.

The strength of light-matter interactions can be described by three parameters: decay

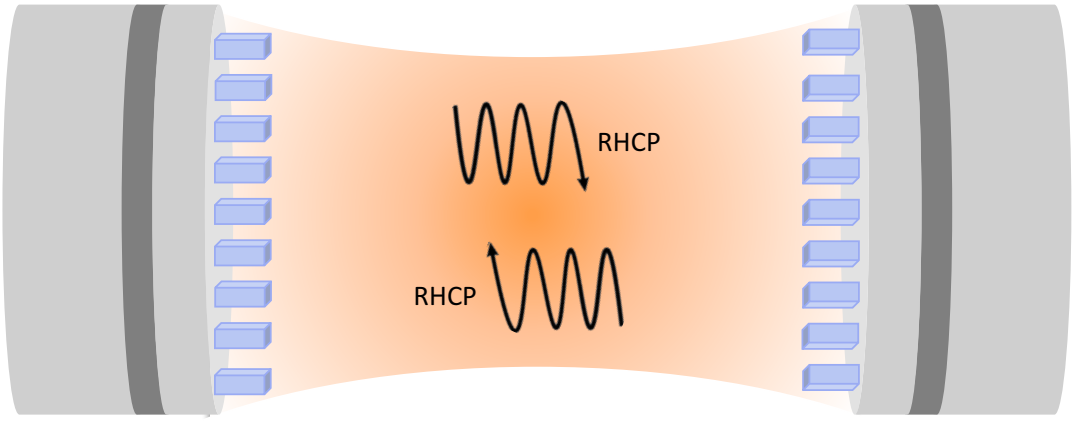

Figure 4.15: Diagram of a Fabry Pérot cavity supporting RHCP light, where the mirrors are chiral metasurface mirrors.

rate inside the cavity, κ, spontaneous emission of atoms, γ, and coupling strength between the cavity mode and the atoms, g. The decay rate is $\kappa = \omega/2Q$, so high Q factors contribute to stronger interactions. A Q factor of 2000 is considered to be high quality, but Q factors reaching the order 10^9 have been constructed [51]. The spontaneous emission rate of atoms are enhanced when a cavity is present, compared to free-space, by Purcell factor F_P [40].

$$F_P = \frac{3}{4\pi^2}\left(\frac{\lambda_0}{n}\right)^3 \frac{Q}{V} \tag{4.12}$$

Purcell factor is updated by Yoo *et al.* [54] for applications with chiral molecules as

$$F_C = \frac{1}{4\pi^2}\left(\frac{\lambda_0}{n}\right)^3 \frac{Q}{V_C} \tag{4.13}$$

where $V_C = U/\max[u_C]$. U is the total energy of the cavity, and $\max[u_C]$ is the maximum chiral energy density inside the cavity. Chiral energy density is related to the degree of chirality of light and helps enhance the Purcell factor.

The coupling strength is defined by the coupling constant as [48]

$$g = -\hat{\epsilon} \cdot \mathbf{d}_{ge}\sqrt{\frac{\omega}{2\epsilon_0 \hbar V}} \tag{4.14}$$

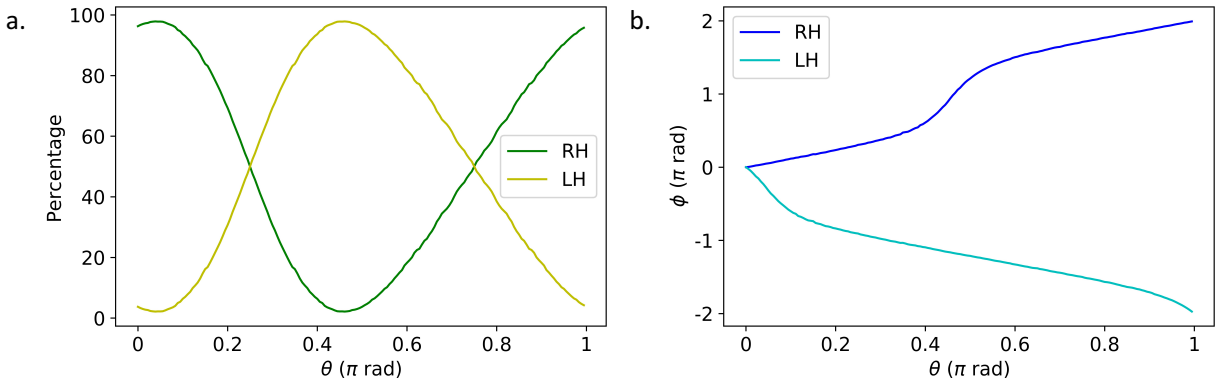

Figure 4.16: (a) Intensity of the two CP states and (b) geometric phase gained by two CP states in the cavity when a anti-diagonally polarized light is incident on the mirror from the back.

where $\hat{\epsilon}$ is the direction of electric field polarization on the atom and $\mathbf{d}_{ge}$ is the dipole matrix element for the atomic transition between ground and excited states and is $3.8 \times 10^{-29} Cm$ for cesium D2 transition [47]. It is inversely proportional to the mode volume, thus it can be enhanced by decreasing V.

The metasurface mirrors can be held in space by mounting them on optical fiber tips, which have similar diameter. The mounting procedure can be found in Appendix F. In this configuration, light can be directly coupled into the cavity from these optical fibers. However, the polarization of light need to be well defined. For some metasurface mirror structures, such as in [42], the incident light need to be circularly polarized. A fiber integrated QWP is also designed for such application, and the details are given in Chapter 5.

In the rest of this Chapter, coupling of light to the cavity mode will be discussed, then the cavity will be simulated for 120 roundtrips to find the mode distribution at the focal plane.

4.4.1 Coupling Into the Cavity

Coupling light from the back side of the mirror is not trivial because the nanopillars act as QWP's if light travels through them by a distance H, and their rotation will change the polarization state. The unit cell simulation is run, where anti-diagonally polarized light is

incident on the mirror from the metallic side, and the nanopillars are rotated. The electric field can be expressed as

$$\mathbf{E_i} = E_0 e^{i(kx-wt)} \left(\hat{\mathbf{i}} - \hat{\mathbf{j}}\right) \tag{4.15}$$

Fig. 4.16 a shows the CP state of the light over the rotation angle of nanopillars. Unlike the operation of the mirror, the CP state is not constant throughout this range. This configuration would allow 50% of incident light to be coupled into the cavity mode. In Fig. 4.16 b, the geometric phase acquired by the two CP states is given. RH component gains positive phase while LH component gains negative phase. For the RH component, the $1:2$ relation of θ and ϕ is roughly observed, but the curve is not linear. The wavefront of light inside the cavity will not be following a smooth spherical wavefront function, but it will be focused to some extend. This allows RH component to be captured by the cavity mode unlike the LH component, which will diverge.

Furthermore, the metallic layer allows 0.8% transmission. To increase the electric field inside the cavity, the mirror separation can be fine-tuned to a multiple of the wavelength of light. The electric field spectrum also have a Lorentzian shape, similar to the transmission curve in Fig. 2.11 b, so fine-tuning the cavity size will allow more than 0.8% coupling, which can reach as high as 100%.

4.4.2 Cavity Mode

Here, the shape of cavity mode is determined and mode volume is calculated. Multiple mirror reflections is simulated numerically in python. As FDTD simulation sizes are limited by computational resources, the operation of the mirror is imitated numerically. First, the output of the first mirror reflection (FDTD results) is propagated by Fourier optics, same technique as discussed in Section 4.3.1. Then, electric field is separated into phase and magnitude. Focusing is applied by adding the phase profile in Fig. 4.12 to the phase of the incident light on the second mirror. The rotation of nanopillars should always induce the same geometric phase with the relation $2\theta = \phi$. To find the mode shape that is supported by the cavity, light is simulated to travel 100 roundtrips inside the cavity. Then, the next 20 roundtrips were summed up to represent the mode shape. The two-dimensional intensity distribution found by this method is given in Fig. 4.17 at the focal plane. Intensity is normalized to the maximum value.

The modes supported by a cavity differ for the case with linear polarization and circular polarization. When linearly polarized light is trapped in a cavity, where the cavity size is

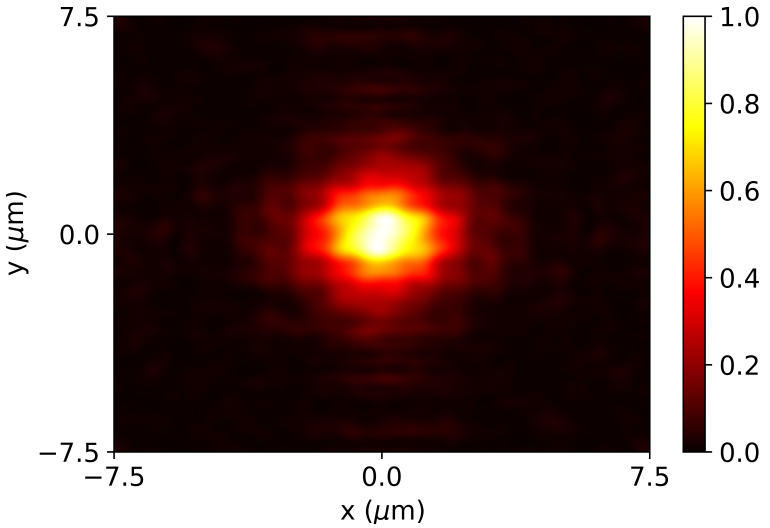

Figure 4.17: Total intensity after 120 roundtrips inside the cavity at the focal plane, at $y = 0\mu m$, normalized to the maximum value.

a multiple of wavelength, therefore the field is a standing wave with nodes and antinodes. Nodes are the points where the electric field is zero, and antinodes are the points where the electric field magnitude is maximum. This results with high and low intensity regions among the longitudinal direction of the cavity. However, when circularly polarized light is trapped in the cavity, the electric field vector is rotating. Therefore, the zero electric field regions at the nodes do not form.

To estimate the mode volume, this calculation is repeated for 10 different $x - y$ planes inside the cavity. Following Eqn. 2.33, the 10 two-dimensional distributions are integrated and divided by the maximum intensity. The resulting mode volume is $725\mu m^3 = 1180(\lambda/n)^3$, which is 17 times smaller than the physical cavity volume of $12600\mu m^3$. In general, a mode volume of order $100(\lambda/n)^3$ is common, but smaller mode volumes reaching $(\lambda/n)^3$ have also been constructed [51]. With this value of V, we can estimate the cavity parameters Purcell factor (Eqn. 4.12), coupling constant (Eqn. 4.14) and cavity decay rate ($\kappa = \omega/2Q$). Purcell factor is found to be $F_P = 0.0421$. Purcell factor describes the enhancement of spontaneous emission in the cavity mode, compared to free-space, and higher values correspond to stronger interactions. Purcell factor of 147 is calculated for an emitter in a micropost microcavity of $V = 2(\lambda/n)^3$ and $Q = 4800$ by Vučković *et al.* [52]. The coupling constant of our cavity for the cesium D2 transition is calculated as

$g = 2\pi \times 245MHz$. Buck and Kimble have constructed a cavity using microspheres that reach coupling constants of $g = 2\pi \times 750MHz$ with Q factors 0.8×10^7 [14] for cesium D2 transition. In another study, Hunger *et al.* have constructed a Fabry Pérot cavity with a finesse of 130000 and they estimate a coupling constant of $2\pi \times 200MHz$ for rubidium D2 transition [27]. Our value for the coupling constant is comparable to similar studies. Our decay rate is $\kappa = 2\pi \times 89GHz$. This is larger by three orders of magnitude than the decay rates found by Hunger *et al.* which is of order $\sim 2\pi \times 10MHz$ [27], and by Buck and Kimble as $2\pi \times 22MHz$ [14]. This is because our Q factor is at the lower end of the high quality factor cavity values, which are generally between $10^4 - 10^9$.

We have shown that our cavity have potential to enhance light-matter interactions significantly, but a larger Q factor would enhance the interactions significantly, and increasing the reflectivity of the mirrors is the main source for this improvement.

Chapter 5

Fiber Integrated Quarter-Waveplate

In Section 4.4, we proposed that metasurface mirrors can be mounted on fiber tips to be held in free space. This fiber is typically a polarization maintaining (PM) fiber, such that light being coupled into the cavity can have well defined polarization. Although our metasurface design does not require circularly polarized light for coupling, this gives us motivation for creating a fiber integrated QWP, where linearly polarization will be converted into circular polarization. The design will allow replacing bulky optics for converting linearly polarized light to circular polarization, as well as providing an effective method for coupling CP light to metasurfaces mounted on fiber tips, such as the chiral mirror design by Semnani *et al.* [42]. Creating quarter-waveplates out of fibers have been an interest to many studies, especially for optic-fiber current sensor applications. In a study by Temkina *et al.* [49], a birefringent PM fiber is used to implement the required phase lag between two linear polarization components. Unlike the method proposed in this Chapter, they do not uniquely define the length of the fiber, but change the phase difference imparted using a electro-optical modulator (EOM). Therefore, the phase difference is determined precisely by varying the voltage applied to EOM. Another study by Bertoncini *et al.* [10] have constructed a QWP by fabricating a Fresnel Rhomb, a tiny phase retarder, on a PM fiber. Our design includes splicing of two PM fibers and precise control of the length of one PM fiber. In this Chapter, we will explain the working principle of fiber integrated QWP, and introduce a broadband polarization tomography procedure for measuring the polarization state of light. Then, initial characterization of a fiber-QWP sample will be discussed.

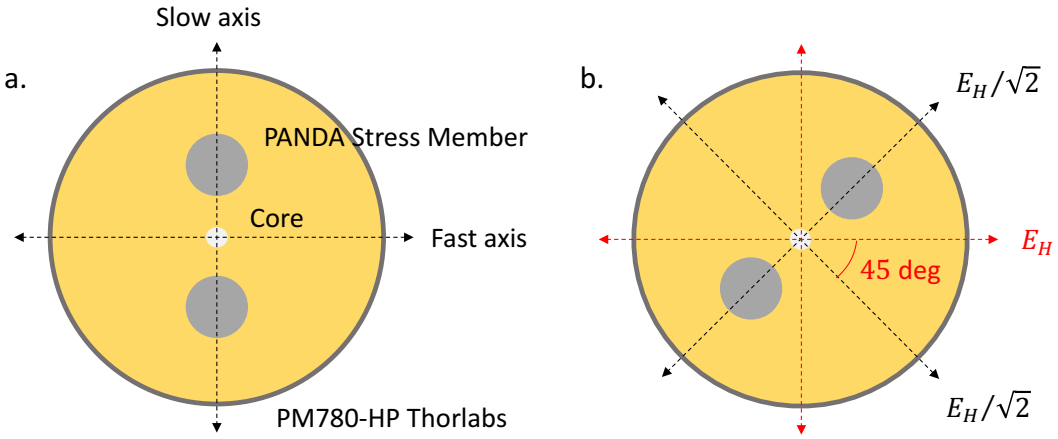

Figure 5.1: (a) Cross-section of a commercial polarization maintaining fiber from Thorlabs, PM780-HP. (b) Cross-section of another PM fiber, rotated 45 deg. clockwise from the first fiber and coupled to it. Black arrows show the fast and slow axes of the second fiber, and the red arrows show the fast and slow axes of the first fiber. H polarized light is coupled from first to second fiber, so the electric field is split into two.

5.1 Theory

The cross-section of a commercial PM fiber from Thorlabs (PM780-HP) [50] is given in Fig. 5.1 a. The two grey circles are called stress members, and they help preserving the linear polarization along both slow and fast axes. Therefore, if linearly polarized light, polarized along either of the axes, is coupled to the PM fiber, its polarization will be maintained. Two orthogonal components of linearly polarized light, aligned to fast and slow axes, will gain different phase according to the n_{eff} of each axis. According to the technical specification of the fiber, there is birefringence of amount $\Delta n = 3.5 \times 10^{-4}$. This means linearly polarized light aligned with the fast axis will evolve by a different n_{eff} than linearly polarized light aligned with the slow axis. The net phase difference, after propagating by length L, is given as

$$\Delta\Phi = \frac{2\pi}{\lambda}\Delta n L \tag{5.1}$$

Let's consider horizontally polarized light coupled to the PM fiber, along the fast axis. Another PM fiber is put in close proximity, but 45 deg. rotated, as shown in Fig. 5.1

b. The incident H polarized light will be split into two components along the fast and slow axes of the second fiber, which are 45 deg. misaligned with the axes of the initial fiber. Due to the birefringence between fast and slow axes, the two components will acquire different phase. If this phase difference is $\pi/2$ rad., then the structure will operate as a QWP. Similarly, a HWP can be implemented by setting the phase difference as π rad. The phase difference depends on the distance traveled in the second piece of fiber, i.e. L term in Eqn. 5.1 to satisfy $\Delta\Phi = \pi/2$. For $\lambda = 850nm$ and $\Delta n = 3.5 \times 10^{-4}$, L is found to be $607\mu m$ for a QWP. Therefore, if a PM fiber is spliced to a second PM fiber, which is 45 deg. misaligned to the first fiber and is exactly $607\mu m$ long, then the birefringence of the second fiber will impart $\pi/2$ rad. phase difference to the incident linearly polarized light, generating circularly polarized light. A clockwise rotation will result with RHCP light because x polarization is coupled to the slow axis, so it lags behind y polarization, while a counter-clockwise rotation will result with LHCP.

5.2 Experimental Setup

The two fibers need to be spliced at a specific rotational alignment, as well as the second fiber piece should have certain length. In order to achieve this, the two fibers are spliced together by Vytran GPX3600 Glass Processor, which allows precise control over the rotation angle of both fibers and achieves a $\sim 50\%$ success rate in splicing fibers. The second fiber is cleaved by Vytran LDC401 Fiber Cleaver, which allows precise control over the length, accurate to $\sim 10\mu m$. The operation procedures of the two devices can be found online.

A sample of spliced fiber can be found in Fig. 5.2, where the spliced region is visible. The length of the second fiber piece is measured to be $600\mu m$, which is $7\mu m$ off from the required length. This gives an error of 1.2% for the $\pi/2$ rad. phase difference.

Polarization state tomography is used to measure the polarization of the electric field leaving the PM fiber. The tomography setup is given in Fig. 5.3. The two waveplates and the linear polarizer shown by the dashed rectangle are the main components of tomography measurements. Prior to taking measurements, the setup need to be calibrated according to a known horizontal polarization. First, the linear polarizer is rotationally aligned such that it will define the horizontal polarization in the system, according to the horizontally polarized source. The polarizer is rotated until it provides maximum power for the known horizontally polarized source. Then, the waveplates are calibrated in order, such that their fast axis will be aligned with the horizontal polarization of the linear polarizer. This can be done by using a horizontally polarized source, inserting the waveplates and the

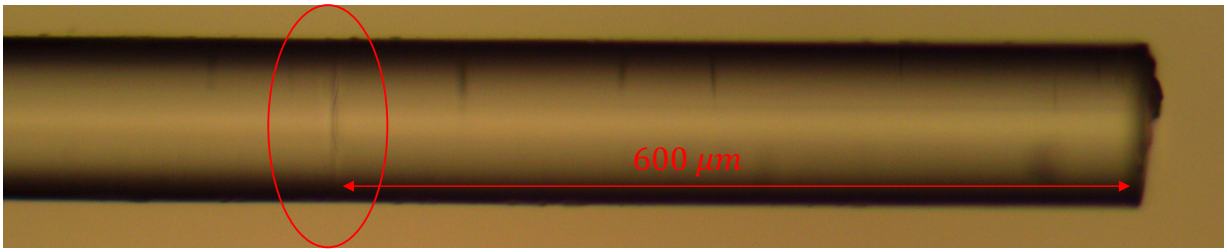

Figure 5.2: Microscope image of the spliced PM fiber. The spliced region is circled, and the length of the second piece is measured as $600\mu m$.

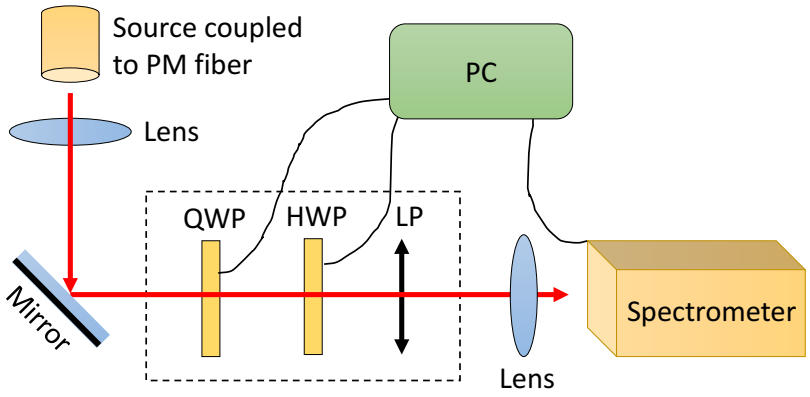

Figure 5.3: Experimental setup of polarization state tomography. QWP: Quarter-waveplate (motorized), HWP: Half-waveplate (motorized), LP: Linear polarizer.

linear polarizer, and maximizing the power at the output. The angle of the waveplates are controlled by a software called ELLO. The aligned position of the waveplates should be set to home position of waveplates on the software. This defines the zero angle rotation of waveplates. Then, to measure the amount of each polarization, the waveplates are rotated at certain angles, and the intensity recorded by the spectrometer gives the relative strength of each polarization state. The rotation angles allow each desired polarization state to be converted to horizontal polarization, which is the only component that gets transmitted at the linear polarizer, into the spectrometer. Table 5.1 lists the angles of the waveplates corresponding to measuring each polarization state.

To represent the polarization state, Stokes parameters need to be introduced. They are

Table 5.1: Tomography Measurement Waveplate Angles

Spectrometer Output	QWP angle (deg.)	HWP angle (deg.)
$\|E_H\|^2$	0	0
$\|E_V\|^2$	0	45
$\|E_D\|^2$	45	22.5
$\|E_A\|^2$	45	337.5(−22.5)
$\|E_R\|^2$	45	45
$\|E_L\|^2$	45	0

defined as [35]:

$$\begin{aligned} S0 &= |E_H|^2 + |E_V|^2 \\ S1 &= |E_H|^2 - |E_V|^2 \\ S2 &= |E_D|^2 - |E_A|^2 \\ S3 &= |E_L|^2 - |E_R|^2 \end{aligned} \tag{5.2}$$

The Stokes parameters can easily be computed by tomography, as all six polarization states are measured by tomography. Stokes parameters allow representing the complete polarization by three parameters, so one can determine the position of the polarization vector on the Poincaré sphere, as represented by the green vector on Fig. 5.4. $S0$ does not have an interpretation for the Poincaré sphere, while $S1$, $S2$ and $S3$ represent each axis. $S0$ is the total intensity and is used to compute the purity of polarization of light. Purity of polarization, p is defined as

$$p = \frac{\sqrt{S1^2 + S2^2 + S3^2}}{S0} \tag{5.3}$$

For completely polarized light, $p = 1$ and the vector is on the Poincaré sphere, and for partially polarized light, $0 < p < 1$ and the vector is inside the Poincaré sphere.

The measurement process is automated using Elliptec's motorized piezoelectric rotation system, where the rotation of waveplates are controlled in Matlab. The spectrometer is also integrated to Matlab, so that the full measurement can be done by running a single

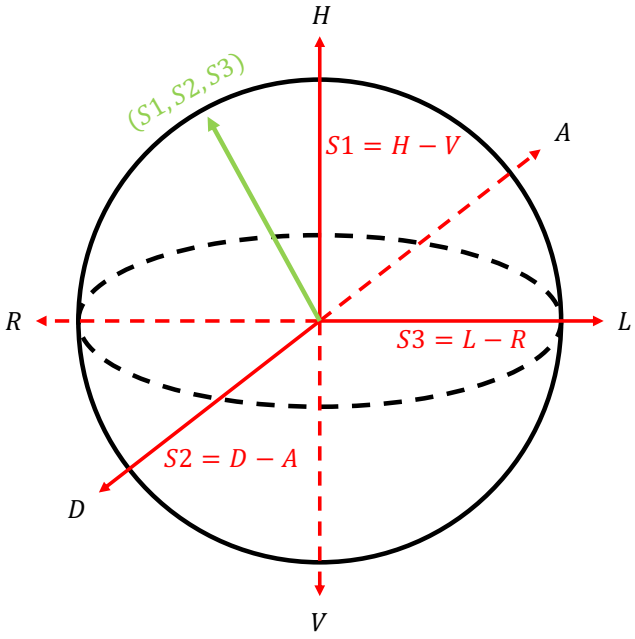

Figure 5.4: Poincaré sphere representing the polarization states of light. The Stokes parameters define each axis and the polarization of light can be represented by a vector on the sphere, as represented by the green vector.

script. The codes required for tomography are developed by my colleague Yujia Yuan, and can be found in Github [30].

5.3 Polarization Tomography Results

First, polarization tomography is tested by a source with known polarization. A linear polarizer and a HWP is placed before the tomography setup and they are calibrated according to the defined horizontal polarization. Then, the tomography is run for different HWP angles. In order to get accurate results, the spectrometer signal (number of counts) is kept at $\sim 4 \times 10^4$ using an attenuator. Noise in the spectrometer is $\sim$ 1500 counts, so low levels of input signal results with lower purities. Spectrometer signal saturates as 7×10^4, and signal close to this value also results with wrong purity results.

The tomography results for different HWP angles are given in Fig. 5.5, with 22.5 deg. increments. In a, purity of 0.94 is observed, and $S1$ is the major Stokes parameter,

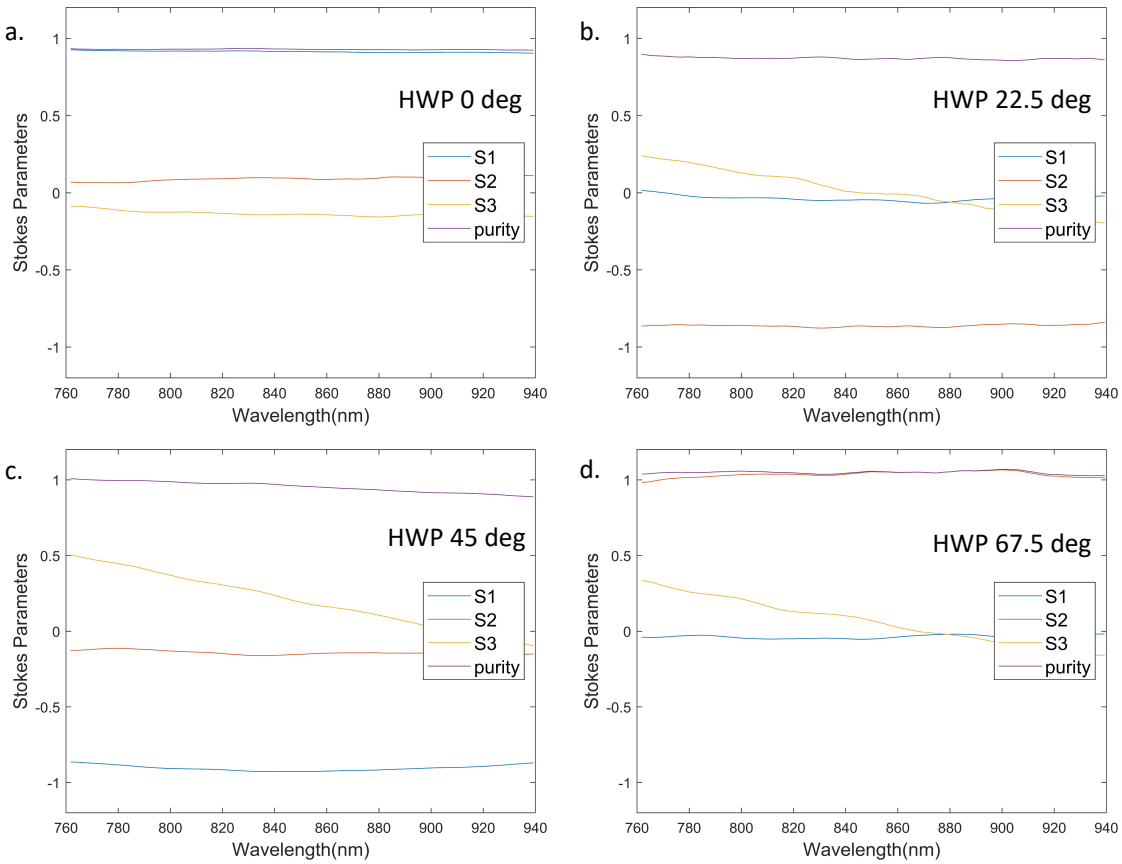

Figure 5.5: Testing the polarization tomography setup using a source with known polarization, where the polarization of the source is changed by rotating a HWP. Tomography results are given for HWP angles 0 deg. (a), 22.5 deg. (b), 45 deg. (c) and 67.5 deg. (d).

which means light is horizontally polarized, as expected. As the HWP is rotated, the Stokes parameters show that light is converted to anti-diagonal polarization, then vertical polarization, and finally diagonal polarization. This is the expected pattern for the given HWP angles. Also, purity levels are very close to unity, except for the last result where purity is 1.05, slightly above 1.

Then, the polarization of a $1m$ long PM fiber is measured to determine the output polarization without the QWP piece. Light is coupled to the PM fiber directly from a horizontally polarized source, and the output of the fiber is sent through the tomography setup. The results of the tomography is given in Fig. 5.6. Each Stokes parameter are

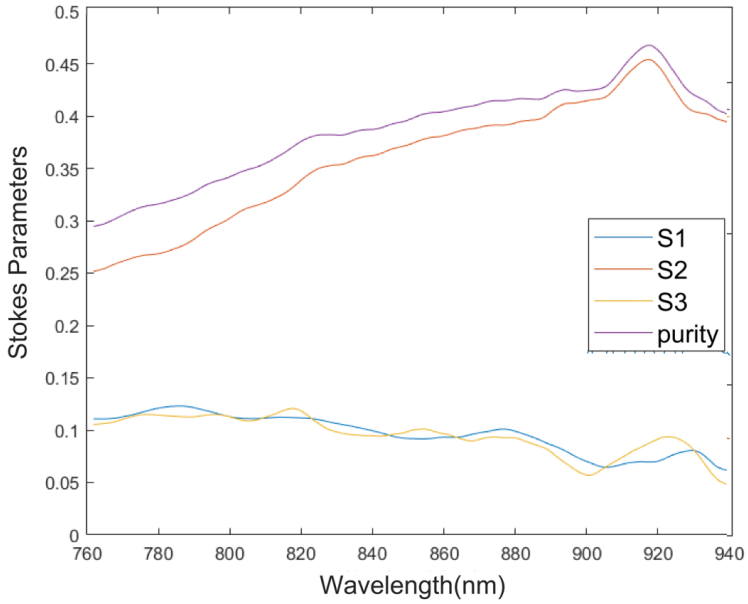

Figure 5.6: Stokes parameters and purity of a PM fiber sample over a range of wavelengths within the operation bandwidth of the fiber, recorded by the spectrometer.

plotted, normalized to $S0$ (total incident power), and the purity is also included. The strongest Stokes parameter is $S2$ with a mean magnitude of 0.35, and a maximum magnitude of 0.44, while the magnitudes of $S1$ and $S3$ are below 0.1. This means light leaving the PM fiber is diagonally polarized relative to the linear polarizer, which was set to horizontal polarization.

This $1m$ PM fiber is spliced with a second piece, which is the fiber sample in Fig. 5.2. The polarization of this sample is measured by the same procedure. The results of the tomography is given in Fig. 5.7. Here, $S3$ is the strongest Stokes parameter, reaching a magnitude of 0.4, while $S1$ and $S2$ are close to 0.0. This means the output of the fiber sample is circularly polarized.

In both cases, purity levels are close to 0.4, which implies that 60% of light is unpolarized. However, we predict that the propagated mode in the PM fiber should be polarized by definition of the fiber. During tomography measurements, we have observed irregular purities because of the measurement of $S0$. To check this, we propose repeating the experiment with monochromatic light coupled to the fiber samples, manually rotating the waveplates using the software ELLO, and recording the output power with a power meter instead of a spectrometer. This allows more control on the experiment and overcomes any

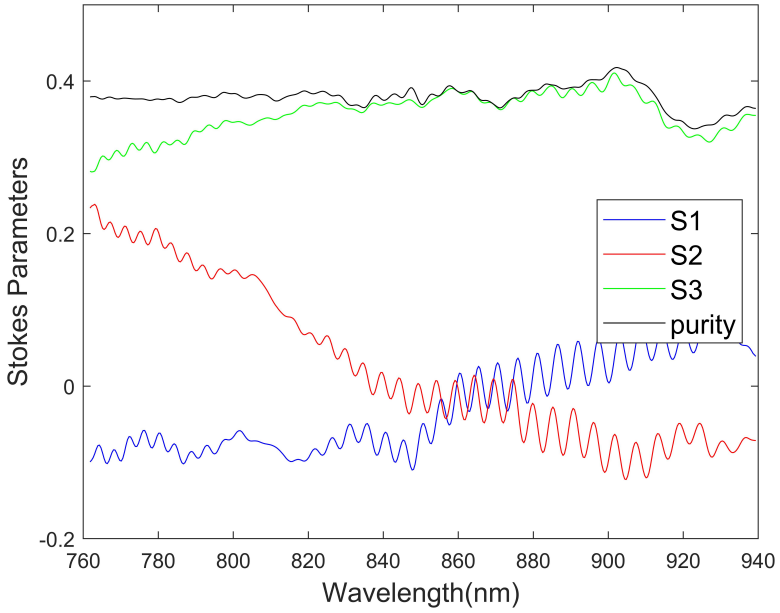

Figure 5.7: Stokes parameters and purity of the fiber-integrated QWP sample over a range of wavelengths within the operation bandwidth of the fiber, recorded by the spectrometer.

issues that might have caused by the spectrometer such as noise and saturation of signal. Although the purity results are unclear, the strongest Stokes parameter should be accurate. This concludes that the fiber-integrated QWP is working in principle, as it outputs circularly polarized light, but more work is needed to determine the quality of polarization.

Chapter 6

Conclusion

In this thesis, we have proposed a dielectric metasurface mirror design for the enhancement of light-matter interactions. First, we introduced the geometric phase and showed that dielectric waveguides have birefringent effects when they have small sizes and asymmetrical shapes. We also introduced the Fabry Pérot cavity and its properties. Then, the procedure for designing the unit cell structure was introduced, and an early version of the design was analysed. It had performance issues at certain nanopillar angles, which was solved by introducing a spacer, using a higher refractive index material and increasing the distance between neighbouring nanopillars. These changes were applied to get the final version of the design.

The unit cell structure provides 99.6% conservation of circular polarization state by intensity and induces a well-defined geometric phase according to the rotation of nanopillars, which proves the theoretical operation of our metasurface. The design has 9.5% material loss, 5.5% of which is through the dielectric layer and 4% of which is due to the metallic layer. In literature, a-Si is reported to be lossless [3], so improved fabrication techniques is promising to decrease the extinction ratio of a-Si. Alternatively, the material could be switched to TiO2, which is used in metasurfaces [23] and is lossless, but has a lower refractive index. The metallic layer can be replaced with a dielectric mirror, but it would be more challenging to fabricate and would decrease the compactness of the overall structure. Instead, the optical path length of the spacer layer was changed to $\lambda/2$, so on the surface of the metal, destructive interference could overcome the plasmonic excitations. Simulations show that this change reduces loss to 2% from 4%, but does not eliminate it completely. It has not been incorporated to the design, but it is a potential update.

Next, the unit cell design is extended to the full-sized mirror (diameter $15\mu m$), where

each nanopillar is rotated at different angles. Conservation of the circular polarization state decreased to 90.5%, but the imperfections are due to the edge or boundary effects, which should be less significant for a larger mirror of diameter $\sim 100\mu m$. Focusing quality of the mirror is analysed. The mirror implements good quality of focusing with Strehl ratio of 0.88, which means the distribution of light at the focal plane is close to the diffraction limit of a rectangular aperture. Overall, the mirror is 81% efficient for reflecting the relevant circular polarization state.

Our main motivation for this mirror is building a free-space Fabry Pérot cavity for light-matter interactions. Some qualities of a potential cavity was analysed. Using the final reflectivity of one circular polarization state, the finesse and Q factor of the cavity is calculated as $\mathcal{F} = 15$ and $Q = 1964$. We discussed that high Q factors and low mode volumes enhance light-matter interactions significantly by decreasing κ and/or increasing F_C and g , and our chiral metasurface mirror can achieve this. We also showed that if an anti-diagonal light is incident from the back of the mirror to couple light into the cavity, 50% will be lost to LH mode, but the remaining RH mode will be focused with some imperfections in the phase profile. Finally, we simulated 120 roundtrips in the cavity to find the mode shape at the focal plane. We have calculated the cavity parameters. The coupling constant is found to be comparable with similar studies, but reflectivity of the mirrors need to be enhanced to increase Purcell factor and to decrease cavity decay. Further analysis to confirm the numerical aperture, and to quantify the response of the mirror when the incident light is not perpendicular to the structure is important for this mirror design. In real-life applications, cavity mode diverges strongly from the focal point to the mirror, and the mirror should be able to perform well under such case.

The next step for this project is the fabrication and characterization the mirror to confirm simulation results.

Last, we introduced a fiber integrated quarter-waveplate to create circularly polarized light without the need of bulky optics for metasurface applications. The procedure for measuring the tomography of polarization state, which will also be useful for the characterization of the mirror, is introduced. A fiber sample has been constructed, and polarization tomography is applied to the sample. Preliminary results show that the fiber-integrated QWP is successful for converting a linearly polarized light to circular polarization. More work is needed to determine the purity of polarization (i.e. how much light is polarized) after the sample.

References

[1] I. A. Calafell, J. D. Cox, M. Radonjić, J. R. M. Saavedra, F. J. García de Abajo, L. A. Rozema, and P. Walther. Quantum computing with graphene plasmons. *npj Quantum Information*, 5(1):37, 2019.

[2] F. Aieta, P. Genevet, M. Kats, and F. Capasso. Aberrations of flat lenses and aplanatic metasurfaces. *Opt. Express*, 21(25):31530–31539, Dec 2013.

[3] A. Arbabi, E. Arbabi, Y. Horie, S. M. Kamali, and A. Faraon. Planar metasurface retroreflector. *Nature Photonics*, 11(7):415–420, 2017.

[4] A. Arbabi, Y. Horie, M. Bagheri, and A. Faraon. Dielectric metasurfaces for complete control of phase and polarization with subwavelength spatial resolution and high transmission. *Nature Nanotechnology*, 10(11):937–943, 2015.

[5] E. Arbabi, A. Arbabi, S. M. Kamali, Y. Horie, M. Faraji-Dana, and A. Faraon. Mems-tunable dielectric metasurface lens. *Nature Communications*, 9(1):812, 2018.

[6] M. Bajcsy, S. Hofferberth, T. Peyronel, V. Balic, Q. Liang, A. S. Zibrov, V. Vuletic, and M. D. Lukin. Laser-cooled atoms inside a hollow-core photonic-crystal fiber. *Phys. Rev. A*, 83:063830, Jun 2011.

[7] Y. Bao, Q. Lin, R. Su, Z.-K. Zhou, J. Song, J. Li, and X.-H. Wang. On-demand spin-state manipulation of single-photon emission from quantum dot integrated with metasurface. *Science Advances*, 6(31), 2020.

[8] A. Basiri, X. Chen, J. Bai, P. Amrollahi, J. Carpenter, Z. Holman, C. Wang, and Y. Yao. Nature-inspired chiral metasurfaces for circular polarization detection and full-stokes polarimetric measurements. *Light: Science & Applications*, 8(1):78, 2019.

[9] M.V. Berry. The adiabatic phase and pancharatnam's phase for polarized light. *Journal of Modern Optics*, 34(11):1401–1407, 1987.

[10] A. Bertoncini and C. Liberale. Polarization micro-optics: Circular polarization from a fresnel rhomb 3d printed on an optical fiber. *IEEE Photonics Technology Letters*, 30(21):1882–1885, 2018.

[11] M. G. Blaber, M. D. Arnold, and M. J. Ford. Search for the ideal plasmonic nanoshell: The effects of surface scattering and alternatives to gold and silver. *The Journal of Physical Chemistry C*, 113(8):3041–3045, 2009.

[12] W. Bogaerts, P. De Heyn, T. Van Vaerenbergh, K. De Vos, S. Kumar Selvaraja, T. Claes, P. Dumon, P. Bienstman, D. Van Thourhout, and R. Baets. Silicon microring resonators. *Laser & Photonics Reviews*, 6(1):47–73, 2012.

[13] Z. Bomzon, G. Biener, V. Kleiner, and E. Hasman. Space-variant pancharatnam–berry phase optical elements with computer-generated subwavelength gratings. *Opt. Lett.*, 27(13):1141–1143, Jul 2002.

[14] J. R. Buck and H. J. Kimble. Optimal sizes of dielectric microspheres for cavity qed with strong coupling. *Phys. Rev. A*, 67:033806, Mar 2003.

[15] E. Collett. *Field Guide to Polarization*. SPIE Press, Bellingham, WA, 2005.

[16] Z.-B. Fan, Z.-K. Shao, M.-Y. Xie, X.-N. Pang, W.-S. Ruan, F.-L. Zhao, Y.-J. Chen, S.-Y. Yu, and J.-W. Dong. Silicon nitride metalenses for close-to-one numerical aperture and wide-angle visible imaging. *Phys. Rev. Applied*, 10:014005, Jul 2018.

[17] J. Flannery. *Optical Resonators Integrated into a Hollow Core Photonic Crystal Fiber for Enhanced Light-Matter Interactions*. PhD thesis, University of Waterloo, 2019.

[18] J. Flannery, R. Al Maruf, T. Yoon, and M. Bajcsy. Fabry-pérot cavity formed with dielectric metasurfaces in a hollow-core fiber. *ACS Photonics*, 5(2):337–341, 02 2018.

[19] P. Genevet, N. Yu, F. Aieta, J. Lin, M. A. Kats, R. Blanchard, M. O. Scully, Z. Gaburro, and F. Capasso. Ultra-thin plasmonic optical vortex plate based on phase discontinuities. *Applied Physics Letters*, 100(1):013101, 2012.

[20] C. Gonzalez-Ballestero, A. Gonzalez-Tudela, F. J. Garcia-Vidal, and E. Moreno. Chiral route to spontaneous entanglement generation. *Phys. Rev. B*, 92:155304, Oct 2015.

[21] N. J. Greenfield. Using circular dichroism spectra to estimate protein secondary structure. *Nature Protocols*, 1(6):2876–2890, 2006.

[22] D. J. Griffiths. *Introduction to electrodynamics; 4th ed.* Pearson, Boston, MA, 2013. Re-published by Cambridge University Press in 2017.

[23] B. Groever, N. A. Rubin, J. P. B. Mueller, R. C. Devlin, and F. Capasso. High-efficiency chiral meta-lens. *Scientific Reports*, 8(1):7240, 2018.

[24] C.M. Haapamaki, J. Flannery, G. Bappi, R. Al Maruf, S.V. Bhaskara, O. Alshehri, T. Yoon, and M. Bajcsy. Mesoscale cavities in hollow-core waveguides for quantum optics with atomic ensembles. *Nanophotonics*, 5(3):392–408, 2016.

[25] E. Hecht. *Optics; 4th ed.* Addison-Wesley, San Francisco, CA, 2002.

[26] H.-H. Hsiao, C. H. Chu, and D. P. Tsai. Fundamentals and applications of metasurfaces. *Small Methods*, 1(4):1600064, 2017.

[27] D. Hunger, T. Steinmetz, Y. Colombe, C. Deutsch, T. W. Hänsch, and J. Reichel. A fiber fabry–perot cavity with high finesse. *New Journal of Physics*, 12(6):065038, jun 2010.

[28] L. Kang, S. P. Rodrigues, M. Taghinejad, S. Lan, K.-T. Lee, Y. Liu, D. H. Werner, A. Urbas, and W. Cai. Preserving spin states upon reflection: Linear and nonlinear responses of a chiral meta-mirror. *Nano Letters*, 17(11):7102–7109, 2017. PMID: 29072915.

[29] M. Khorasaninejad, W. T. Chen, R. C. Devlin, J. Oh, A. Y. Zhu, and F. Capasso. Metalenses at visible wavelengths: Diffraction-limited focusing and subwavelength resolution imaging. *Science*, 352(6290):1190–1194, 2016.

[30] S. Kuru. Chiral mirror. https://github.com/semakuuru/ChiralMirror, 2021.

[31] W. Li, Z. J. Coppens, L. V. Besteiro, W. Wang, A. O. Govorov, and J. Valentine. Circularly polarized light detection with hot electrons in chiral plasmonic metamaterials. *Nature Communications*, 6(1):8379, 2015.

[32] P. Lodahl, S. Mahmoodian, S. Stobbe, A. Rauschenbeutel, P. Schneeweiss, J. Volz, H. Pichler, and P. Zoller. Chiral quantum optics. *Nature*, 541(7638):473–480, 2017.

[33] L. Marrucci, C. Manzo, and D. Paparo. Pancharatnam-berry phase optical elements for wave front shaping in the visible domain: Switchable helical mode generation. *Applied Physics Letters*, 88(22):221102, 2006.

[34] J. Martínez-Llinàs, C. Henry, D. Andrén, R. Verre, M. Käll, and P. Tassin. A gaussian reflective metasurface for advanced wavefront manipulation. *Opt. Express*, 27(15):21069–21082, Jul 2019.

[35] A. Niggebaum. Quantum state tomography of the 6 qubit photonic symmetric dicke state. Master's thesis, Ludwig Maximilian University of Munich, 2011.

[36] R. Oulton. Lecture notes in solid state physics, January 2018.

[37] S. Pancharatnam. Generalized theory of interference, and its applications. *Proceedings of the Indian Academy of Sciences - Section A*, 44(5):247–262, 1956.

[38] J. Petersen, J. Volz, and A. Rauschenbeutel. Chiral nanophotonic waveguide interface based on spin-orbit interaction of light. *Science*, 346(6205):67–71, 2014.

[39] D. T. Pierce and W. E. Spicer. Electronic structure of amorphous si from photoemission and optical studies. *Phys. Rev. B*, 5:3017–3029, Apr 1972.

[40] E. M. Purcell, H. C. Torrey, and R. V. Pound. Resonance absorption by nuclear magnetic moments in a solid. *Phys. Rev.*, 69:37–38, Jan 1946.

[41] A. Sargsyan, E. Klinger, C. Leroy, T. A. Vartanyan, and D. Sarkisyan. Circular dichroism of atomic transitions of the rb d1 line in magnetic fields. *Optics and Spectroscopy*, 125(6):833–838, 2018.

[42] B. Semnani, J. Flannery, R. Al Maruf, and M. Bajcsy. Spin-preserving chiral photonic crystal mirror. *Light: Science & Applications*, 9(1):23, 2020.

[43] B. Semnani, A. H. Majedi, and S. Safavi-Naeini. Nonlinear quantum optical properties of graphene. *Journal of Optics*, 18(3):035402, Feb 2016.

[44] V. Sharma, M. Crne, J. O. Park, and M. Srinivasarao. Structural origin of circularly polarized iridescence in jeweled beetles. *Science*, 325(5939):449–451, 2009.

[45] I. Söllner, S. Mahmoodian, S. L. Hansen, L. Midolo, A. Javadi, G. Kiršanskė, T. Pregnolato, H. El-Ella, E. H. Lee, J. D. Song, S. Stobbe, and P. Lodahl. Deterministic photon–emitter coupling in chiral photonic circuits. *Nature Nanotechnology*, 10(9):775–778, 2015.

[46] L. Sortino, P. G. Zotev, S. Mignuzzi, J. Cambiasso, D. Schmidt, A. Genco, M. Aßmann, M. Bayer, S. A. Maier, R. Sapienza, and A. I. Tartakovskii. Enhanced light-matter interaction in an atomically thin semiconductor coupled with dielectric nano-antennas. *Nature Communications*, 10(1):5119, 2019.

[47] D. A. Steck. *Cesium D Line Data*. available online at http://steck.us/alkalidata (revision 2.2.1, 21 November 2019).

[48] D. A. Steck. *Quantum and Atom Optics*. Eugene, OR, 2019. available online at http://steck.us/teaching (revision 0.12.6, 23 April 2019).

[49] V. Temkina, A. Medvedev, A. Mayzel, A. Mokeev, and A. Kirpichenko. Manufacturing method and stability research of the fiber quarter-wave plate for fiber optic current sensor. In *2019 IEEE International Conference on Electrical Engineering and Photonics (EExPolytech)*, pages 278–281, 2019.

[50] Thorlabs. *Polarization Maintaining Fiber (PM780-HP)*, 12 2005.

[51] K. J. Vahala. Optical microcavities. *Nature*, 424(6950):839–846, 2003.

[52] J. Vučković, M. Pelton, A. Scherer, and Y. Yamamoto. Optimization of three-dimensional micropost microcavities for cavity quantum electrodynamics. *Phys. Rev. A*, 66:023808, Aug 2002.

[53] S. Yang, Z. Liu, S. Hu, A.-Z. Jin, H. Yang, S. Zhang, J. Li, and C. Gu. Spin-selective transmission in chiral folded metasurfaces. *Nano Letters*, 19(6):3432–3439, 06 2019.

[54] S. Yoo and Q-H. Park. Chiral light-matter interaction in optical resonators. *Phys. Rev. Lett.*, 114:203003, May 2015.

[55] N. Yu, F. Aieta, P. Genevet, M. A. Kats, Z. Gaburro, and F. Capasso. A broadband, background-free quarter-wave plate based on plasmonic metasurfaces. *Nano Letters*, 12(12):6328–6333, 12 2012.

[56] N. Yu, P. Genevet, M. A. Kats, F. Aieta, J.-P. Tetienne, F. Capasso, and Z. Gaburro. Light propagation with phase discontinuities: Generalized laws of reflection and refraction. *Science*, 334(6054):333–337, 2011.

[57] S.-P. Yu, J. D. Hood, J. A. Muniz, M. J. Martin, R. Norte, C.-L. Hung, S. M. Meenehan, J. D. Cohen, O. Painter, and H. J. Kimble. Nanowire photonic crystal waveguides for single-atom trapping and strong light-matter interactions. *Applied Physics Letters*, 104(11):111103, 2014.

[58] A. Zhan, S. Colburn, R. Trivedi, T. K. Fryett, C. M. Dodson, and A. Majumdar. Low-contrast dielectric metasurface optics. *ACS Photonics*, 3(2):209–214, 02 2016.

APPENDICES

Appendix A

MODE Simulation Details

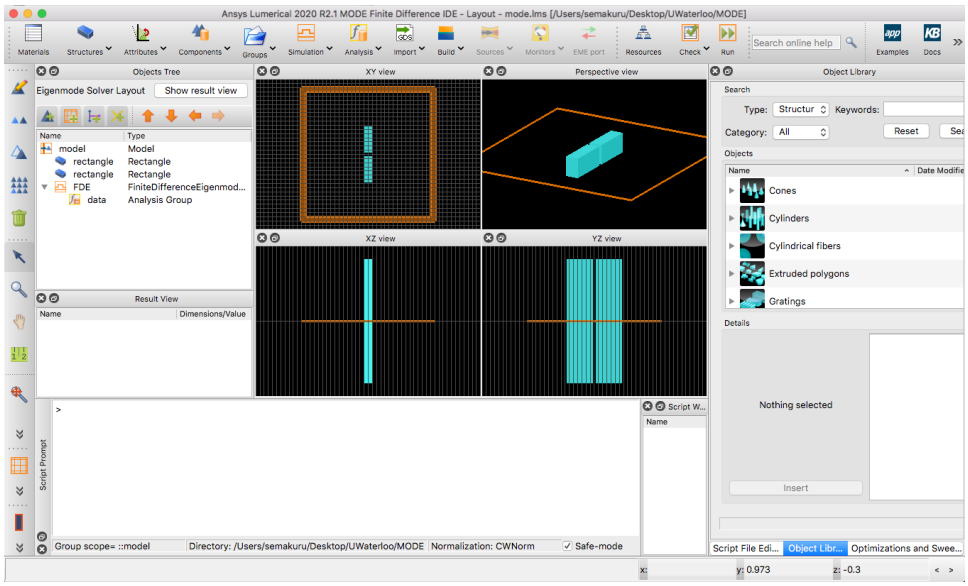

Figure A.1: MODE simulations setup screen.

MODE simulations are done in Section 2.4 to calculate the modes and the associated n_{eff} in rectangular waveguides, and in Section 3.3 to calculate the coupling and propagation modes. The general procedure for MODE simulations is presented here. In Fig. A.1, the main simulation GUI is given. On the left, the list of structures, monitors and the simulation region is given. Finite difference eigenmode (FDE) solver calculates the field

profile of modes by solving Maxwell's equations over a cross-section of the waveguide (see Fig. 3.9 a). The solver calculates the mode field profiles and effective refractive indices of the modes.

When the simulation is run, the results view is activated, given in Fig. A.2. On lower left, the wavelength (or frequency) of the modes can be entered, and at the bottom of the page (not seen here), the button "calculate modes" starts the simulation, and the list of modes at the top appears. Clicking on each mode shows the associated field profile in the lower right region. The information about the modes are listed at the top. TE polarization fraction (Ex) shows the fraction of light that is E_x polarized. This means the first two modes are E_y, while the third mode is E_x. In Fig. 3.9 b, the coupling mode is said to be E_x, but here, it is E_y. This inconsistency is due to the different choice of axis in Fig. 3.9 b compared to here.

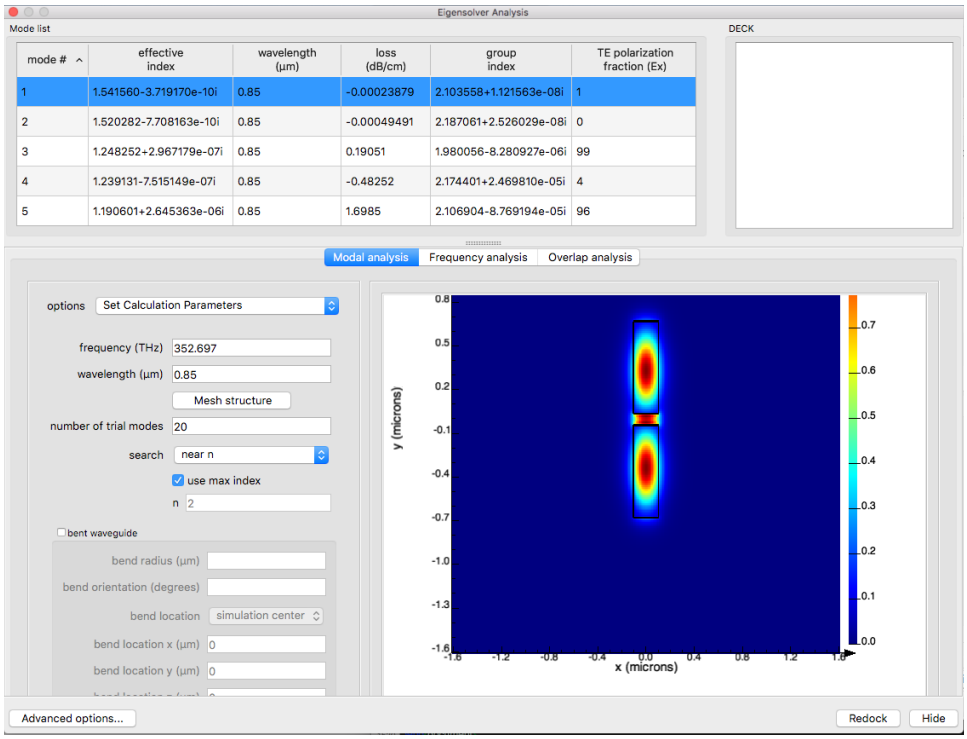

Figure A.2: MODE simulations eigensolver results view. The current result correspond to the coupling mode in Fig. 3.9 b.

Appendix B

FDTD Simulation Details

FDTD is the main method used to design and analyse the metasurface mirror structure. For the simulation of the unit cell and whole mirror, here are some simulation settings:

1. Periodic boundary conditions in x and y, and PML boundary condition in z. PML profile is set to "steep angle," which is the best setting if PML is used with periodic boundary conditions.

2. Set the sources to correct phase depending on the simulation purpose. Linearly polarized input for recording phase difference, and right-handed circularly polarized light for finding the purity.

3. Simulation time is set to $5000 \times 10^{-15} s$. If there is unexpected loss in the simulation region or unexpected field oscillations, auto shutoff might need to be turned off.

4. Higher mesh setting allows finer representation of the structures, which is necessary when nanopillars are rotated. Typically, mesh is set to 4, and additional mesh region is inserted around the nanopillars for the unit cell simulations. Also, mesh can be set to 8, without the additional mesh, but simulation will take a longer time. The large mirror simulations are done with mesh setting of 2, because larger mesh require more computer memory. Mesh refinement is set to "conformal variant 1," which provides better convergence when metals are simulated.

5. The size of FDTD boundaries is the unit cell size for the unit cell simulations, and is the diameter for the mirror.

The following script is used to set up a sweep over any parameter and to record the electric field and reflectivity information to a text file, which is then processed in python (see Appendix C). The Lumerical FDTD files to run the scripts can be found on [30].

```
# SWEEP OVER ANGLE OR WIDTH
index_850 = 1; # 1 if monochromatic, otherwise index of 850nm
No_of_points = 180;
range_min = 0;
range_max = 180;

variable = range_min;
inc = (range_max - range_min) / No_of_points;

for(i=1:No_of_points){ # Sweeping over the variable range
    switchtolayout;
    select("::model"); # Material properties are scripted into model
    set("theta",variable); # change to any parameter that "variable" is
        representing

    run;

    E1 = getresult("R", "E");
    y1 = E1.lambda;
    Ex = E1.getattribute("Ex");
    Xph = angle(Ex);
    Ey = E1.getattribute("Ey");
    Yph = angle(Ey);
    ph_diff = abs(Xph - Yph);
    R = getresult("field_far","T");
    R = R.T;
    T = getresult("field_below","T");
    T = T.T;

    for (i=1:length(y1)){
    str = num2str(variable)+", "+num2str(y1(i))+", "+num2str(R(i))+",
        "+num2str(T(i))+", "+num2str(Ex(i))+", "+num2str(Ey(i))+",
        "+num2str(ph_diff(i));
    write("NaSi_des_swth.txt",str); # Save data in a txt file, processing it in
        python
    }
```

```
    variable = variable + inc;
}
# To make a 2D sweep, include another "for" loop for the second variable
```

For the simulation of the entire mirror ($15\mu m$), electric field and reflectivity information is extracted and recorded into text files by the following script.

```
index_850 = 1;
mirror_span = 15e-6;
D = 15e-6;

run;

E = getresult("field_near" , "E"); # monitor named field_near, located at the
    top of nanopillars
x = E.x;
y = E.y;
z = E.z;
lambda = E.lambda;
E_ = E.E;
E_mag = pinch(sqrt(E.E2), 4,index_850);
Ex = pinch(E.Ex , 4, index_850);
Ey = pinch(E.Ey , 4, index_850);
Ez = pinch(E.Ez , 4, index_850);
R1 = getresult("field_near" , "T");
Rnear = R1.T;
T1 = getresult("field_below" , "T"); # monitor named field_near, located below
    the metal layer
T = T1.T;

n = 1;
for (i=1:length(x) ) {
    for (j=1:length(y) ) {
        str = num2str(x(i))+", "+num2str(y(j))+", "+num2str(Ex(n))+",
            "+num2str(Ey(n))+", "+num2str(Ez(n))+", "+num2str(Rnear)+",
            "+num2str(T);
    n = n+1;
    filename = "NaSi_fab_spacer_15um_f30_E_all_xy_pixel"+num2str(p)+".txt";
    write(filename,str);
    # field monitor located at z = 700nm
```

```
}}
```

Appendix C

Python Code for Full Mirror Analysis and Fourier Propagation

This is the python code for extracting the results from simulations of unit cell, recorded into text files and analyse the data.

```
import numpy as np
import pylab as pl
import scipy.special as sp
#import integration2 as integ
import scipy.optimize as opt
import cmath
import matplotlib.patches as patches
import matplotlib as mpl


dim_x = 60 # dimensionality of the first variable
dim_y = 1 # dimensionality of the second variable, set to 1 if single wavelength

filename = "NaSi_des_swH2copy.txt"
with open(filename) as f:
    lines = f.readlines()        # each line is y = y'
    print("number of data: ", len(lines))
    no_of_colmn = 14 # if working with complex no, each coln is counted twice

    Matrix = np.zeros([no_of_colmn,len(lines) ])
```

```
    x = 0                 # column index of the matrix set to zero
    y = 0                 # row index of the matrix set to zero

    for i in lines[ :len(lines)]:
        a = ''                          # data is in string, initialize each
            data a
        for j in i:
            a = a + j                   # Update reading
            if j == ',':                # Data seperation reached
                a = a[:len(a)-1]        # Subtract ,
                a = ''.join(a.split())
                a=a.replace("i","j",1)
#                print(a)
                Matrix[x,y] = complex(a).real
                x = x + 1
                Matrix[x,y] = complex(a).imag
                x = x + 1               # Going along the row
                a = ''
        a = a[:len(a)-1]         # Subtract ,
        a = ''.join(a.split())
        a=a.replace("i","j",1)
        Matrix[x,y] = complex(a).real
        x = x + 1
        Matrix[x,y] = complex(a).imag
        y = y + 1                       # Next row
        x = 0                           # Back to the first column

# First variable, usually W1 or nanopillar angle
x = np.zeros([dim_x])
for i in range(dim_x):
    x[i] = Matrix[0][i*dim_y]
# Second variable, usually the wavelength or W2
y = Matrix[2][0:dim_y]
# R and T are extracted
Rin = Matrix[4].reshape(dim_x,dim_y)
Tin = -Matrix[6].reshape(dim_x,dim_y)
# real and imag parts of E are extracted separately
Ex_Real = Matrix[8].reshape(dim_x,dim_y)
Ex_Im = Matrix[9].reshape(dim_x,dim_y)
Ey_Real = Matrix[10].reshape(dim_x,dim_y)
```

```
Ey_Im = Matrix[11].reshape(dim_x,dim_y)

""" If multiple wavelengths and we want to get 850nm result """
#for i in range(len(y)):
#    if y[i] < 850e-9:
#        break
#index_850 = i

""" If the simulation is run only for 850nm, unindent this part of code """

index_850 = 0
theta = x

Exreal = np.zeros(dim_x)
Eyreal = np.zeros(dim_x)
Eximag = np.zeros(dim_x)
Eyimag = np.zeros(dim_x)
R = np.zeros(dim_x)
T = np.zeros(dim_x)
for i in range(len(Ex_Real)):
    Exreal[i] = Ex_Real[i][index_850]
    Eyreal[i] = Ey_Real[i][index_850]
    Eximag[i] = Ex_Im[i][index_850]
    Eyimag[i] = Ey_Im[i][index_850]
    R[i] = Rin[i][index_850]
    T[i] = Tin[i][index_850]
loss = 1 - (R+T)

""" If the variable is wavelength, unindent this part of code """

#theta = y

#R = Rin[0]
#T = Tin[0]
#Exreal = Ex_Real[0]
#Eyreal = Ey_Real[0]
#Eximag = Ex_Im[0]
#Eyimag = Ey_Im[0]
#loss = 1 - (R+T)
```

```
""" Electric field vector manipulation """

Exvector = (Exreal + 1j * Eximag) / np.sqrt(2) # Ex = [re(Ex) + i im(Ex)]
    /sqrt(2)
Eyvector = (Eyreal + 1j * Eyimag) / np.sqrt(2) # Ey = [re(Ey) + i im(Ey)]
    /sqrt(2)
Ercp = (Exvector + Eyvector*1j) / np.sqrt(2) # E_rcp = Ex + i Ey
Elcp = (Exvector + Eyvector*-1j) / np.sqrt(2) # E_lcp = Ex - i Ey

""" Separate phase and magnitude of E vectors """

def magnitude_phase(E_in):
    Eph = np.zeros([len(E_in)])
    Er = np.zeros([len(E_in)])
    for i in range(len(E_in)):
        Er[i], Eph[i] = cmath.polar(E_in[i])
    return Er , Eph

Elcpr , Elcpph = magnitude_phase(Elcp) # mag and ph of LHCP
Ercpr , Ercpph = magnitude_phase(Ercp) # mag and ph of RHCP
Exr , Exph = magnitude_phase(Exvector) # mag and ph of Ex
Eyr , Eyph = magnitude_phase(Eyvector) # mag and ph of Ey

E_mag = np.sqrt(abs(Exvector) **2 + abs(Eyvector)**2) # |E| = sqrt(|Ex|**2 +
    |Ey|**2)

ph_diff = abs(Exph - Eyph) / np.pi # ph(Ex) - ph(Ey) normalized to pi

""" next is plotting figures / analysis of data for specific cases like phase
    normalization """
```

This is the python code for the analysis of the whole mirror structure, including focusing and cavity analysis:

```
import numpy as np
import pylab as pl
import scipy.special as sp
import scipy.optimize as opt
import cmath
```

```
import scipy.fftpack as sfft

radius = 7.5e-6
R = 0.895
monitor = 0.7e-6
focalp = 28e-6
wavelength = 850e-9

filename = "NaSi_fab_15um_f30_E_all_xy_pixel1.txt"
with open(filename) as f:
    lines = f.readlines()        # Each line is y = y'
#    info = lines[0]
    print("lines " ,len(lines))
    no_of_data_each_row = 14
    sweep_dimensionx = int(np.sqrt(len(lines)))
    sweep_dimensiony = int(np.sqrt(len(lines)))
    Matrix = np.zeros([no_of_data_each_row,len(lines)])

    x = 0                # column index of the matrix set to zero
    y = 0                # row index of the matrix set to zero

    for i in lines[:len(lines)]:
        a = ''                          # Data is in string, initialize each
            data a
        for j in i:
            a = a + j                   # Update reading
            if j == ',':                # Data seperation reached
                a = a[:len(a)-1]        # Subtract ,
                a = ''.join(a.split())
                a=a.replace("i","j",1)
                Matrix[x,y] = complex(a).real
                x = x + 1
                Matrix[x,y] = complex(a).imag
                x = x + 1               # Going along the row
                a = ''
        a = a[:len(a)-1]         # Subtract ,
#        Matrix[x,y] = float(a)   # Final term doesnt have comma at the end
        a = ''.join(a.split())
        a=a.replace("i","j",1)
        Matrix[x,y] = complex(a).real
```

```
        x = x + 1
        Matrix[x,y] = complex(a).imag
        y = y + 1                       # Next row
        x = 0                           # Back to the first column

x1 = np.zeros([sweep_dimensionx])
for i in range(sweep_dimensionx):
    x1[i] = Matrix[0][i*sweep_dimensiony]

y1 = Matrix[2][0:sweep_dimensiony]

Exreal = Matrix[4].reshape(sweep_dimensiony,sweep_dimensionx)
Eyreal = Matrix[6].reshape(sweep_dimensiony,sweep_dimensionx)
Ezreal = Matrix[8].reshape(sweep_dimensiony,sweep_dimensionx)
Eximag = Matrix[5].reshape(sweep_dimensiony,sweep_dimensionx)
Eyimag = Matrix[7].reshape(sweep_dimensiony,sweep_dimensionx)
Ezimag = Matrix[9].reshape(sweep_dimensiony,sweep_dimensionx)


Exvector = Exreal + 1j * Eximag / np.sqrt(2)
Eyvector = Eyreal + 1j * Eyimag / np.sqrt(2)
Ercp = (Exvector + Eyvector*1j) / np.sqrt(2)
Elcp = (Exvector + Eyvector*-1j)/ np.sqrt(2)


""" Get phase and magnitude of LCP and RCP """

def magnitude_phase(E_in):
    Eph = np.zeros([len(E_in)])
    Er = np.zeros([len(E_in)])
    for i in range(len(E_in)):
        Er[i], Eph[i] = cmath.polar(E_in[i])
    return Er , Eph

Elcpr , Elcpph = magnitude_phase(Elcp) # mag and ph of LHCP
Ercpr , Ercpph = magnitude_phase(Ercp) # mag and ph of RHCP
Exr , Exph = magnitude_phase(Exvector) # mag and ph of Ex
Eyr , Eyph = magnitude_phase(Eyvector) # mag and ph of Ey

E_mag = np.sqrt(abs(Exvector) **2 + abs(Eyvector)**2) # |E| = sqrt(|Ex|**2 +
```

```
    |Ey|**2)

ph_diff = abs(Exph - Eyph) / np.pi # ph(Ex) - ph(Ey) normalized to pi


""" Calculating the phase profile and RH purity """

phi_spherical = np.zeros([len(x1),len(y1)])
for i in range(len(x1)):
    for j in range(len(y1)):
        phi_spherical[j][i] = 2*np.pi/wavelength * (focalp -
            np.sqrt(x1[i]*x1[i] + y1[j]*y1[j] + focalp*focalp))
        if phi_spherical[j][i] < -2*np.pi:
            phi_spherical[j][i] = phi_spherical[j][i] + 2*np.pi
        if phi_spherical[j][i] < -np.pi:
            phi_spherical[j][i] = phi_spherical[j][i] + 2*np.pi


pl.figure(1)
pl.contourf(x1*1e6, y1*1e6, phi_spherical/np.pi, 500, cmap ='jet')
cbar = pl.colorbar(ticks=np.arange(-1,1+0.01,0.5))
cbar.ax.tick_params(labelsize=13)
cbar.set_label('$\phi_{sp}$ ($\pi$ rad)', fontsize=14)
pl.xlabel("x ($\mu$m)", fontsize=13)
pl.ylabel("y ($\mu$m)", fontsize=13)


PHASEOVERALL = np.zeros([len(x1),len(y1)])
PHASEOVERALL[0:int(len(x1)/2)] = phi_spherical[0:int(len(x1)/2)]/np.pi
PHASEOVERALL[int(len(x1)/2):-1] = Ercpph[int(len(x1)/2):-1]/np.pi

phasemirror = Ercpph

pl.figure(2)
pl.contourf(x1*1e6 , y1*1e6 , PHASEOVERALL , 500, cmap ='jet')
pl.xlabel("x ($\mu$m)",fontsize=13)
pl.ylabel("y ($\mu$m)",fontsize=13)
pl.xticks(np.arange(-7.5, 7.5+0.1, 7.5),fontsize=13)
pl.yticks(np.arange(-7.5, 7.5+0.1, 7.5),fontsize=13)
cbar = pl.colorbar(ticks=np.arange(-1,1.1,0.5))
```

```
cbar.ax.tick_params(labelsize=13)
cbar.set_label('$\phi_{RH}$ ($\pi$ rad)', fontsize=14)
pl.plot([-7.5,7.5],[0,0], 'k--',linewidth=1,alpha=1)
pl.text(-2, -7, "theoretical", fontsize=13 , color = 'k')
pl.text(-3, 6.5, "simulation result", fontsize=13 , color = 'k')

#pl.savefig("NaSi_15um_RHphase_compare.jpg",dpi= 1000)


ratio = Ercpr / (Ercpr+Elcpr)
sum(sum(ratio)) / len(lines)
purity = Ercp*np.conj(Ercp) / (Ercp*np.conj(Ercp)+Elcp*np.conj(Elcp))
print("ratio of Ircp to Iout is :", sum(sum(purity)) / len(lines))
print("ratio of Ircp to Iin is :", sum(sum(purity)) / len(lines) * R)
""" """

pl.figure(3)
pl.contourf(x1*1e6 , y1*1e6 , purity*89.5/100, 100, cmap ='RdYlGn')
#pl.colorbar()
pl.xlabel("x ($\mu$m)",fontsize=13)
pl.ylabel("y ($\mu$m)",fontsize=13)
cbar = pl.colorbar(ticks=np.arange(0,1.1,0.2))
cbar.ax.tick_params(labelsize=13)
cbar.set_label('$R_{RH}$', fontsize=14)
pl.xticks(np.arange(-7.5, 7.5+0.1, 7.5),fontsize=13)
pl.yticks(np.arange(-7.5, 7.5+0.1, 7.5),fontsize=13)
#pl.savefig("NaSi_15um_RHpurity.jpg",dpi= 1000)

#pl.title("Amount of RCP component in reflected wave, z = 0.6um")
#pl.title("|Ercp|**2/(|Ercp|**2+|Elcp|**2), z = 0.6um")
""" Propagation by FFT after one reflection """

""" Set k vectors """
x = x1
y = y1
dx = x[5]-x[4]
kx = np.fft.fftfreq(len(x) , d=dx)*2*np.pi
ky = kx
k0 = 2*np.pi /(wavelength)
```

```
kz = np.ones([len(kx),len(ky)])*1j
for i in range(len(kx)):
    for j in range(len(ky)):
        kz_n = k0**2 - kx[i]**2 - ky[j]**2
        if kz_n < 0:
            kz[i][j] = 1j*np.sqrt(np.abs(k0**2 - kx[i]**2 - ky[j]**2))
        else:
            kz[i][j] = np.sqrt(k0**2 - kx[i]**2 - ky[j]**2)

""" Propagation function """

def propagate(E_in, z): # returning the field and intensity in 2D
    Urcp = E_in
    Urcp_tilde = np.fft.fft2(Urcp)
    Urcp_tilde_z = Urcp_tilde * np.exp(1j * kz * z)
    U_z = (np.fft.ifft2(Urcp_tilde_z))
    I = U_z * np.conj(U_z)
    return U_z, I

""" Propagate through z axis in 2D """

def Power_yz_lcp(z): # Returns the 2D LHCP electric field z distance away from
    the mirror
    P_out = np.zeros([len(z) , len(y1)])
    for i in range(len(z)):
        zf = z[i] - monitor
        U_zf, I = propagate(Elcp, zf)
        for j in range(len(I[int(sweep_dimensionx/2)])):
            P_out[i][j] = (I[int(sweep_dimensionx/2)][j])
    return P_out

def Power_yz_rcp(z): # Returns the 2D RHCP electric field z distance away from
    the mirror
    P_out = np.zeros([len(z) , len(y1)])
    for i in range(len(z)):
        zf = z[i] - monitor
        U_zf, I = propagate(Ercp, zf)
        for j in range(len(I[int(sweep_dimensionx/2)])):
            P_out[i][j] = (I[int(sweep_dimensionx/2)][j])
    return P_out
```

```
z = np.linspace(focalp - 25e-6 , focalp + 20e-6 ,500)
Poweryzlcp = Power_yz_lcp(z)
Poweryzrcp = Power_yz_rcp(z)
Poweryzall = Poweryzlcp+Poweryzrcp

PoweryzrcpT = Poweryzrcp.T #Transpose
PoweryzlcpT = Poweryzlcp.T

# y = 0 intensity distribution
Powerzall = (PoweryzrcpT[int(len(x1)/2)]+PoweryzlcpT[int(len(x1)/2)])

pl.figure(5)
pl.plot(z*1e6 , Powerzall)
pl.xlabel("z ($\mu$m)")
pl.ylabel("Intensity(MV/m2)")
pl.title("Intensity vs distance from mirror (FT)")
##pl.axis([2.3,2.6,80,100])

pl.figure(6, figsize =(18,7))
pl.contourf(z*1e6 , x*1e6, Poweryzall.T , 500, cmap ='hot')
pl.plot(z*1e6 , (1e-6*Powerzall*1e6/10)-7)
pl.xlabel("z ($\mu$m)", fontsize=13)
pl.ylabel("x ($\mu$m)", fontsize=13)
pl.xticks(np.arange(3, 48, 5),fontsize=13)

#pl.savefig("NaSi_15um_focusing2.jpg",dpi= 1000)

""" Focal Plane """

zf = focalp - monitor
E_focal, I = propagate(Ercp, zf)

pl.figure(7)
pl.contourf(x*1e6 , y*1e6, (I)*1e-6 , 500, cmap ='hot')
#cbar = pl.colorbar(ticks=np.arange(0,6+0.1,1))
#cbar.ax.tick_params(labelsize=13)
pl.colorbar()
pl.xlabel("x ($\mu$m)", fontsize=13)
pl.ylabel("y ($\mu$m)", fontsize=13)
```

```
pl.xticks(np.arange(-7.5, 7.5+0.1, 7.5),fontsize=13)
pl.yticks(np.arange(-7.5, 7.5+0.1, 7.5),fontsize=13)
#pl.plot([145,150],[222,222],c='w',linewidth=1,alpha=0.7)
#pl.text(146, 222.6, "5 nm", fontsize=12 , color = 'w')
#pl.plot([150,150],[207,236],"--",c='k')

#pl.savefig("NaSi_15um_focuspoint.jpg",dpi= 1000)

""" Normalize to Airy disk 1D intensity """
x2 = np.linspace(-radius, radius+0.001e-6,1006)
th = np.arctan(x2 / focalp)
a = radius*2
focalp = 28e-6

def integ_data(x,y): # Integrating functions with finite data points using
    trapezoidal rule
    h = (x1[5]-x1[4])*1e6
    return (2*sum(y) - y[0] - y[-1]) * h /2

def Airy_circ(x): # Airy function for circular aperture
    th = np.arctan(x/focalp)
    return (2*sp.j1(k0*a*np.sin(th))/(k0*a*np.sin(th)))**2

def Airy_rect(x): # Airy function for rectangular aperture
    th = np.arctan(x/focalp)
    return np.sinc(k0*a*np.sin(th)/(2*np.pi))**2 *np.sinc(k0*a*np.sin(0)/2)**2

def integration_difference(Amax): # Computes the difference in integral of Airy
    func and data
    I1 = integ_data(x1 , I[int(sweep_dimensionx/2)])*Amax # Integral of data
    I2 = integ_data(x1 , Airy_rect(x1)) # Integral of Airy function
    return np.abs(I1 - I2)

A = opt.fmin(integration_difference,[1/100])

pl.figure(9)
pl.plot(x*1e6 , I[int(sweep_dimensionx/2)]*A)
pl.plot(x*1e6 ,Airy_rect(x2))

##pl.plot(xEx*1e6 , result[67]*759.8973)
```

```
pl.xlabel("x ($\mu$m)", fontsize = 13)
pl.ylabel("Intensity", fontsize = 13)
#pl.xticks(np.arange(-50, 50+0.1, 25),fontsize=13)
#pl.yticks(np.arange(0, 1.01, 0.2),fontsize=13)
#pl.title("Intensity at focal point 1D, f = 10 um")
#pl.legend(["Intensity (FT)","Diffraction Limit"],fontsize=13,
#          loc=(0.53,0.75))
pl.axis([-0.75,-0.6,0.48,0.52])
#pl.savefig("NaSi_15um_1DAiry.jpg",dpi= 1000)

dx = (x[5]-x[4])*1e6
FTI = np.fft.fft(I[int(sweep_dimensionx/2)]*A)
FTAiry = np.fft.fft(Airy_rect(x))

""" Cavity Multiple Mirror """

def reflect(E_in, phaseprofile):
    Eref = E_in.reshape(len(lines),1)
    phaseprofile = phaseprofile.reshape(len(lines),1)
    Ercpph_n = np.zeros([len(Eref)])
    Ercpr_n = np.zeros([len(Eref)])
    for i in range(len(Eref)):
        Ercpr_n[i] , Ercpph_n[i] = cmath.polar(Eref[i])
        Ercpph_n[i] = Ercpph_n[i] + phaseprofile[i]
        if Ercpph_n[i] < -np.pi:
            Ercpph_n[i] = Ercpph_n[i] +2*np.pi
            if Ercpph_n[i] > np.pi:
                Ercpph_n[i] = Ercpph_n[i] -2*np.pi
                Eref[i] = (Ercpr_n[i])*np.cos(Ercpph_n[i]) +
                    1j*(Ercpr_n[i])*np.sin(Ercpph_n[i])
    Eref = Eref.reshape(sweep_dimensiony,sweep_dimensionx)
    Ercpr_n = Ercpr_n.reshape(sweep_dimensiony,sweep_dimensionx)
    Ercpph_n = Ercpph_n.reshape(sweep_dimensiony,sweep_dimensionx)
    return Eref


""" Second mirror """

E_focal, I = propagate(Ercp , focalp)
E2_m, I2_m = propagate(E_focal , focalp)
```

```
E2_m = E2_m.reshape(len(lines),1)
phasemirror = phasemirror.reshape(len(lines),1)
Ercpph2 = np.zeros([len(E2_m)])
Ercpr2 = np.zeros([len(E2_m)])
for i in range(len(E2_m)):
    Ercpr2[i] , Ercpph2[i] = cmath.polar(E2_m[i])
    Ercpph2[i] = Ercpph2[i] + phasemirror[i]
    if Ercpph2[i] < -np.pi:
        Ercpph2[i] = Ercpph2[i] +2*np.pi
    if Ercpph2[i] > np.pi:
        Ercpph2[i] = Ercpph2[i] -2*np.pi
    E2_m[i] = (Ercpr2[i])*np.cos(Ercpph2[i]) + 1j*(Ercpr2[i])*np.sin(Ercpph2[i])

E2_m = E2_m.reshape(sweep_dimensiony,sweep_dimensionx) *np.sqrt(R)

E2focalp, I2 = propagate(E2_m, focalp)

print("Intensity sum of I2 / no of data:", sum(sum(I2))/len(lines))
print("Intensity ratio to initial, I2:", sum(sum(I2))/sum(sum(I)))

pl.figure()
pl.contourf(x*1e6 , y*1e6, (I2) , 500, cmap ='hot')
cbar = pl.colorbar(ticks=np.arange(0,6+0.1,1))
cbar.ax.tick_params(labelsize=13)
pl.xlabel("x ($\mu$m)", fontsize=13)
pl.ylabel("y ($\mu$m)", fontsize=13)
pl.xticks(np.arange(-7.5, 7.5+0.1, 7.5),fontsize=13)
pl.yticks(np.arange(-7.5, 7.5+0.1, 7.5),fontsize=13)
#pl.title("I2")

#pl.savefig("intensity_on_second_focalp.jpg", dpi=1000)

""" This code is repeated for 20 mirrors, i.e. 15 roundtrips """
```

Appendix D

Derivation of the Matrix for Mirror Reflectivity Calculations

The reflectivity and transmission of the metallic layer will be calculated numerically. We will derive the matrix for the calculation for a single mirror, but this analysis is usually done for periodic structures with any two materials. Let's consider the structure in Fig. D.1. Two materials of refractive indices n_1 and n_2 are present. For our purposes, the white material is air ($n_1 = 1$) and the gray material is silver ($n_2 = 0.15267 - 5.6903i$). The electric field at each region can be written as

$$\begin{aligned} E_1 &= A_1 e^{-ik_1 z} + B_1 e^{ik_1 z} \\ E_2 &= A_2 e^{-ik_2 z} + B_2 e^{ik_2 z} \\ E_3 &= A_3 e^{-ik_1 z} \end{aligned} \tag{D.1}$$

At the first boundary, denotes by in the diagram, $E_1 = E_2$ and $dE_1/dz = dE_2/dz$ according to the continuity of field at a boundary.

$$\begin{aligned} A_1 e^{-ik_1 d} + B_1 e^{ik_1 d} &= A_2 e^{-ik_2 0} + B_2 e^{ik_2 0} \\ -ik_1 A_1 e^{-ik_1 d} + ik_1 B_1 e^{ik_1 d} &= -ik_2 A_2 e^{-ik_2 0} + ik_2 B_2 e^{ik_2 0} \end{aligned} \tag{D.2}$$

This can be written in the matrix form

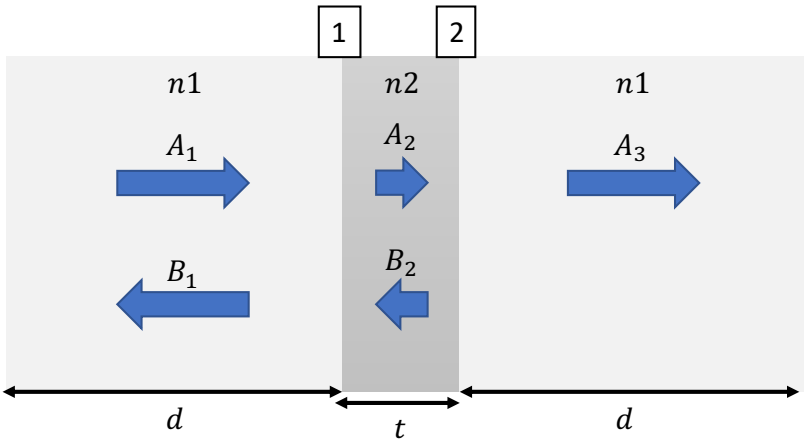

Figure D.1: Diagram for the structure used to derive the matrix for calculating the reflectivity and transmission of a structure.

$$\begin{pmatrix} e^{-ik_1 d} & e^{ik_1 d} \\ -ik_1 e^{-ik_1 d} & ik_1 e^{ik_1 d} \end{pmatrix} \begin{pmatrix} A_1 \\ B_1 \end{pmatrix} = \begin{pmatrix} e^{-ik_2 0} & e^{ik_2 0} \\ -ik_2 e^{-ik_2 0} & ik_2 e^{ik_2 0} \end{pmatrix} \begin{pmatrix} A_2 \\ B_2 \end{pmatrix} \tag{D.3}$$

The same can be written for the second boundary.

$$\begin{aligned} A_2 e^{-ik_2 t} + B_2 e^{ik_2 t} &= A_3 e^{-ik_1 0} \\ -ik_2 A_2 e^{-ik_2 t} + ik_2 B_2 e^{ik_2 t} &= -ik_1 A_3 e^{-ik_1 0} \end{aligned} \tag{D.4}$$

In its matrix form

$$\begin{pmatrix} e^{-ik_2 t} & e^{ik_2 t} \\ -ik_2 e^{-ik_2 t} & ik_2 e^{ik_2 t} \end{pmatrix} \begin{pmatrix} A_2 \\ B_2 \end{pmatrix} = \begin{pmatrix} e^{-ik_1 0} & e^{ik_1 0} \\ -ik_1 e^{-ik_1 0} & ik_1 e^{ik_1 0} \end{pmatrix} \begin{pmatrix} A_3 \\ 0 \end{pmatrix} \tag{D.5}$$

We set $B_3 = 0$ because there is no backwards-travelling wave for this case. Now we can combine the two results and write a matrix that will relate the coefficients of the first region with the coefficient of the third region.

$$\begin{pmatrix} e^{-ik_2 t} & e^{ik_2 t} \\ -ik_2 e^{-ik_2 t} & ik_2 e^{ik_2 t} \end{pmatrix} \begin{pmatrix} 1 & 1 \\ -ik_2 & ik_2 \end{pmatrix}^{-1} \begin{pmatrix} e^{-ik_1 d} & e^{ik_1 d} \\ -ik_1 e^{-ik_1 d} & ik_1 e^{ik_1 d} \end{pmatrix} \begin{pmatrix} A_1 \\ B_1 \end{pmatrix} \tag{D.6}$$

$$= \begin{pmatrix} 1 & 1 \\ -ik_1 & ik_1 \end{pmatrix} \begin{pmatrix} A_3 \\ 0 \end{pmatrix} \tag{D.7}$$

The first and final coefficients are related by a matrix $\mathbf{M}$, such that

$$\begin{pmatrix} A_3 \\ 0 \end{pmatrix} = \mathbf{M} \begin{pmatrix} A_1 \\ B_1 \end{pmatrix} \tag{D.8}$$

where the matrix is defined as

$$\mathbf{M} = \begin{pmatrix} 1 & 1 \\ -ik_1 & ik_1 \end{pmatrix}^{-1} \begin{pmatrix} e^{-ik_2 t} & e^{ik_2 t} \\ -ik_2 e^{-ik_2 t} & ik_2 e^{ik_2 t} \end{pmatrix} \begin{pmatrix} 1 & 1 \\ -ik_2 & ik_2 \end{pmatrix}^{-1} \begin{pmatrix} e^{-ik_1 d} & e^{ik_1 d} \\ -ik_1 e^{-ik_1 d} & ik_1 e^{ik_1 d} \end{pmatrix} \tag{D.9}$$

Appendix E

Analysis of Design with Optimized Spacer Thickness

A new spacer thickness is proposed to improve the metallic loss. The new thickness provides and optical path of $\lambda/2$, which is calculated to be $293nm$ for glass spacer. It is found to reduce the metallic loss by 2%, but it does not overcome the full metallic loss. A new unit cell design is found by this thickness since the phase difference is found to change slightly. The design parameters are the same as Fig. 4.4, but the only change is $W2 = 228nm$.

This unit cell design is simulated by rotating the nanopillars from 0 to 180 deg. Reflectivity and transmission are 92% and 0.8% respectively and are constant throughout this range. The RH purity and geometric phase plots are given in Fig. E.1.

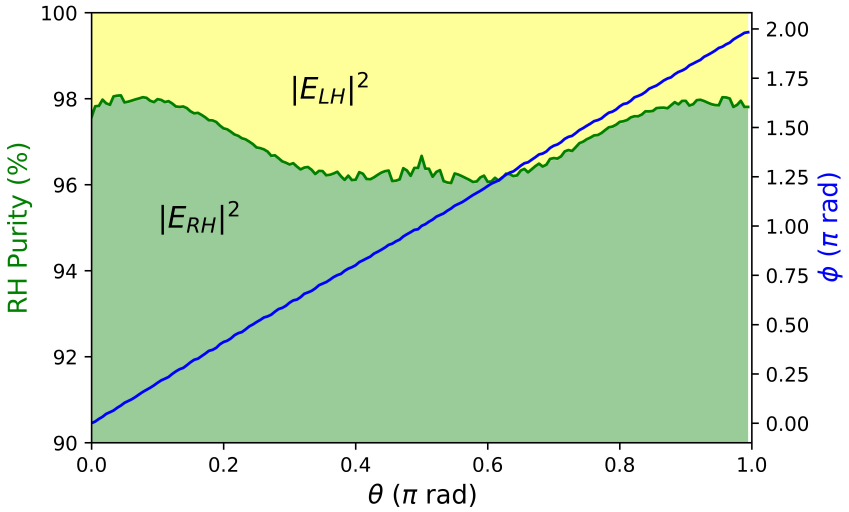

Figure E.1: Right handed (RH) purity at the output is shown by the green region, and left handed (LH) component is the yellow region over nanopillar angles for the design with new spacer thickness. The blue curve shows the geometric phase on RH component, ϕ_{RH}, which should have 1:2 ratio with θ.

Appendix F

Mounting Mirrors on Fibers

The method for mounting metasurface mirrors on fiber tips is used by Dr. Jeremy Flannery, and is the method planning to be used here. The procedure for a photonic crystal mirror is given in Fig. F.1. The steps are as follows:

1. A sharp tungsten probe ($50\mu m$ diameter) is dipped into epoxy (Norland Optical Adhesive 88) to transfer epoxy to the tip of the probe. Then, the probe is lowered to the chip holding the mirror sample to create two epoxy droplets of similar size.
2. The optical fiber (HCPCF in the figure, PM fiber for this project) is lowered to the droplets to transfer the droplets to the fiber tip.
3. Epoxy covered fiber tip is lowered on to the mirror sample, making sure the fiber and the mirror are aligned and the fiber is perpendicular to the mirror by using two side cameras to check for verticality. The epoxy is cured with UV light.
4. The fiber is removed, with the mirror attached to the tip.

Our mirror structure is layered such that the lowest layer is a homogeneous layer of SiO2. Therefore, the droplet sizes and separations have more flexibility, as long as the tip of the fiber is parallel to the mirror.

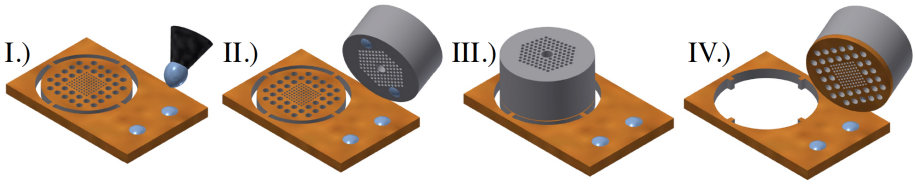

Figure F.1: Procedure for mounting metasurface mirrors to optical fiber tips. The steps are explained in text. The figure is obtained from [17].